Studies on Plasma Etching Process Based on Autonomous Control for Nano-meter Fabrication

SUZUKI Toshiya

2014

Nagoya University

Department of Electrical Engineering and Computer Science

Contents

Chapter 1 Introduction

1.1 Plasma Processing in Microelectronics Manufacturing------------------------------ 1
1.1.1 Trend and Challenge in Future Scale Integrated Circuits ---------------------- 2
1.1.2 Needs of Sophisticated Etching Technologies---------------------------------- 4
1.2 Plasma Processing for Low-*k* Materials
1.2.1 Plasma Processing System -- 5
1.2.2 Fine Pattern Profile of Low-*k* Materials ---6
1.3 Demands for Development of New Etching Process -------------------------------- 7
1.3.1 Needs of Plasma Nano-Science for Next Generation Etching Process ------ 9
1.3.2 Advanced Process Control (APC) -- 10
1.4 Goal and Construction of Present Research --- 12
1.5 References --- 13

Chapter 2 Plasma Diagnostic Techniques for Evaluating the Internal Parameters and Film Analysis Methods

2.1 Introduction -- 17
2.2 Vacuum Ultraviolet Absorption Spectroscopy (VUVAS)
2.2.1 Theory of Absorption Spectroscopy -- 18
2.2.2 Measurements of Absolute Densities of H and N Atoms with Micro-Discharge Hollow Cathode Lamp (MHCL) ---------------------------- 21
2.3 Optical Emission Spectroscopy (OES) -- 23
2.4 Methods for Evaluating Films Deposited and Etched
2.4.1 Spectroscopic Ellipsometry --- 27
2.4.2 X-Ray Photoelectron Spectroscopy (XPS) ------------------------------------ 30
2.5 References -- 32

Chapter 3 Realization of Nano-features by Nano-etch process

3.1 Introduction -- 33

3.2 Experimental Details

3.2.1 Metalorganic Supercritical Chemical Fluid Deposition (MOCFD) --------- 34

3.2.2 Dual-Frequency Capacitively Coupled Plasma Etcher ------------------------ 36

3.3 Results and Discussion

3.3.1 Fabrication of Organic Rods Armored by Pt Nanoparticles ----------------- 38

3.3.2 Pt Nanoparticles Diameter Dependence on the Deposition Condition ----- 43

3.3.3 Dependence of Plasma Etching Conditions on Feature-Profiles ------------ 47

3.3.4 Temporal Variations of Feature Shapes in Plasma Etching ------------------ 52

3.3.5 Comparison of Methods for Pt Particle Mask Deposition -------------------- 55

3.3.6 Sidewalls Protection Effect of Pt Nanoparticle against H Atoms ----------- 57

3.3.7 Analysis of Protection Effect of Pt Nanoparticle ------------------------------ 59

3.3.8 Applications in Field Emission Device -- 63

3.4 Conclusion --- 66

3.5 References -- 67

Chapter 4 Temporal Changes of Absolute Densities of Atoms by Surface Modifications of Reactor Wall

4.1 Introduction -- 70

4.2 Experimental Details --- 72

4.3 Results and Discussion

4.3.1 Generation and Loss of H and N atoms -------------------------------------- 76

4.3.2 Influence of Preceding Process on Atom Densities --------------------------- 78

4.3.3 Decay of Atom density in O_2 Plasma after H_2/N_2 Plasmas ------------------ 82

4.3.4 XPS Analyses on Al_2O_3 Film as a Reactor Wall Material ------------------- 84

4.3.5 Importance of Loss Process on Reactor Wall -------------------------------- 88

4.4 Conclusion -- 90

4.5 References -- 91

Chapter 5 Reactor Wall Loss Properties Influenced by the Preceding Process

5.1 Introduction --- 94

5.2 Experimental Details-- 95

5.3 Results and Discussion

5.3.1 Importance of Sticking and Loss Probabilities of Atoms ---------------- 97

5.3.2 Loss Kinetics of H and N Atoms in Afterglow of H_2/N_2 mixture plasma 99

5.3.3 Surface Loss Probabilities of H and N Atoms for Different Preceding Processes -- 101

5.3.4 Impact of Surface Properties on Surface Loss Probability -------------- 107

5.4 Conclusion --- 110

5.5 References --- 111

Chapter 6 Real Time Process Control of Plasma Etching Based on Atom Densities Measurements

6.1 Introduction -- 113

6.2 Experimental Details -- 116

6.3 Results and Discussion

6.3.1 Autonomous Control System --- 120

6.3.2 Properties of Low Dielectric Constant Organic Film----------------------- 123

6.3.3 Influence of Air Exposure on Atom Density -------------------------------- 126

6.3.4 Evaluation with Optical Emission Spectroscopy (OES) -------------------- 129

6.3.5 Impact of Atom Density Control on Etched Feature Profile --------------- 131

6.4 Conclusion --- 134

6.5 References --- 135

Chapter 7 Conclusions and Future Works

7.1 Conclusion of Present Research -- 138

7.2 Future Research Directions -- 142

Acknowledgements -- 143

List of Papers -- 145

Chapter 1 Introduction

1.1 Plasma Processing in Manufacturing

Approximately 40% steps in the microelectronics fabrication have used plasma processes. Applications in the micro-machining, the flat panel displays, the surface modification, the cleaning, the sterilization, the sputter coating, and many other areas have been rapidly growing based on the developments of microelectronics processing technology. The plasma-based processing development has been advanced the microelectronics industry over the past 30 years. Consistent annual doubling of the circuits complexity has been proceeded (table 1.1). Such development was proceeded to provide functionality and cost reduction. Thus, the understanding of fundamental reactions in plasma processes is important because plasma models are being applied as tools for the development of new plasma equipment and processes. These days, plasma diagnostics are also being applied as process monitors to control and improve the flexibility and reliability of the processes.

Table 1.1 Transistor count (based on Intel microprocessors).

Production year (MPU name)	1971 (4004)	1982 (80286)	1989 (80486)	2000 (Pentium4)	2004 (Itanium2)	2008 (Corei7)	2012 (Poulson)
Number of transistor	2,300	134,000	1,180,235	21 million	112 million	731 million	3100 million

1.1.1 Trend and Challenge in Future Scale Integrated Circuits

In modern society, all fields including electric communication are supported by Ultra-large scale integrated circuits (ULSI). In the future of ULSI devices, the high-speed operation to manipulate huge information will be demanded as well as the complex function. Responding to these demands, ULSI has been improved by the miniaturization high integration of device elements. For example, dynamic random access memory (DRAM) was developed in 1970 with 1 Kbit in capacity, it was improved to 1 Gbit in 1998. A microprocessor (MPU) consisted of about 2,300 transistors was developed in Intel Corporation in 1971, and its clock frequency was 108 kHz. Pentium(R) 4 processor™ consisted of 55 million transistors developed in 2001, and its clock frequency was 2.2 GHz. Intel Corporation commercialized the 45 nm Intel® Core™ i7 Processor consisted of transistors of 731 million in 2008. This system is a chip including four cores with multiple functional units and interfaces, and its clock frequency was higher than 3.6 GHz [1].

Table 1.2 shows the integration trend of MPU, DRAM and technology node [2]. The device components number on MPU and DRAM chips follows Moore low. In 2014, DRAM with 1 Tbit and MPU with 3.6 billion transistors/chip will be expected. For this purpose, the technology for interconnecting is getting more complicated.

Almost all of microelectronic devices are fabricated on the inorganic materials, i.e. Si and glass substrates. But as a recent issue, in the past a few years, it has been an huge interest in devices fabricating on organic materials for device applications such as mechanically flexible computers and displays. In future, even for the individual transistor will be made of organic materials [3-4]. These flexible electronics are beginning to make significant inroads into the commercial world.

Organic semiconductors on flexible films have been known recently [5]. However, achieving electronic properties equals to those on inorganic ones requires

high-quality crystals [6]. These cannot be easily made in the thin-film form by conventional vapor-deposition and etching technologies typically used in present microelectronics fabrication. In other words, advance in flexible electronics is derived from the ability of deposit and etching films on low-cost substrates such as plastic. Thus, the developments of new deposition and etching technologies are indispensible for large-scale circuit fabrication on flexible substrates.

Table 1.2 Integration trend and technology node of microprocessor and DRAM

Year	1997	1999	2003	2006	2009	2012
DRAM Bits/Chip	256 M	1 G	4 G	16 G	64 G	256 G
Microprocessor Transistor/chip	11 M	21 M	76 M	200 M	520 M	1.40 B
Technology node (DRAM)	250 nm	180 nm	130 nm	100 nm	70 nm	50 nm

1.1.2 Needs of Sophisticated Deposition and Etching Technologies for ICs Manufacturing

The integrated circuits (ICs) fabrication involves a basic stepwise manufacturing. The film is patterned with a light-sensitive polymer material coating known as photoresist. The photoresist is exposed to the radiation through a mask. Exposed areas of the photoresist undergo a change in chemical structure, and wash away (for a positive-tone resist). The patterned resist on the wafer protects the underlying film material. This process is well known as lithography. After patterning, the unprotected areas by photoresist are etched by a plasma etching process. After the etching process, the remaining resist is stripped with leaving features remaining in the film. These subsequent steps (film deposition, lithography, and etch) are repeated many times with different imaging masks to build many layers that make up a completed integrated circuit. Recently, the most typical type of integrated circuits (ICs) for MPU and memory has the complementary metal-oxide-semiconductor (CMOS) structure [7]. Up to 2000s, traditional CMOS devices have been used aluminum (Al) conductor and silicon oxide (SiO_2) dielectric interlayer of insulating film. However, traditional Al/SiO_2 interconnects have been replaced to Cu/low-*k* interconnects due to the RC delay in Al/SiO_2 system resulting from the scale-down less than 100 nm. Moreover, Intel reported that metal gate electrodes are applied as a replacement for polycrystalline Silicon (poly-Si), such as $TaSi_xN_y$, because scaling down of CMOS requires thin gate dielectric for high performance [8, 9]. The refractory metals are superior candidates to solve the problems associated with poly-Si gates. Recently, sputtering deposition of the electrode is more favorable than conventional chemical vapor deposition (CVD) for the CMOS process. This is because the impurity metal contained in the CVD degrades the dielectric reliability, especially at high-temperature. It also realize good uniformity with thinnest film of a few nanometers.

1.2 Plasma Processing for Low-*k* Materials

1.2.1 Plasma Processing System

Plasma processing such as etching and ashing are essential components for the fabrication of semiconductor device. The plasma process can be chemically selective and removing one type of material while leaving other materials. In addition, it also can be anisotropic and removing material at the trench bottom while leaving the same material on the sidewalls. The primary goal of etch process is to minimize the sidewall fluctuation and realize the vertical etching. The ashing process should be achieved without severe damage on the target film. These processes also should be performed with the control of the etching feature properties and the degree of undercutting. In addition, the plasma processes require selectivity to the mask and underlying substrate for the controllability of shape of target film and prohibiting damage on the target film [27]. Plasma etching is proceeded by the atoms generation, ions and accelerated ions to target film. Once the accelerated ions reach to the target, the ions can physically and chemically remove atoms from the target film [28,29]. Since they are electrically neutral, the atoms diffuse thermally onto the wafer. The ions reaches the wafer surface because it accelerated perpendicularly by a sheath field, and then they bombard the wafer surface. In the case of the plasma etching, bombardment of the ion is enhanced by an RF bias power. The atoms and ions react with the surface [30]. Those etching reactions proceed by reactions between a target film and gas species add by-products to the plasma. Therefore, internal plasma parameters such as electron density and temperature, substrate temperature, atom and ion density etc. are connected with the process performance [31,32]. It has been pointed out that the effect of light radiation in the wavelength region of vacuum ultra-violet (VUV) and ultra-violet (UV) during the etching process.

1.2.2 Fine Pattern Profile of Low-*k* Materials

Feature profile control is extremely difficult in etching process of organic material, because organic materials is instable mechanically and chemically compared with inorganic. The semiconductor industry trend has demanded to fabricate integrated circuits (ICs) with more transistors on a smaller area, a precise etching process of low-*k* material with a few nm order will be demanded soon. Plasma process controls are conducted by adjusting the external parameters such as gas mixture ratio. However, it is very difficult to etch the material with ideal etching features reproducibly by different etching equipment, since plasma characteristics widely vary depending on the equipment mechanical variations such as reactor size and structure. The etching process should be carried out with setting the internal parameters at specific values via the control of the external parameters. The knowledge of etching properties based on the external parameters pressure is not coherent with other apparatus. Conversely, the information based on the internal plasma parameters is uniquely and independently among the variety types of apparatus. Thus, I focused on etch features based on the internal parameters, and investigated an etching mechanism for realizing highly precise profile control of etching features in low-*k* organic films.

1.3 Demand for Development of New Etching Process

The size of the semiconductor device was estimated to be 24 billion dollars in 2006. Technology innovations were realized along Moore's law [24] aiming at increasing the components on a chip. These technology innovations are proceeded by technology node scaling-down for realizing higher integration. Plasma processes such as plasma etching, PECVD and magnetron sputtering technologies are essential for production of all semiconductor devices . Among them, technologies of plasma etching such as reactive ion etching (RIE) are the currently used for characteristics improvement of silicon devices based on the scaling law. According to scaling down of device elements, a lot of requirements have been needed for solving the problems and acquiring good device characteristics. For example, the basic requirements for RIE, which are widely used as an etching process, can be classified as follows: (1) high microfabrication capability (high anisotropy, high selectivity, accurately controlled profile, high uniformity over the wafer, and low damage) and (2) high productivity (high and stable reproducibility and high throughput). In addition, the following critical conditions are required for manufacturing high density devices.

A) Low RIE-lag effect and minimal microloading effect [25].

B) Low electrical damage such as charging-induced gate breakdown and no device degradation due to heavy metal impurity contamination [26].

C) Some new requirements to enable the introduction of unique material such as low-*k* and high-*k* materials [27, 28].

As scaling down proceeded, nanometer-leveled precise control of etching feature has been indispensable for the process requirements. However, numerous trials-and-errors processes have been proceeded in the plasma etching processes

development. As a result, the operation performances were characterized by external parameters, since there has never been the any scientific principle. These requirements above are strongly dependent on the capabilities of etching reactors and the related etching reaction mechanisms. It means that a lot of cost, time and human resource have been spent for applying new technologies to mass production system, because there is no reproducibility between the results from the reactor and those from the mass production reactor.

In order to develop the sophisticated and economically efficient plasma processing, the new concept of plasma process has to be introduced, which is applicable to the process developments for various reactors. As a result, based on those advanced plasma process technology, it could be expected to meet the fast technology development and apply those to mass production with the least cost in a short period.

1.3.1 Need of Plasma Nano-Science for Next Generation Nano-Etching Process

In the reactor, low-temperature plasma generated by a electric discharge has many parameters to be controlled to achieve the process requirement. There are two aspects of the plasma which are important in processes: physical and chemical. The number of the positive and negative charges densities contained in plasma is equal. Because of the higher mobility of the electrons, the surface in contact with the plasma has a negative potential. This electric field induced by the potential reduces the electron current density until the electrical neutrality is maintained by ion current.

The electrical field accelerates the ions to the surface. Many physical effects are induced by the arrival of photons, electrons and ions from the plasma. They may induce sputtering or stress generation on the surface if the energy of the charged particles is sufficient, and the electric field will be normal. Therefore, ions reach the target sample at normal incidence. The chemical effect of plasmas are induced by the chemical active species generated in the plasma. Both the physical and chemical effects are important and should be considered carefully. Their combined effects contribute to the etching process.

When these two effects of plasmas in mind, I may consider their application in microelectronics processing. Basically, the process characteristics are determined by these parameters. In other words, the control of external parameters, such as input power, gas ratio and working pressure, results in the change of internal parameters such as electron density, electron temperature and energy of particles. However, practical process characteristics must be controlled by internal parameters, which have an influence on the process directly. After all, how to control the internal parameters sophisticatedly is a key issue to acquire the advanced properties and the developments of plasma process technologies.

1.3.2 Advanced Process Control (APC)

Advanced process control (APC) has been suggested to improve wafer-to-wafer or lot-to-lot processing quality, because the APC techniques reduce process variability, which is a function of process variability. The APC improves process accuracy utilizing pre- and post-process measurement, modeling of process and equipment trends, and suggesting subsequent process parameter adjustments (i.e. feedback control). Process variability is generally reduced through preprocess measurements and subsequent process parameter adjustment (i.e. feedforward control). Run-to-run process control (R2R) could address to improve within-wafer and within-die variability. In general, process engineers are unwilling to allow dynamic changes in the process recipe [29]. Furthermore, it is necessary that processes are controlled at real time in order to minimize any fluctuations in etching characteristics to suppress any perturbation such as modification of chamber–wall conditions [30].

The APC for plasma processes was previously reviewed by Edgar *et al* [31]. For instance, Shadmehr *et al.* reported the fault detection of CHF_3/O_2 plasmas by utilizing an optical emission spectroscopy and a residual gas analysis [32]. Greve *et al.* demonstrated the real-time feedback control in SiH_4/ NH_3 plasmas by using quadrupole mass spectrometry [33]. Fukasawa *et al.* reported that the fluctuation in etch rates caused by changes in chamber conditions [34].

Condition of reactor wall surface influences the plasma chemistry in the reactor and it has been a great concern for the precise control of plasma etching processing [35-37]. The prior process and/or the exposure of ambient air during the maintenance of reactors could modify the wall surface condition of the wall considerably and then influence the following etching process indirectly via the wall surface memory [38]. Indeed, there are several reports of the reactor-wall's surface loss probabilities of species such as molecular atoms [39–41] and atoms [42–46] by using various diagnostic

techniques such as absorption spectroscopy and appearance mass spectroscopy [47,48].

In our previous study, Nagai *et al*. reported that the behaviors of H and N atom densities influenced much on etching feature [49-53]. Yamamoto *et al*. demonstrated that the control of H and N atom density to improve the plasma etching characteristics of low-*k* organic films [54]. Takahashi *et al.* monitored the absolute densities of H and N atoms in H_2/N_2 plasmas at real-time. They also controlled the atom densities to intended values by a feedback controller [55]. However, they could not control with their feedback system the circumstance perturbation caused by unintentional influences. Namely, in actual plasma processes, the temporal change of plasma conditions caused by memory effect, whose the etching product or reactor surface influenced the gaseous species densities [30]. Thus, it required a real time process control in feature profiles but it has not been realized so far.

1.4 Objective and composition of this dissociation

The findings of the section of introduction, with regard to advanced plasma processing for etching and deposition technologies, indicate the necessity of a new plasma process technology development. The fabrication of microelectronic devices is becoming more mature, resulting from tightening of process specifications. In recent years, there has been tremendous interest in flexible electronics due to a variety of merits such as lightweight, abundance and cost-effectiveness of organic materials. Besides the obvious applications of flexible electronics in flat panel displays, flexible circuits are also promising for use in such applications as radio frequency identification (RFID) tags and other disposable electronic devices. In other to fabricate the devices on flexible substrates, it is necessary to obtain highly stabilized film properties needed for designing the circuit and realize the sophisticated etching performance with the reproducibility as scaling-down and high integration. However, advanced process development for deposition and etching technologies has been slowly incorporated into the industry due to very low reproducibility, and is now becoming a necessity for processes which are operating at or near their limits. Deposition and etching processes are indispensible for the fabrication of microelectronics, which has been innovatively developed to improve the process capability.

1.5 References

[1] R. Kumar and G. Hinton, "A Family of 45nm IA Processors," ISSCC Dig. Tech. Papers, Paper 3.2, Feb. (2009).

[2] T. Kikkawa, Oyo Buturi, 68, 1215 (1999).

[3] A. Aviram, and M. Ratner, Chem. Phys. Lett. 29, 277 (1974).

[4] C. Joachim, J. Gimzewski, and A. Aviram, Nature 408, 541 (2000).

[5] C. K. Chiang, C. R. Fincher, Jr., Y. W. Park, A. J. Heeger, H. Shirakawa, E. J. Louis, S. C. Gau, and Alan G. MacDiarmid, Phys. Rev. Lett. 39, 1098 (1977).

[6] J. H. Schön, S. Berg, Ch. Kloc, and B. Batlogg, Science 287,1022 (2000).

[7] R. H. Havemann, and J. A. Hutchby, Proceedings of the IEEE, 89, 586 (2001).

[8] K. Mistry, et al., "A 45nm Logic Technology with High-κ + Metal-Gate Transistors, Strained Silicon, 9 Cu Interconnect Layers, 193nm Dry Patterning, and 100% Pb-free Packaging," IEDM Tech. Dig., pp. 247-250, Dec. (2007).

[9] C. Auth, et al., "45nm High-k+Metal gate Strain-Enhanced Transistors," Symp. VLSI Technology, pp. 128-129, June (2008).

[10] K. Badeker, Ann. Phys. 22, 749 (1907).

[11] I. Hamberg and C.G. Granqvist, J. Appl. Phys. 60, R123 (1986).

[12] J.J. Cuomo and S.M. Rossnagel, Handbook of Ion Beam Processing Technology, Noyes Publications, (1989).

[13] Rossnagel SM, Sputter Deposition, In Sproul WD, Legg KO, editors, (1995).

[14] A. Belkind, A. Freilich, and R. Scholl, J. Vac. Sci. Technol. A 17,1934 (1999).

[15] G. Este and W.D. Westwood, J. Vac. Sci. Technol. A 6, 1845 (1988).

[16] D. A. Glocker, J. Vac. Sci. Technol. A 11, 2989 (1993).

[17] I. Safi, Surf. Coat. Technol. 127, 203 (2000).

[18] J. Sellers. Surf. Coat. Technol. 98, 1245 (1998).

[19] P. J. Kelly, P. S. Henderson, R. D. Arnell G. A. Roche, and D. Carter, J. Vac. Sci.

Technol. A 18, 2890 (2000).

[20] J. Musil, J. Lestina, J. Vlcek, and T. Tolg, J. Vac. Sci. Technol. A 19, 420 (2001).

[21] A. Raveh, M. Weiss, and R. Shneck, Surf. Coat. Technol. 11, 1263 (1999).

[22] S. Peter, U.F. Richtera, R. Tabersky, and U. König, Thin Solid Films 377, 430 (2001).

[23] A. Anders, Surt. Coat. Technol. 183, 301 (2004).

[24] G. E. Moore, Electronics 38, 114 (1965)

[25] R. A Gottscho, C. W. Jurgensen, and D. J. Vitkavage, J. Vac. Sci. Technol. B 10, 2133 (1992).

[26]Y. Yoshida and T. Watanabe, Proc. 5th Symp. Dry Process, 1983, p.4

[27] Y. J. Lim, S. K. Lee, and H. J. Kim, J. Vac. Sci. Technol. A18, 1216, (2000).

[28] P. C. Andricacos, C. Uzoh, J. O. Duckovic, J. Horkans, and H. Deligianni, IBM J. Res. Dev. 42, 567 (1998).

[29] Book: Run-to-Run Control in Semiconductor Manufacturing, ed. by James Moyne, Enrique del Castillo, Arnon M. Hurwitz (CRC Press, USA, 2001)

[30] T. Suzuki, K. Takeda, H. Kondo, K. Ishikawa, M. Sekine, and M. Hori: Jpn. J. Appl. Phys. **Submitted** (2013).

[31] T. F. Edgar, S. W. Butler, W. J. Campbell, C. Pfeiffer, C. Bode, S. B. Hwang, K. S. Balakrishnan, and J. Hahn: Automatica **36** (2000) 1567.

[32] R. Shadmehr, A. Angell, P. B. Chou, G. S. Oehrlein, and R. S. Jaffe: J. Electrochem. Soc. **139** (1992) 907.

[33] D. W. Greve, T. J. Knight, X. Cheng, B. H. Krogh, and M. A. Gibson: J. Vac. Sci. Technol. B **14** (1996) 489.

[34] M. Fukasawa, A. Kawashima, N. Kuboi, H. Takagi, Y. Tanaka, H. Sakayori, K. Oshima, K. Nagahata, and T. Tatsumi: Jpn. J. Appl. Phys. **48** (2009) 08HC01.

[35] G. Cunge, M. Kogelschatz, and N. Sadeghi: Plasma Sources Sci. Technol. **13** (2004) 522.

[36] M. Schaepkens, R. C. M. Bosch, T. E. F. M. Standaert, G. S. Oehrlein, and J. M. Cook: J. Vac. Sci. Technol. A **16** (1998) 2099.

[37] T. W. Kim and E. S. Aydil: J. Electrochem. Soc. **150** (2003) G418.

[38] A. Agarwal and M. J. Kushner, J. Vac. Sci. Technol. A **26** (2008) 498.

[39] N. Itabashi, K. Kato, M. Magane, S. Naito, T. Goto, A. Matsuda, C. Yamada, and E. Hirota: Jpn. J. Appl. Phys. **29** (1990) L505.

[40] Y. Hikosaka, H. Toyoda, and H. Sugai: Jpn. J. Appl. Phys. **32** (1993) L690.

[41] K. Sasaki, K. Usui, H. Furukawa, C. Suzuki, and K. Kadota: Jpn. J. Appl. Phys. **37** (1998) 5047.

[42] J. P. Booth and N. Sadegi: J. Appl. Phys. **70** (1991) 611.

[43] Y. Hatanaka and S. Mickramanayaka: Vacuum **35** (1992) 894. [in Japanese]

[44] S. Takashima, M. Hori, T. Goto, A. Kono, and K. Yoneda: J. Appl. Phys. **90** (2001) 5497.

[45] M. Hori and T. Goto: Appl. Surf. Sci. **253** (2007) 6657.

[46] G. A. Curley, L. Gatilova, S. Guilet, S. Bouchoule, G. S. Gogna, N. Sirse, S. Karkari, and J. P. Booth: J. Vac. Sci. Technol. A **28** (2010) 360.

[47] S. Takashima, A. Kono, M. Ito, K. Yoneda, M. Hori, and T. Goto: Appl. Phys. Lett. **75** (1999) 3929.

[48] S. Takashima, S. Arai, A. Kono, M. Ito, K. Yoneda, M. Hori, and T. Goto: J. Vac. Sci. Technol. A **19** (2001) 599.

[49] M. Sekine, Appl. Surf. Sci. **192** (2002) 270.

[50] G. S. Oehrlein, R. J. Phaneuf, and D. B. Graves: J. Vac. Sci. Technol. B **29** (2011) 010801.

[51] M. Fukasawa, T. Tatsumi, T. Hasegawa, S. Hirano, K. Miyata, and S. Kadomura: Proc. on Dry Process Symposium (Tokyo, 1999) p. 221.

[52] Y. Morikawa, S. Yasunami, W. Chen, T. Hayashi, and T. Uchida: J. Vac. Sci. Technol. **A** 19 (2001) 1747.

[53] Y. Morikawa, T. Hayashi, and T. Uchida: Jpn. J. Appl. Phys. **42** (2003) 1441.

[54] H. Yamamoto, H. Kuroda, M. Ito, T. Ohta, K. Takeda, K. Ishikawa, H. Kondo, M. Sekine, and M. Hori: Jpn. J. Appl. Phys. **51** (2012) 0.516202.

[55] S. Takahashi, R. Kawauchi, S. Takashima, S. Den, T. Katagiri, H. Kano, T. Ohta, M. Ito, T. Suzuki, K. Takeda, and M. Hori: Jpn. J. Appl. Phys. **51** (2012) 076502.

Chapter 2 Plasma Diagnostic Techniques for Evaluating the Internal Parameters and Film Analysis Methods

2.1 Introduction

In the microelectronic industry, plasma processing is widely used as thin films deposition process and etching process. Those plasma process applications extend surface modification, display fabrication, solar sell fabrication, and many other areas. To understand the plasma surface reactions, diagnostic analysis tools have been developed to analyze the concentrations of reactive species and particles in the plasma. In this chapter, evaluation techniques of plasma diagnostic are discussed such as vacuum ultra-violet absorption spectroscopy (VUVAS), optical emission spectroscopy (OES). On the basis of these diagnostic analyses, the development of plasma nano-technology could be expected to realize for the next generation process.

2.2 Vacuum Ultraviolet Absorption Spectroscopy (VUVAS)

2.2.1 Theory of Absorption Spectroscopy

If a beam of the light passes through a plasma, the intensity of the light transmitted the plasma is given as follows [1],

$$I(\nu) = I_0(\nu)\exp[-k(\nu)L], \tag{2.1}$$

where ν is the frequency of the light, $I(\nu)$ and $I_0(\nu)$ are the transmitting light intensity and the incident light intensity, respectively. $k(\nu)$ is the absorption, and L is the length of the absorption.

The broadening of the absorption line-profile is induced by the broadening of the absorption coefficient. These broadening are caused by the natural broadening, Doppler effect broadening, Lorentz broadening, Holtsmark broadening, and Stark effect broadening. Natural broadening is induced by the finite lifetime of the exited state. Doppler effect broadening is induced by the motions of the atoms. Lorentz broadening is induced by collisions with foreign gases. Holtsmark broadening is induced by collisions with other absorption atoms of the same kind. Stark effect broadening is induced by collisions with electrons and ions.

When a beam of the light passing through an atoms layer at the length of dL, there are N_l normal atoms per cm^3. At the the frequency range between ν and $\nu+d\nu$, dN_l are capable of absorbing and N_u excited atoms of which dN_u are capable of emitting. At the point of view that spontaneous re-emission takes place in all direction, the effect of it is negligible. Thus, the decrease of the light intensity is given by

$$-[I(\nu)]d\nu = dN_l dL\rho(\nu)B_{lu}h\nu - dN_u dL\rho(\nu)B_{ul}h\nu, \tag{2.2}$$

where $\rho(\nu)$ is the radiation energy density given by $I(\nu)=c\rho(\nu)$, (c: light velocity). B_{lu} and B_{ul} are Einstein B coefficient from ground state l to excited state u and from l to u, respectively. h is Planck's constant. Rewriting Eq. (2-2), we obtain

$$-\frac{1}{I(\nu)}\frac{d[I(\nu)]}{dL}d\nu = \frac{h\nu}{c}(B_{lu}dN_l - B_{ul}dN_u), \qquad (2.3)$$

The left-hand term can be recognized as $k(\nu)d\nu$ defined by Eq. (2-1), Eq. (2-3). The equation can be calculated as follows

$$k(\nu)d\nu = \frac{h\nu}{c}(B_{lu}dN_l - B_{ul}dN_u) \qquad (2.4)$$

And integrating over the range of whole absorption line,

$$\int k(\nu)d\nu = \frac{h\nu_0}{c}(B_{lu}N_l - B_{ul}N_u), \qquad (2.5)$$

where ν_0 is the frequency at the center of the line. With applying Einstein A coefficient, the equation can be calculated as follows

$$\int k(\nu)d\nu = \frac{c^2}{8\pi\nu_0^2}\frac{g_u}{g_l}AN_l(1-\frac{g_l N_u}{g_u N_l})$$

$$\cong \frac{c^2}{8\pi\nu_0^2}\frac{g_u}{g_l}AN_l \qquad (N_u << N_l), \qquad (2.6)$$

where g_l and g_u are the statical weights of the lower and upper level, respectively. Therefore, density N_l can be estimated by measuring $I_0(\nu)$ and $I(\nu)$.

When incoherent light is used as the light source, the intensity of a beam of the light is the integrated over the frequency as following

$$I_0 = \int e_0 f_0(\nu) d\nu , \tag{2.7}$$

$$I_a = \int e_0 f_0(\nu)\{1 - \exp[-k_0 f_a(\nu)L]\} d\nu , \tag{2.8}$$

where I_0 and I_a are the intensities of the incident light and the absorption, respectively. $f_0(\nu)$ is the emission line-profile function for the light source. e_0 is the emission intensity of the light source at a center frequency of $f_0(\nu)$. $f_a(\nu)$ is the absorption line-profile function. And k_0 is the absorption coefficient at the center frequency of $f_a(\nu)$. Thus, the absorption intensity $A(k_0L)$ is given by the following formula

$$A(k_0 L) = 1 - \frac{I_a}{I_0} = \frac{\int f_0(\nu)\{1 - \exp[-k_0 f_a(\nu)L]\} d\nu}{\int f_0(\nu) d\nu} . \tag{2.9}$$

From $A(k_0L)$ obtained by measurement, k_0 is determined by assuming the line-profile function $f_0(\nu)$ and $f_a(\nu)$. Then, the number density of state l, N_l, is estimated by using Eq. (2.2-6) as

$$N_l = \frac{8\pi\nu_0^2}{c^2} \frac{g_l}{g_u} \frac{1}{A} k_0 \int f_a(\nu) d\nu . \tag{2.10}$$

2.2.2 Measurements of Absolute Densities of H and N Atoms with Micro-Discharge Hollow Cathode Lamp (MHCL)

Recently, the measurement system using the VUVAS with micro-discharge hollow cathode lamp (MHCL) as a light source has developed to measure the absolute densities such as H [2] and N [3] atoms in the ground state. Transition lines used for measurement of the absolute densities of H and N atoms are Lyman α at 121.6 nm, $^4P_{5/2}$-$^4S^0_{3/2}$, $^4P_{3/2}$-$^4S^0_{3/2}$ and $^4P_{1/2}$-$^4S^0_{3/2}$ at 120.0 nm and $^3S^0$-$2p^4$ $^3P_2$ at 130.217 nm, respectively. Each emission of these transition lines can be obtained by the H_2 and N_2 plasma, respectively. However, these light emissions are induced by two major processes [4-6]. One is the direct excitation of atoms in the ground state by the electron impact.

$$X + e \rightarrow X^* + e \rightarrow X + h\nu + e \qquad (2.11)$$

, where X is the atom in the ground state, X^* is X atoms in the excited state. This reaction is responsible for the production of slow excited X^* atoms. The other is the dissociative excitation of molecules in the ground state by the electron impact.

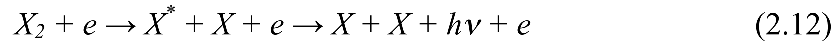

$$X_2 + e \rightarrow X^* + X + e \rightarrow X + X + h\nu + e \qquad (2.12)$$

, where X_2 is the molecule in the ground state. This reaction can produce fast excited X atoms that produce a large Doppler broadening. Therefore, the line profile of the atom emission consists of two different components of velocity distribution induced by these two different excitation processes. Thus, it is difficult to estimate the line profile of the atom emission. To solve this problem for the absolute atom density measurement, a high pressure MHCL was developed as a light source for VUVAS in our research group.

The merits of the MHCL are expected (i) light emission with minimizing the Doppler shift, (ii) pure atom emission and (iii) point-source-like light emission. (i) Since the fast excited atom arising from dissociative excitation of molecules should be thermalized before they emit light, the line profile of the atom emission does not involve a large Doppler shift. (ii) The hollow cathode has a high current density because of its small size as 0.1 mm diameter. This high current density is favorable for attaining a high molecules dissociation and obtaining pure atom emission spectrum. (iii) A point-source-like emission can be attained using an appropriate lens system, and efficiently coupled to the entrance slit of a monochromator. In addition, the size of the lamp is compact, and the lamp is operated by a dc power source with inexpensive cost.

The cathode consists of a plate made of cupper with 0.5 mm thickness and a through-hole hollow of 0.1 mm in diameter. The anode is wire made of tungsten, and is located near the hollow. Helium (250 sccm) and a small amount of H_2 or N_2 mixed helium gas (5 sccm) were used, at a total gas pressure of 0.1 MPa.

2.3 Optical Emission Spectroscopy (OES)

In the plasma, many optical emissions are observed from excited species (e.g. atoms and molecules) generated by electron collision, dissociation, impact of other excited species, photon absorption, etc. Those species can be identified by the photon energy of the optical emission. Generally, electron impact excitation of the ground state frequently occurs in the plasma, and it is given by

$$e + X \rightarrow X^{*} + e\,, \qquad (2.13)$$

where X is the species of interest. Subsequently after the excitation, de-excitation is followed by the photon emission as,

$$X^{*} \rightarrow X + h\nu\,. \qquad (2.14)$$

The optical emission intensity induced by the transition from the excited state to the ground state can be calculated as following

$$I_x \propto n_e n_X \int \sigma_X(\varepsilon) v(\varepsilon) f_e(\varepsilon) d\varepsilon = k_{eX} n_e n_X\,, \qquad (2.15)$$

where n_e is the electron density, n_X is the concentration of X, $\sigma_X(\varepsilon)$ is the collision cross section for the electron impact excitation of X as a function of electron energy ε, $v(\varepsilon)$ is the electron velocity and $f_e(\varepsilon)$ is the electron energy distribution function (EEDF). $k_eX(\varepsilon)$ is the excitation rate coefficient for X^* by the electron impact on X. On the assumption that k_{eX} and n_e are constant, the intensity of the light emission is proportional to the species concentration. However, both of them are generally difficult to be constant because they are easily affected by the experimental conditions, and varied in the

plasma processing. Thus, optical emission spectroscopy (OES) is widely used to compare the emission intensities and the species concentration. To assume that emissions from exited states, it is necessary that the emissions are proportional to the same species concentration in the ground state. Therefore, actinometric optical emission spectroscopy (AOES) technique is widely applied to estimate relative species concentration in the ground state [7-13].

Optical emission spectra are measured by a monochromator with a photomultiplier tube (PMT). In a monochromator, the light intensity is detected through the exit slit by PMT.

A measured spectral line has a certain width. The full width at half maximum (FWHM) of the measured spectral line is determined by various factors such as (i) natural broadening, (ii) Doppler broadening, (iii) pressure broadening, (iv) Stark broadening, and (v) instrumental broadening (instrumental function).

(i) The natural broadening gives a Lorentzian line shape. But it is generally negligible because it is very small.

(ii) Doppler broadening gives a Gaussian line shape, and it depends on the temperature of the species. Doppler broadening is calculated as following,

$$f_D(\nu) = \exp\left[-\left\{2\sqrt{\ln 2}\,\frac{(\nu-\nu_0)}{\Delta\nu_D}\right\}^2\right], \tag{2.16}$$

with

$$\Delta\nu_D = \frac{2\nu_0}{c}\sqrt{\frac{2RT\ln 2}{M}}, \tag{2.17}$$

Where $\Delta\nu_D$ is the FWHM of the Doppler broadening, ν_0 is the center frequency, c is the velocity of light, R is the gas constant, T is the gas temperature, M is the mass number.

(iii) Pressure broadening gibes Lorentzian function, and it depends on pressure around the species. It is calculated as following,

$$f_P(\nu) = \frac{\Delta\nu_P}{2\left\{4(\nu - \nu_0)^2 + \left(\frac{\Delta\nu_P}{2}\right)^2\right\}}, \quad (2.18)$$

with

$$\Delta\nu_P = \frac{1}{\pi} z = \frac{1}{\pi} \cdot n \cdot \sigma \cdot \sqrt{\frac{8RT}{\pi\mu}}, \quad (2.19)$$

where ν_P is the FWHM of the pressure broadening, z is the collision frequency, n is the concentration of the species, σ is the collision cross section, μ is the reduced mass.

(iv) Stark broadening is induced by charged particles such as electrons and ions, and it depends on the electric field. Therefore, it derives the electron density.

(v) The instrumental broadening is induced by difference of the spectrometer performance used in the experiment, and it depends on the performance itself. To determine the instrumental function, a light source with enough sharp spectral lines such as a low-pressure mercury lamp is generally used. The spectrum gives

the convolution of Gaussian and Lorentzian functions, and it results in a Voigt profile. Voigt function is calculated as following,

$$f_V(v) = \frac{a}{\pi} \int \frac{\exp(-y^2)}{a^2 + (\omega + y)^2} dy \,, \tag{2.20}$$

with

$$a = \frac{\Delta \nu_L}{\Delta \nu_G} \sqrt{\ln 2} \,, \tag{2.21}$$

and

$$\omega = \frac{2(\nu - \nu_0)\sqrt{\ln 2}}{\Delta \nu_G} \,, \tag{2.22}$$

where $\Delta\nu_L$ is the FWHM of the Lorentz broadening, $\Delta\nu_G$ is the FWHM of the Gaussian broadening.

2.4 Methods for Evaluating Films Deposited and Etched

2.4.1 Spectroscopic Ellipsometry

Ellipsometry measures a polarization change of light reflects and transmits from a material structure, and it is represented as amplitude ratio Ψ, and phase difference Δ. The measured result depends on thickness and optical properties of the target materials. In addition, the other material property such as composition, crystallinity, roughness, doping concentration associate with a change in optical response Thus, ellipsometry is widely used as the measurement method of these characteristics. Discussion of the waves's electric field behavior, also known as polarization, in space and time is adequate for the measurement. A wave propagating along the z-direction can be described with its x- and y- components, because a wave of the electric field and the propagation direction are always orthogonal, Polarized light is known that electric field follows the specific path and traces out the distinct shape at any point. The light will be linearly polarized when the two waves of orthogonal light are in-phase. The orientation is determined by relative amplitudes. The light is circularly polarized when the orthogonal light are 90° out-of-phase and equal amplitude. The light is elliptically polarized when orthogonal waves of arbitrary amplitude and phase are combined.

Maxwell's equations should be satisfied when the light interacts with a material. The equations lead the boundary conditions at the interface. The light will reflect and refract at the interface with the equal angle between the incident angle (*fi*) and the reflected angle (*fr*). Incident light is refracted at an angle (*ft*) calculated as following:

$$n_0 \sin(\Phi_i) = n_i \sin(\Phi_t) \tag{2.27}$$

The same occurs at each interface, and the boundary conditions provide the other solutions for electric fields between parallel and perpendicular to the target sample surface. Thus, the light can be separated into two orthogonal components with relation of the plane. Electric fields that are parallel and perpendicular to the plane can be considered as p- and s- polarized components, respectively. Each of the two components is independent and can be separated for the calculation. Thus the amount of reflected light and transmitted light at an interface between materials can be calculated as following:

$$r_s = \left(\frac{E_{or}}{E_{0i}}\right)_s = \frac{n_i \cos(\Phi_i) - n_t \cos(\Phi_t)}{n_i \cos(\Phi_i) + n_t \cos(\Phi_t)} \tag{2.28}$$

$$r_p = \left(\frac{E_{or}}{E_{0i}}\right)_p = \frac{n_t \cos(\Phi_i) - n_i \cos(\Phi_t)}{n_i \cos(\Phi_t) + n_t \cos(\Phi_i)} \tag{2.29}$$

$$t_s = \left(\frac{E_{ot}}{E_{0i}}\right)_s = \frac{2 n_i \cos(\Phi_i)}{n_i \cos(\Phi_i) + n_t \cos(\Phi_t)} \tag{2.30}$$

$$t_p = \left(\frac{E_{ot}}{E_{0i}}\right)_p = \frac{2 n_i \cos(\Phi_i)}{n_i \cos(\Phi_t) + n_t \cos(\Phi_i)} \tag{2.31}$$

Tracking the relative phase of each component determines the overall reflected or transmitted light. For this purpose, the film phase thickness can be defined as following:

$$\beta = 2\pi\left(\frac{t_1}{\lambda}\right) n_1 \cos(\Phi_1) \tag{2.32}$$

Ellipsometry is interested in the change of *p*- and *s*- components relationships upon reflection or transmission. In this manner, the reference light is introduced into the experiment. A known light of polarization reflected or transmitted at the interaction of the sample is measured. The change of the light polarization is commonly written as following:

$$\rho = \tan(\psi)e^{i\Delta} \tag{2.33}$$

The incident light is linear to the p- and s- components. The ellipsometry measures those change of reflected light undergone amplitude and phase changes.

The thickness of the film is determined by interaction between reflecting light at the surface and traveling light through the film. Amplitude and phase information can be measured by the interference of the rejoining light. The phase information Δ is sensitive to films thickness down to sub-monolayer, ranges from sub-nanometers to a few micrometers. If the films is thicker than tens of microns, interference oscillations become difficult to resolve, except longer infrared wavelengths. In this case, Other measurement techniques are preferred.

2.4.2 X-Ray Photoelectron Spectroscopy (XPS)

X-ray photoelectron spectroscopy (XPS) provides compositional information and chemical information. It is the most widely used as surface-analytical technique because it is easy to operate, and available the commercial equipment. The surface is analyzed by irradiation with soft X-ray photons. When a X-ray photon energy *hv* interacts with an electron at the surface of target material in a level X with the binding energy E_B, the entire energy of photon is transferred to the electron. The kinetic energy of a photoelectron ejected with is calculated as following

$$E_{kin}\,({}_{hv}, X) = hv - E_B - \Phi_s \qquad (2.34)$$

where Φ_s is work function term. And it is a small and almost constant. *hv* must be larger than E_B. The ejected electron term come from not only a core level but also the valence band. However, most attention in XPS is focused on electrons in the core levels. The measurement of the kinetic energies enables elemental analysis because of the reason that there are no two elements sharing the same electronic binding energy set. The changes of E_B indicate the chemical environment of an atom, and it can be followed by monitoring changes of E_{kin} from the Eq. (2.34). Thus, the measurement of photoelectron kinetic energy leads the chemical information, and XPS can be used for all elements analysis except hydrogen and helium in the periodic table.

Although XPS is concerned the electron ejection by other processes such as photoelectron leaves behind a core hole. In the creation of the hole, the hole created in the K-shell gives a photoelectron with kinetic energy (hv-E_K). The hole is filled by an electronic transition that comes from the unresolved L_{23} shell. The energy (E_K-E_{L23}) associated with the transition can be dissipated as a X-ray photon, an electron in the same shell or that in a higher shell.

The second process is called the Auger process [15], and the ejected electron is called an Auger electron. The kinetic energy can be calculated as following:

$$E_{kin}(KL_1L_{23}) = E_K - E_{L1} - E_{L23} - E_{inter}(L_1L_{23}) + E_R - \Phi_s \qquad (2.35)$$

Where $E_{kin}(KL_1L_{23})$ is the interaction energy between the holes in the L_1 and L_{23} shell. E_R is the sum of the intra-atomic relaxation energies.

2.5 References

[1] A. C. G. Mitchell and M. W. Zemansky, Resonance Radiation and Exited Atoms (Cambridge, London 1961).

[2] S. Takashima, M. Hori, T. Goto, A. Kono, M. Ito and K. Yoneda, Appl. Phys. Lett. 75, 3929 (1999).

[3] S. Takashima, S. Arai, M, Hori, T. Goto A. Kono, M. Ito, and K. Yoneda, J. Vac. Sci. Technol. A 19, 599 (2001).

[4] R. S. Freund, J. A. Schiavone, and D. F. Brader, J. Chem. Phys. 64, 1122 (1976).

[5] K. Ito, N. Oda, Y, Hatano, and T. Tsuoi, Chem. Phys. 21, 203 (1977).

[6] S. Djurovic and J. R. Roberts, J. Appl. Phys. 74, 6558 (1993).

[7] J. W. Corburn and M. Chen, J. Appl. Phys. 51, 3134 (1980).

[8] Y. Kawai, K. Sasaki, and K. Kadota, Jpn. J. Appl. Phys. 36, L1261 (1997).

[9] R. E. Walkup, K. L. Saenger, and G. S. Sewyn, J. Chem. Phys. 84, 2668 (1986).

[10] H. M Katsch, A. Tewes, E. Quandt, A. Goehlich, T. Kawetzki, and H. F. Dobele, J. Appl. Phys. 88, 6232 (2000).

[11] S. F. Durrant and M. A. B. Moraes, J. Vac. Sci. Technol. A, 13, 2513 (1995).

[12] S. F. Durrant and M. A. B. Moraes, J. Vac. Sci. Technol. A , 16, 509 (1998).

[13] A. Gicquel, M. Chenevier, Kh. Hassouni, A. Teserepi, and M. Dubus, J. Appl. Phys. 83, 7504 (1998).

[14] K. Siegbahn, C. Nordling, A. Fahlman, R. Nordberg, K. Hamrin,J. Hedman, G. Johnsson, T. Bergmark, S.-E. Karisson, I. Lindgreen, B. Lindberg: ESCA: Atomic, Molecular, and Solid Sate Structure Studied by Means of Electron Spectroscopy. Almqvist and Wiksells, Uppsala 1967.

[15] P. Auger, J. Phys. Radium 6, 205 (1925).

Chapter 3 Realization of Nano-features by Nano-etch process

3.1 Introduction

In ULSI processing, the number of device integrations is growing exponentially in accordance with Moore's law and the feature size is scaled down dramatically [1,2]. In the technology generation of 10-nm half-pitch and beyond, fluctuation of feature size and shape at subnanometer-scale become an essential factor to determine the device performance. To achieve accurate nanoscale patterning for sub-10-nm devices, some paper discussed etching feature of inorganic material with a few nm mask [3,4]. However, there is no report of the organic material etching with those scale patterning. This is because mechanical strength of organic material used as an interlayer dielectric is generally low [6~8]. In previous studies, the correlation among the behaviors of H and N atom densities and the etching characteristics of the organic films was investigated [17-22]. From the results, it was found that the chemical reaction with by H atoms resulting in HCN and C_xH_y of by-products and the bombardment of ions, such as N_2H^+ and NH_x^+, enhanced the etching rate of organic films, while the CN layer produced by N atoms protected the pattern sidewall from spontaneous chemical etching [10, 11,16, 23-25]. Moreover, it was clarified that etching characteristics of organic film depend not only H and N atom densities but also the substrate temperature.

In this chapter, characteristics of the organic films etching deposited nm 10 nm Pt particles employing a 100-MHz excited capacitively coupled plasmas (CCP) reactor with a 2-MHz biasing employing H_2 and N_2 mixture gases were investigated. In addition, I proposed a scheme to control a fine pattern profile of organic films precisely by the Pt particles deposition. I believe this technique can be applied for etching process of general organic materials also.

3.2 Experimental Details

3.2.1 Metalorganic Supercritical Chemical Fluid Deposition (MOCFD)

The apparatus for the supercritical chemical fluid deposition consists of two reactors, and was developed *in house*. The deposition procedure used is as follows. Both the upper and lower reactors were evacuated until a pressure of approximately 10 Pa was attained. Then, 5 ml of a precursor of trimethyl(methylcyclopentadienyl)Pt(IV) ($C_5H_4CH_3Pt(CH_3)_3$, Sigma-Aldrich, CAS 94442-22-5) with a concentration of 1 wt. % diluted in hexane (Sigma-Aldrich, CAS 110-54-3) was introduced into the upper reactor, where it was mixed with supercritical CO_2 by the rotation of a propeller under 10 MPa and 70ºC. The wafer was placed on a stage in the lower reactor, and supercritical CO_2 was filled at 10 MPa and 130ºC. The stage was heated to the deposition temperature, ranging typically from 120ºC to 230ºC. After the precursor was mixed for 10 min, the gate valve in the apparatus was opened to transfer the precursor from the upper to the lower reactor; this represents the beginning of the deposition. Usually the deposition process took 30 min.

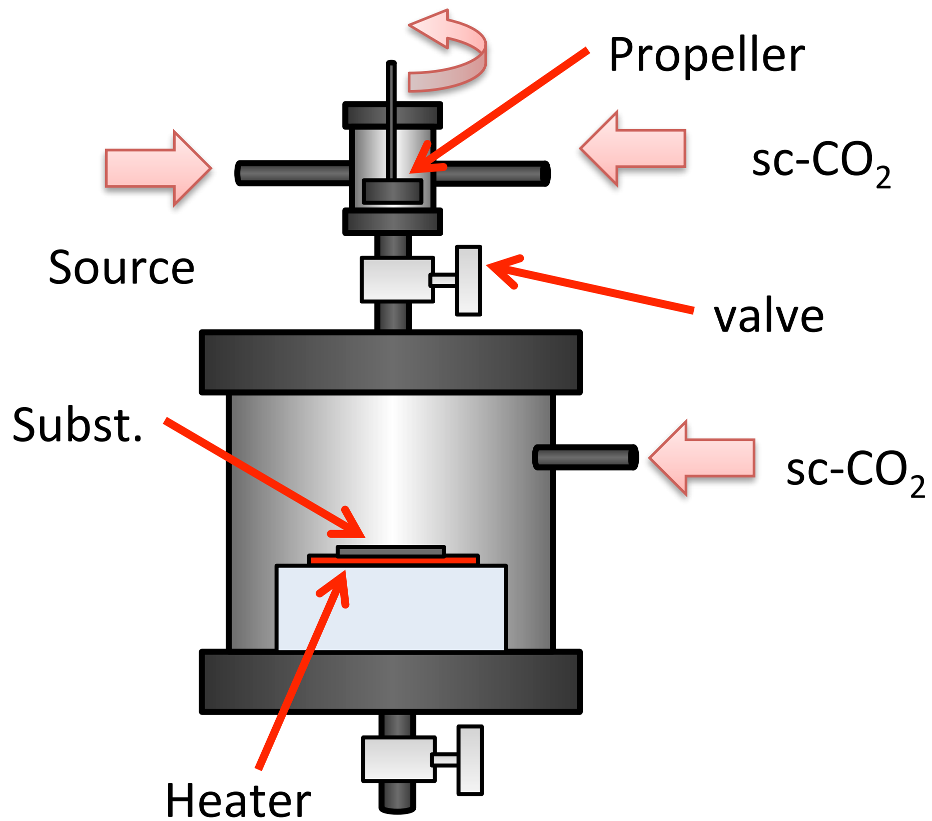

Figure 3.1 Metalorganic supercritical chemical fluid deposition (MOCFD) system.

3.2.2 Dual-Frequency Capacitively Coupled Plasma Etcher

The samples covered with Pt particles were processed by plasma etching in an *in-house* reactor of a dual-frequency coupled plasma etcher. 100-MHz power at 400 W was applied to the top electrode and 2-MHz power at 200 W was applied to the bottom electrode. The sample wafer set on the bottom electrode that was maintained at 60ºC by the circulating coolant (in order to obtain appropriate feature shapes, but at 20ºC as a standard for processes with an SiO_2 mask). Hydrogen with a flow rate of 75 sccm and nitrogen of 25 sccm were introduced into the chamber and maintained at a pressure of 2 Pa. The etch rate of the organic film was 102 nm/min and the etching time was typically 120 s.

Organic low dielectric films (Dow Chemical, SiLK™) [3] with the thickness of 200 nm on Si substrate were etched. The film thickness was measured in real time by spectroscopic ellipsometer (M-200F™, J.A. Woollam Inc.). All spectra were recorded from λ=300 to 800 nm. The wavelength dependence of the refractive index was approximated by a Cauchy model. H and N atom densities (transitions are Lyman α at 121.6 nm for H atoms and $^4P_{5/2}$-$^4S^0_{3/2}$, $^4P_{3/2}$ -$^4S^0_{3/2}$ and $^4P_{1/2}$-$^4S^0_{3/2}$ at 120.0 nm for N atoms) were measured by a vacuum ultraviolet absorption spectroscopy (VUVAS) system with a high pressure micro-discharge hollow cathode lamp (MHCL) [4, 5].

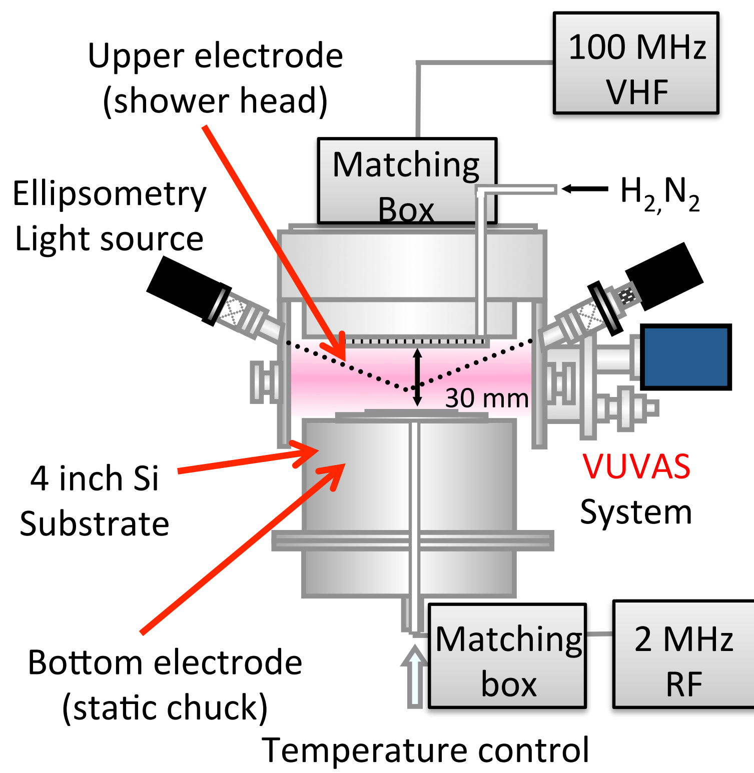

Fig 3.2 Dual-frequency coupled plasma etcher.

3.3 Results and Discussion

3.3.1 Fabrication of Organic Rods Armored by Pt Nanoparticles

In nanoscale fabrication, photolithographic mask patterning followed by etching is currently used but there are associated issues for forming sub-nanoscale pattern masks. To overcome this, other new approaches, such as molding, printing, and template self-assembly, are required. Recently, by combining the use of photolithography along with block copolymers, it has become possible to produce patterns on the tens-of-nm scale [3]. However, no photolithographic patterning technique with true nm-scale ability has not been reported so far.

Bottom-up approaches are well-established to realize true nm-scale, for example in carbon nano-materials such as carbon nanotubes (CNTs) [5]. In recent progress, material compositions and structures obtained through the bottom-up approach have suggested device and fabrication strategies that are not possible with top-down methods [6]. These have been proposed to be used as field emission sources, on the basis of their high aspect ratios, small radii and curvatures, and high chemical stability [7-11]. Conventional fabrication methods of CNTs include arc discharge [12], laser ablation [13], and chemical vapor deposition (CVD) [14-18]. CVD growth generally necessitate temperatures higher than 500ºC, therefore such growth methods cannot be applied for device fabrication on organic substrates.

In contrast, the top-down approach provides the ability to fabricate nano-structured materials at room temperature or at temperatures less than the melting point of organics, typically around 200ºC. In addition, organic materials show characteristics of mechanical weakness for realization of sub-nanometer-features. Here, I propose the use of nanoscale metallic particles as a resist mask for plasma-etching as a top-down approach for fabricating devices on organic substrates.

Our group has reported that metalorganic supercritical chemical fluid deposition (MOCFD) of platinum particles with a size of 2 nm could be deposited on graphitic carbon materials [19-21]. I applied Pt nanoparticles as the etching mask for fabricating nano-pillars (rods).

Figure 3.3 (a) shows scanning electron microscope (SEM) images of organic film with Pt particles formed by MOCFD with the substrate temperature of 150°C. The size distribution of Pt particles is also shown in Fig. 3.3 (b) for different substrate temperatures of (i) 150°C, (ii) 170°C, (iii) 190°C. As the substrate temperature was increased, the mean diameters of the Pt particles shifted slightly to a higher value, from 2.97 to 3.85 nm. This indicated that the substrate temperature of MOCFD affects the diameter of the organic rods.

Figure 3.4 (a) shows cross-sectional SEM images of organic films after they were etched for 120 s with Pt particles subsequently deposited by MOCFD with a substrate temperature of 190°C, similar to Figure 1(b). The organic film with a thickness of 200 nm was etched off entirely and the substrate was exposed. Organic rods were observed with a typical diameter of 10.2 nm (aspect ratio 18.7). Vertically aligned organic-pillars forming under a vacuum environment; I speculate that deformation takes places during air exposure since the organic materials are mechanically weak. Surprisingly, under plasma etching, lateral etching was prevented and the sidewall of the organic rods was not eroded. Organic rods with nanoscale diameter were thus successfully formed by the top-down approach. However, there remains the question of why the sidewall was protected from erosion.

I speculated that the Pt particles should play a role of the mask, with resistance to not only vertical ion bombardment on the top but also spontaneous chemical etching on the sidewall of the rods. As described later, the Pt particles probably decomposed into nanoparticles and were deposited on the sidewalls of the organic rods during plasma etching. After the plasma etching, the organic rods were separately removed

from the substrate using a scriber. This collected sample was dispersed on other substrate, and TEM sample preparation was then performed. This method allows cross-sectional observations of the rods. Figure 3.5 (b) shows a TEM image of the rods collected from the sample, indicating that they are identical to those shown in Figure 3.5 (c). Interestingly, the organic rods had a mean diameter of 10.2 nm and were armored with Pt nanoparticles.

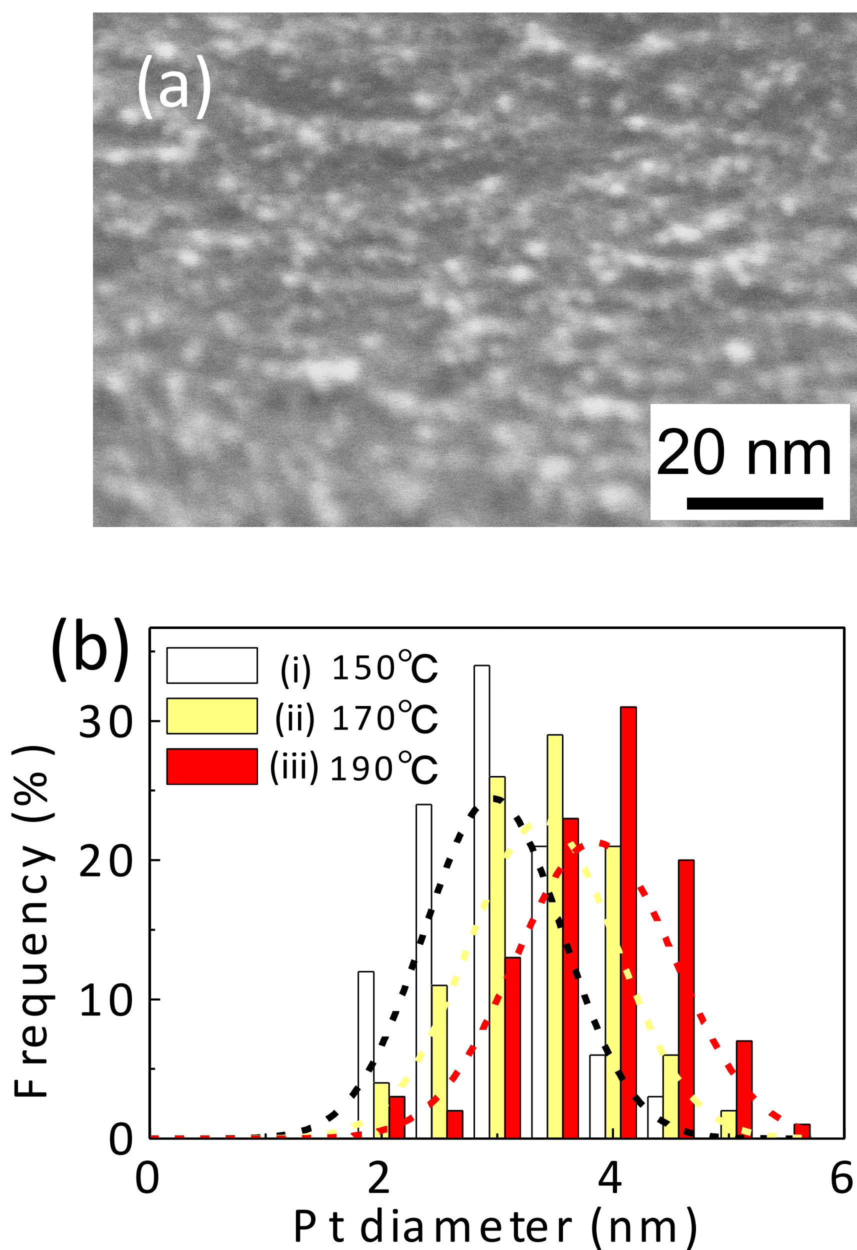

Figure 3.3 (a) SEM images of organic films before etching, Pt particles were deposited by MOCFD at 150°C. (b) The size distribution of diameter of Pt particles on the samples for the deposition temperature at (i) 150°C, (ii) 170°C and (iii) 190°C.

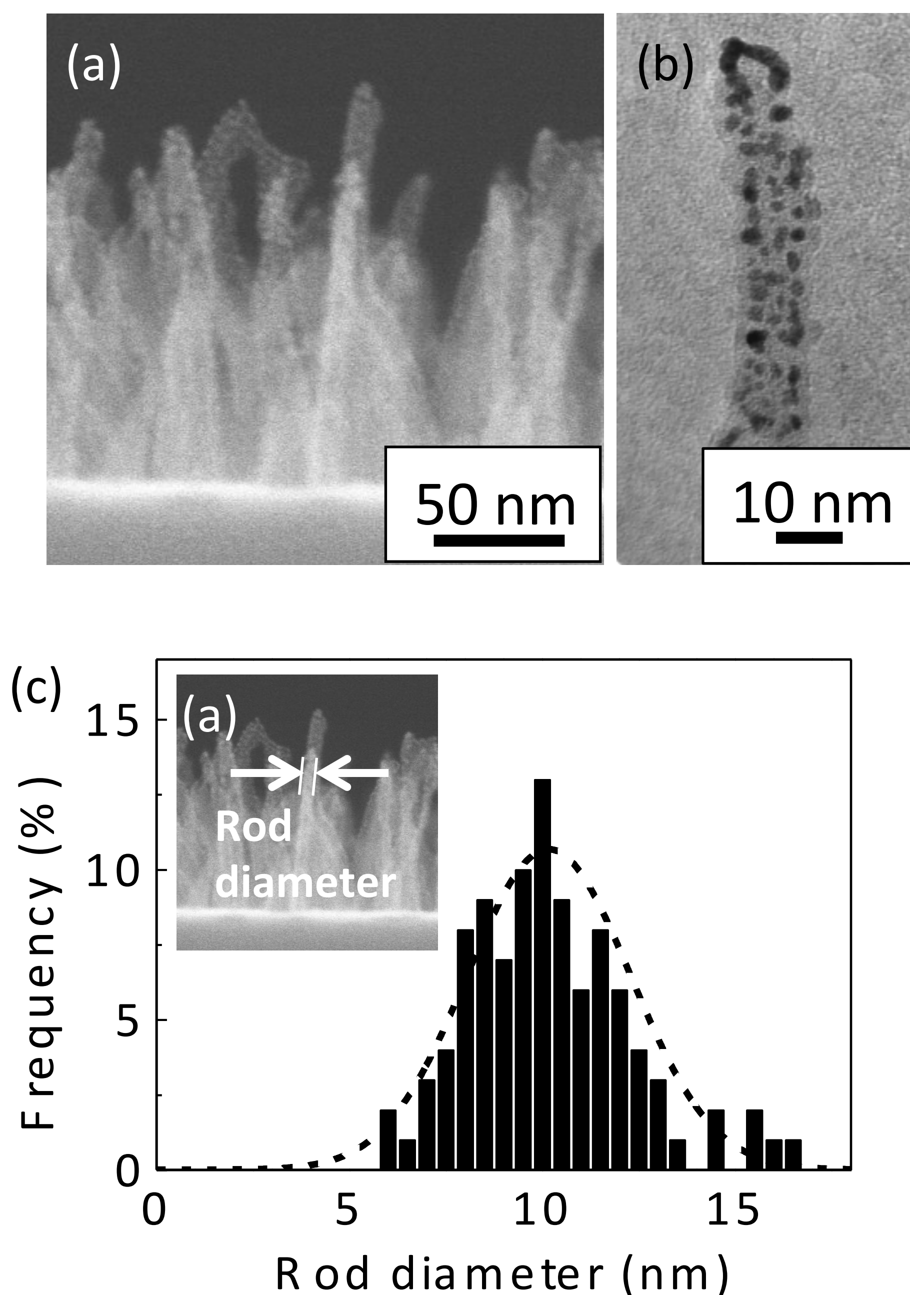

Figure 3.4 (a) Cross-sectional SEM images of organic films after the etching for 120 s after Pt particles deposition by the MOCFD with substrate temperature of 190°C. (b) Typical TEM image of the organic rods armored by Pt nanoparticles collected from the sample as identical as shown in (a). (c) The size distribution of width of organic rods on the sample as shown in (a).

3.3.2 Pt Nanoparticles Diameter Dependence on the Deposition Condition

Figure 3.5 (a)-(e) shows cross-sectional scanning electron microscope (SEM) images of organic films with Pt particles by MOCFD with different substrate temperatures of (a) 150°C, (b) 170°C (c) 190°C, (d) 210°C and (e) 230°C. Plasma etching conditions were a mixture ratio of 25 for N_2 and 75 for H_2, and the substrate temperature at 60°C for 30 s. As the substrate temperature was increased, the mean diameters of the Pt particles shifted to a higher value, from 2.97 to 12.85 nm. This indicated that the substrate temperature of MOCFD affects the diameter of the organic rods.

Figure 3.6 (a)-(c) shows cross-sectional SEM images of organic films etched after Pt particles deposition by MOCFD with different depositing times of (a) 10 min, (b) 20 min and (c) 30 min. Those size distribution of Pt particles is also shown in Figure 3.6 (d). As the deposition time was increased, the mean diameters of the Pt particles shifted slightly to a higher value, from 2.97 to 3.85 nm. This indicated that the substrate temperature of MOCFD affects the diameter of the organic rods. Figure 3.7 shows cross-sectional SEM images of organic films after etched subsequently deposited Pt particles by MOCFD with different Pt nanoparticle amount of (a) 2.5 ml and (b) 5 ml. Plasma etching conditions were a mixture ratio of 25 for N_2 and 75 for H_2, and the substrate temperature at 60°C for 30 s. Figure 3.7 (c) The size distribution of diameter of Pt particles on the samples as shown in (a) and (b). There were no increase of Pt diameter as increasing deposition time or Pt nanoparticle density. These results indicated that the substrate temperature of MOCFD affects the diameter of the nanoparticles.

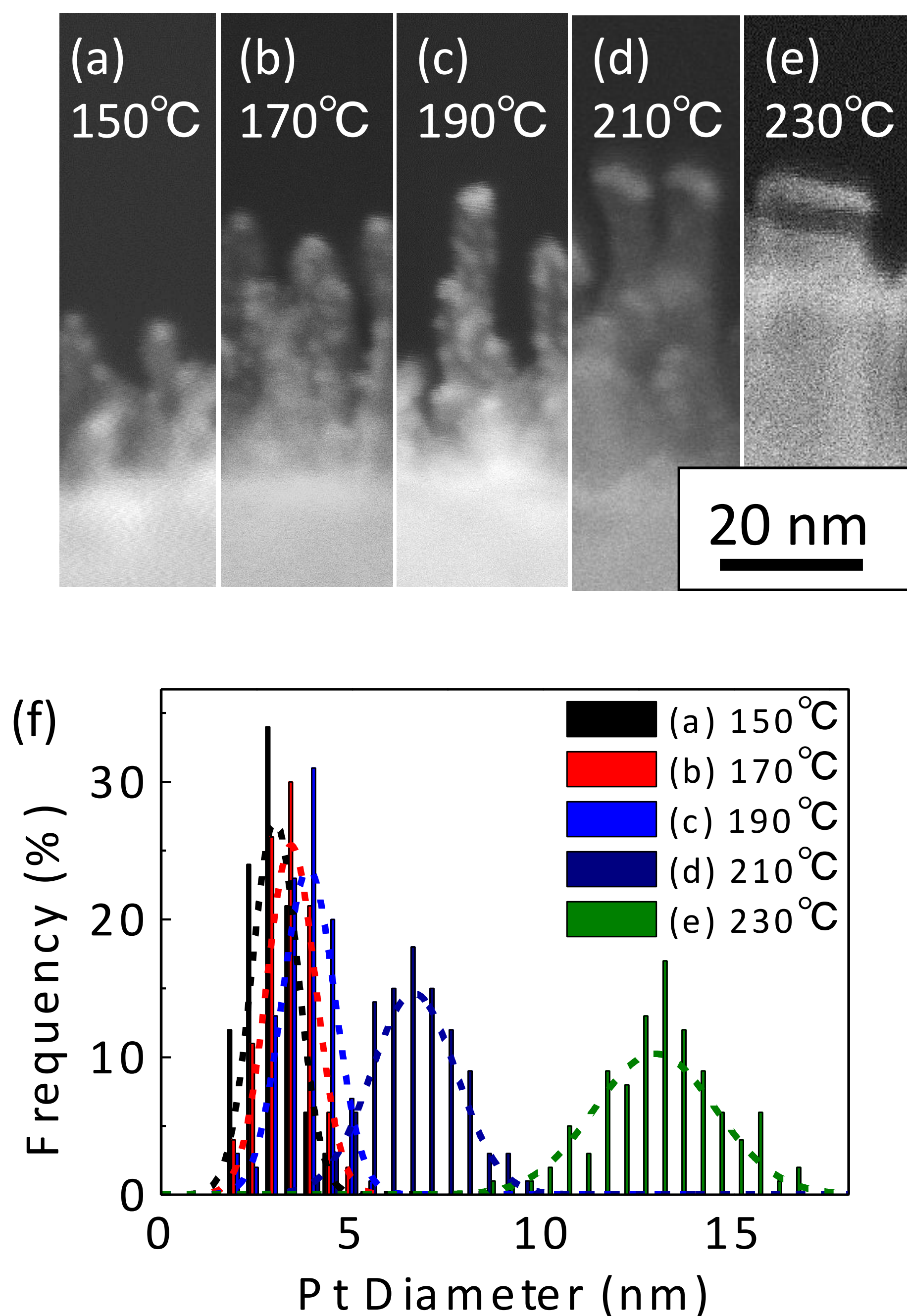

Figure 3.5 Cross-sectional SEM images of organic films after Pt particles deposition by MOCFD with different substrate temperatures of **(a)** 150°C, **(b)** 170°C **(c)** 190°C, **(d)** 210°C and **(e)** 230°C. Plasma etching conditions were a mixture ratio of 25 for N_2 and 75 for H_2, and the substrate temperature at 60°C for 30 s. **(f)** The size distribution of diameter of Pt particles on the samples as shown in **(a)**, **(b)**, **(c)**, **(d)** and **(e)**.

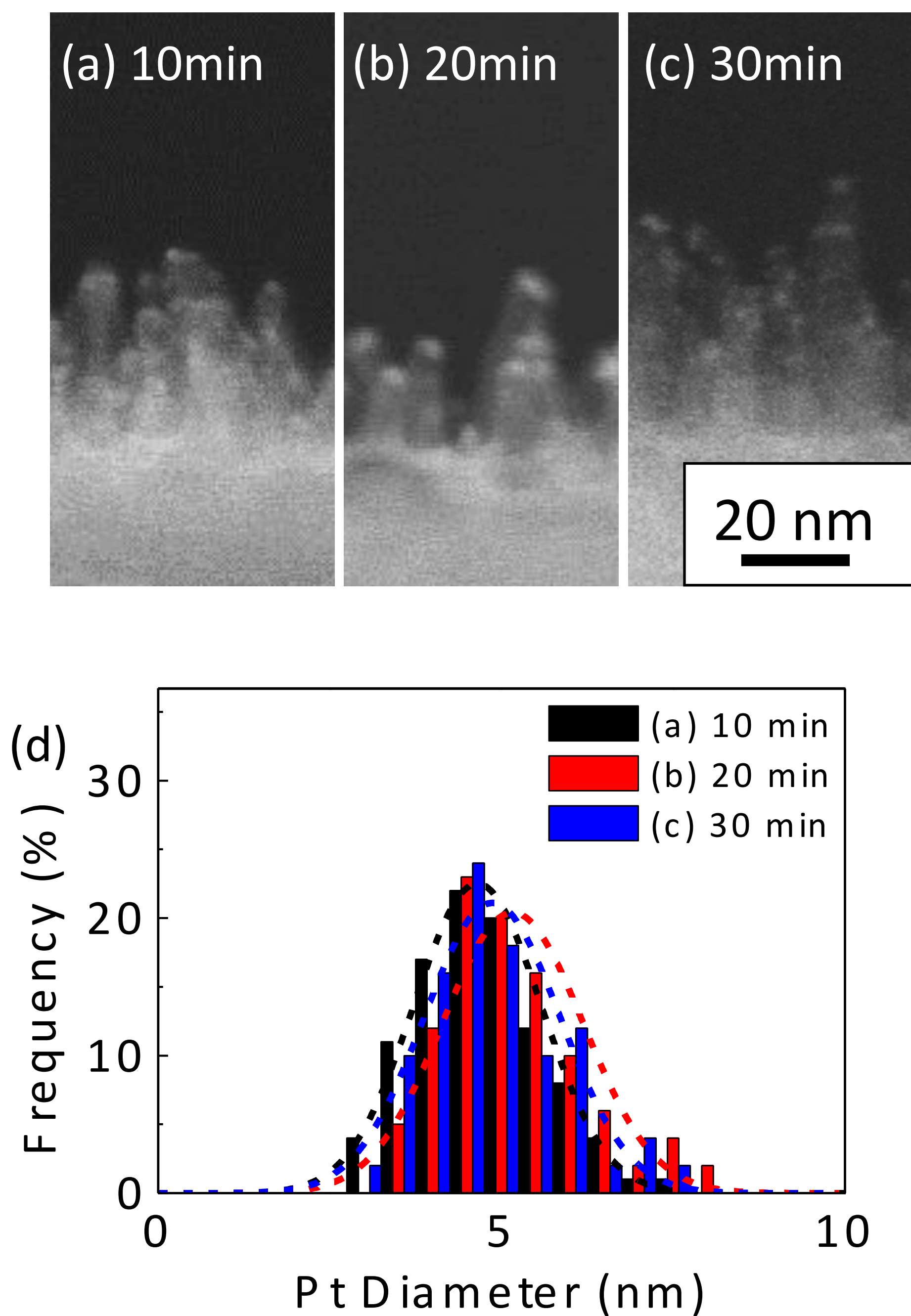

Figure 3.6 Cross-sectional SEM images of organic films after Pt particles deposition by MOCFD with different depositing times of **(a)** 10 min, **(b)** 20 min and **(c)** 30 min. Plasma etching conditions were a mixture ratio of 25 for N_2 and 75 for H_2, and the substrate temperature at 60°C for 30 s. **(f)** The size distribution of diameter of Pt particles on the samples as shown in **(a)**, **(b)** and **(c)**.

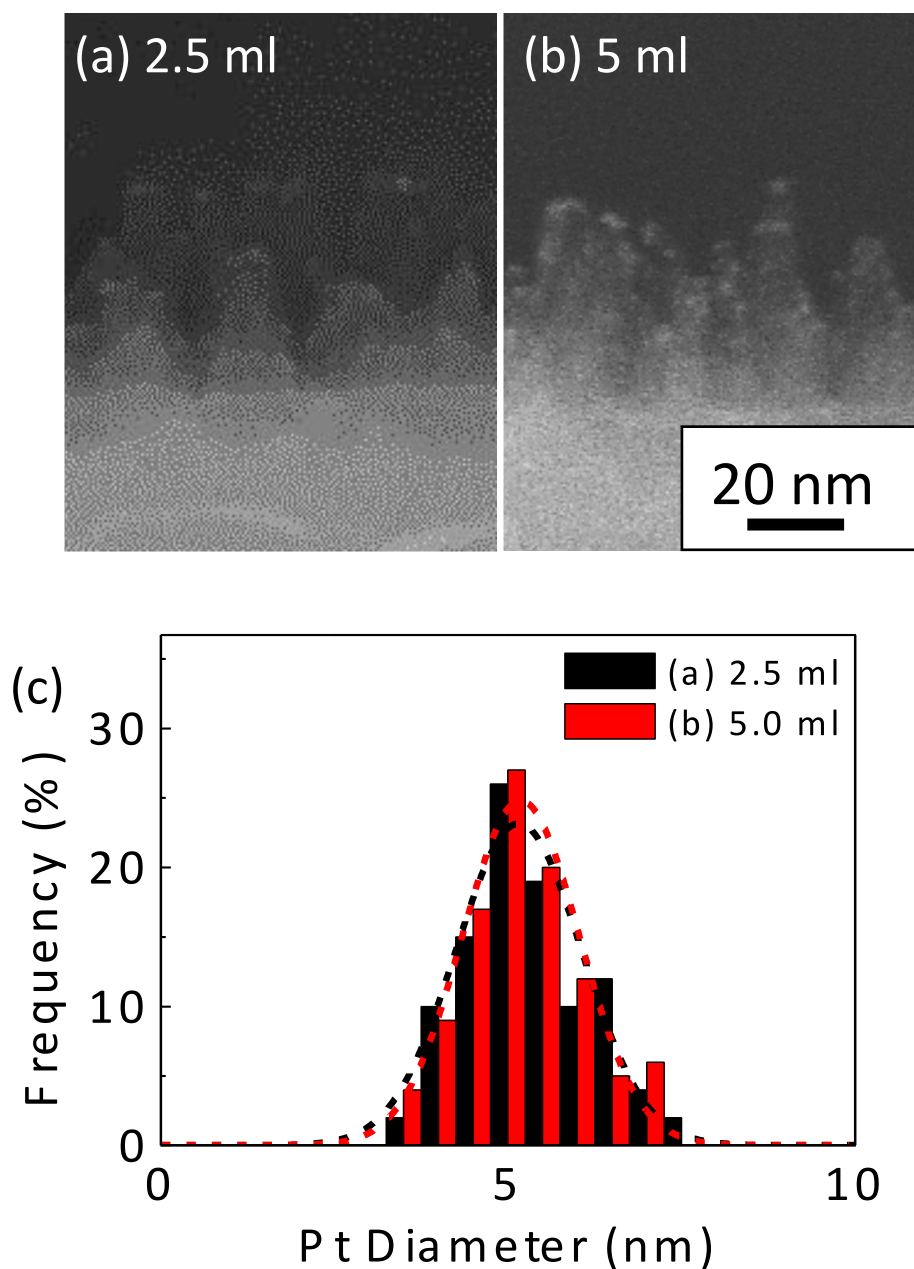

Figure 3.7 Cross-sectional SEM images of organic films after Pt particles deposition by MOCFD with different Pt complex amount of **(a)** 2.5 ml and **(b)** 5 ml. Plasma etching conditions were a mixture ratio of 25 for N_2 and 75 for H_2, and the substrate temperature at 60°C for 30 s. **(c)** The size distribution of diameter of Pt particles on the samples as shown in **(a)** and **(b).**

3.3.3 Dependence of Plasma Etching Conditions on Feature-Shapes

To assess etching shape, a dependence on substrate temperature and mixture gas flow ratio was investigated. Figure 3.5 (a)-(c) shows cross-sectional scanning electron microscope (SEM) images of organic films after being partially etched for 30 s with different N_2 mixture gas flow ratio of (a) 75%, (b) 50% and (c) 25%. And the films with with different substrate temperatures of (d) 0°C, (e) 30°C and (f) 60°C with N_2 mixture gas flow ratio of 75% after subsequently deposited with Pt particles by MOCFD. As the substrate temperature or the H_2 gas ratio increased, feature shapes exhibit tapered shapes. These tapering are parameterized by taking a ratio of top and bottom parts of rods. Mean taper amounts of the organic rods decreased drastically from 10.51 nm for (a) 75% to 2.44 nm for (c) 25 %, and 9.94 nm for (d) 0°C to 2.44 nm for (f) 60°C after partially etched for 30 s. And they also decreased drastically from 3.96 nm for (i) 75% to 0.18 nm for (k) 25 %, and 4.96 nm for (l) 0°C to 0.18 nm for (n) 60°C after completely etched for 120s. Namely, the feature profile became the most vertical – like rod having same thickness from the top to the bottom – while the etching conditions were of 75% mixture of N_2 gas at the substrate temperature of 60°C.

Notably, the etching conditions were different from the tendency obtained for the blanket organic films. If the blanket film without covering Pt particles is etched, the feature shapes became the bowing shape – like stick having thinning at middle level. This indicated that the blanket organic films were etched spontaneously. On contrary, in cases with Pr nanoparticles, it is noteworthy that the taper shapes were always exhibited, since the spontaneous etching prevented.

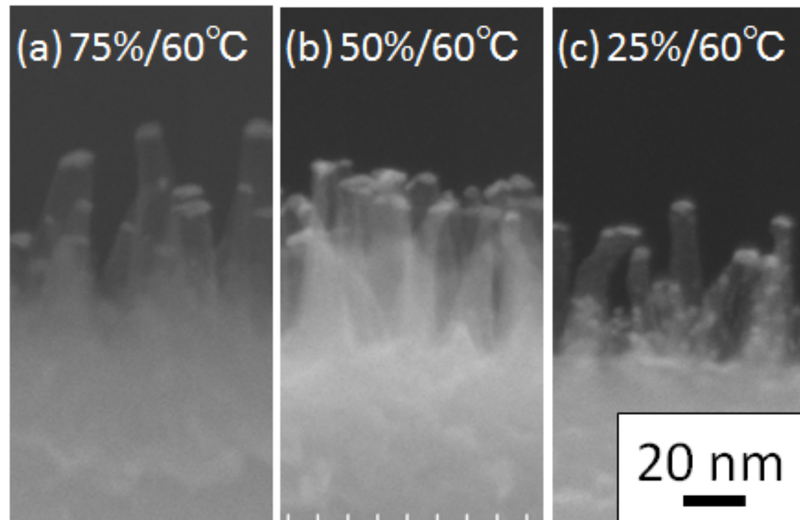
(a) 75%/60°C
(b) 50%/60°C
(c) 25%/60°C
20 nm

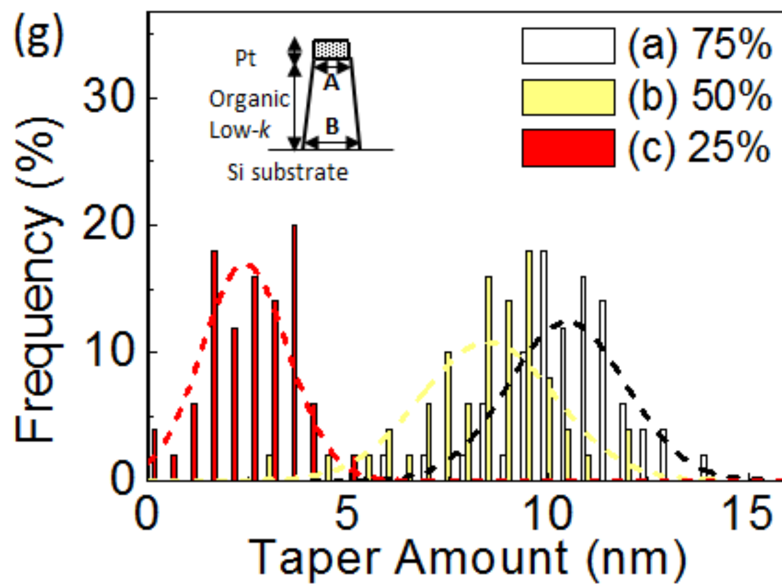
(g)
Pt
Organic
Low-k
A
B
Si substrate
(a) 75%
(b) 50%
(c) 25%
Frequency (%)
Taper Amount (nm)
0
10
20
30
0
5
10
15

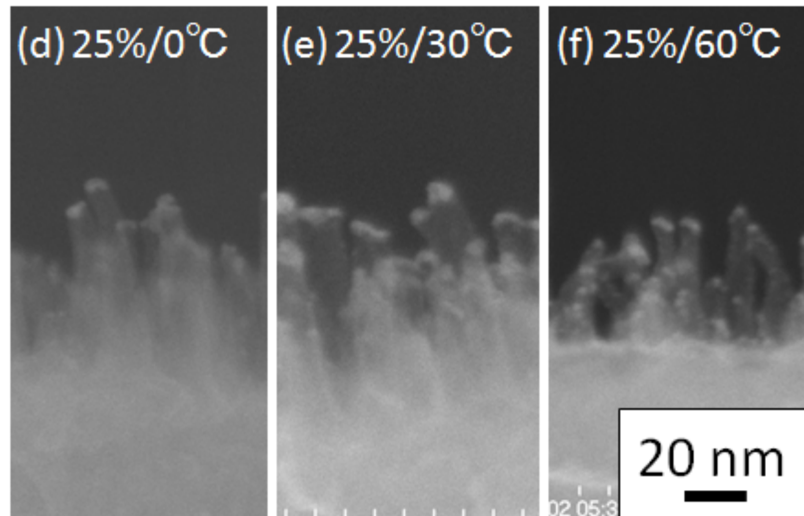

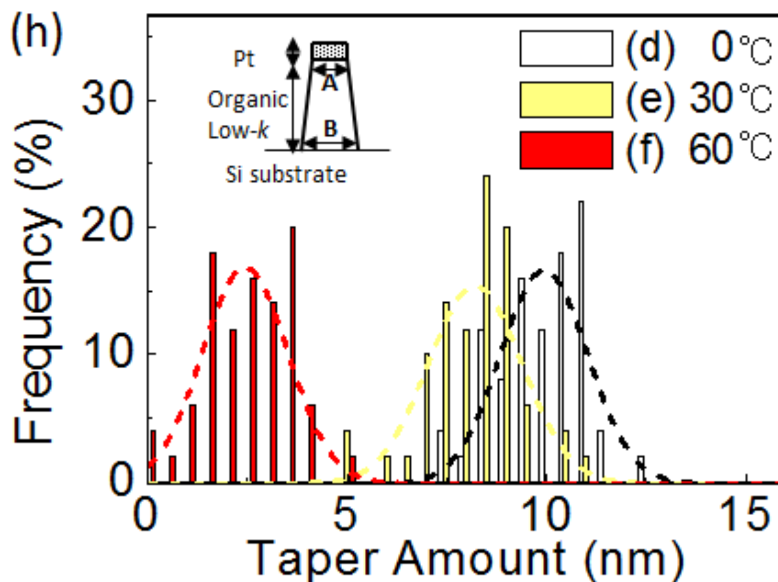

Figure 3.8 Cross-sectional SEM images of organic films after etching, subsequent to Pt particle deposition by MOCFD, at different N_2 mixture gas flow ratio of (a) 75% (b) 50% and (c) 25% with the substrate temperature of 60°C after partially etched for 30 s. Additionally, images shows dependence of the substrate temperatures at (d) 0°C, (e) 30°C and (f) 60°C with mixture ratios of 25 for N_2 and 75 for H_2 after partially etched for 30 s. And lower part of images in (l), (m) & (n) shows after completely etched for 120s. The organic rods tended to taper-shape with increasing (g) the mixture ratio of N_2 gas or (h) the substrate temperature after partially etched for 30 s.

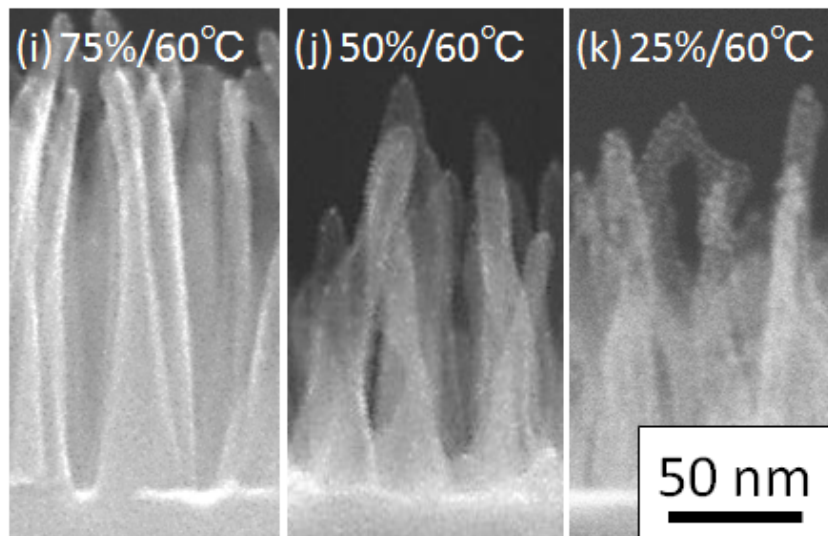

(i) 75%/60°C
(j) 50%/60°C
(k) 25%/60°C
50 nm

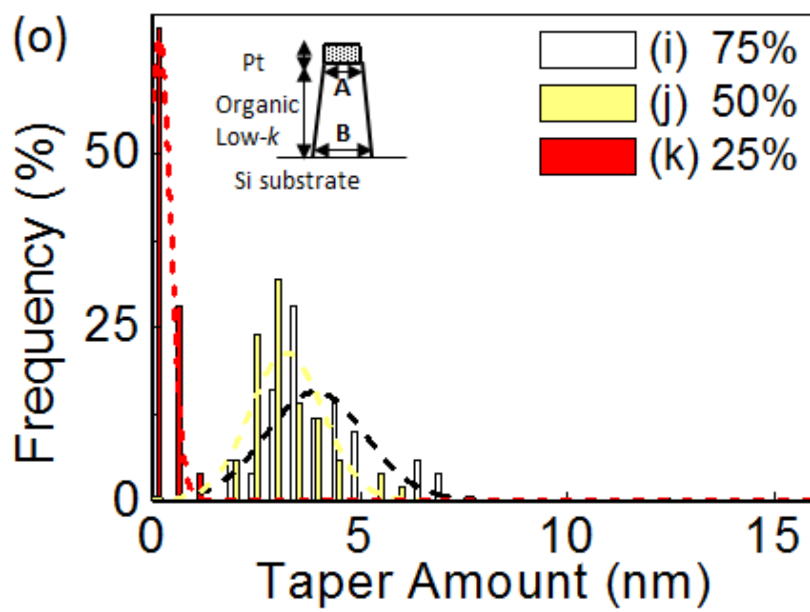

(o)
Pt
Organic
Low-k
A
B
Si substrate
(i) 75%
(j) 50%
(k) 25%
Frequency (%)
0
25
50
0
5
10
15
Taper Amount (nm)

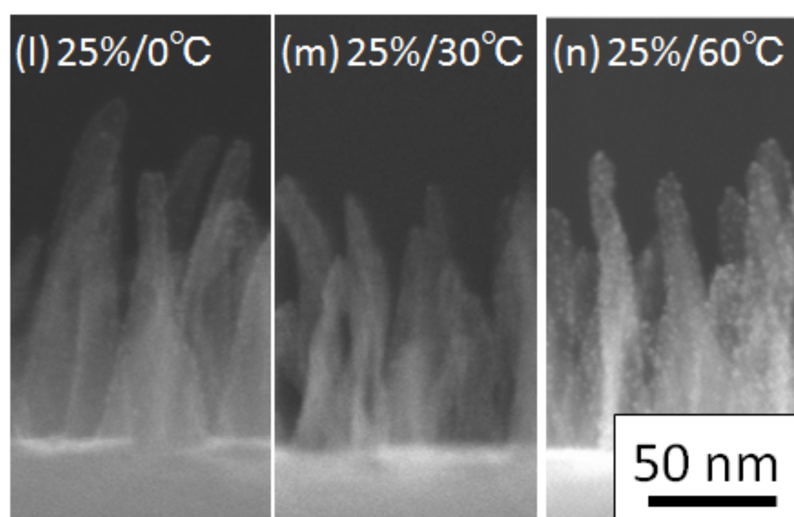

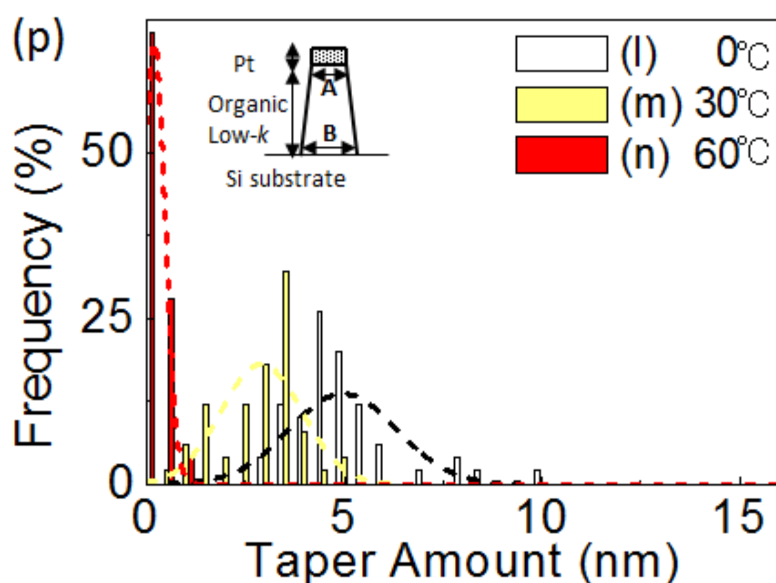

Figure 3.8 Cross-sectional SEM images of organic films after etching, subsequent to Pt particle deposition by MOCFD, at different N_2 mixture gas flow ratio of (i) 75% (j) 50% and (k) 25% with the substrate temperature of 60°C after completely etched for 120s. Additionally, images shows dependence of the substrate temperatures at (d) 0°C, (e) 30°C and (f) 60°C with mixture ratios of 25 for N_2 and 75 for H_2 after partially etched for 30 s. The organic rods tended to taper-shape with increasing (o) the mixture ratio of N_2 gas or (p) the substrate temperature after completely etched for 120s. The shape parameter is defined a ratio of diameters at top and bottom parts of the rods.

3.3.4 Temporal Variations of Feature Shapes in Plasma Etching

Figure 3.9 shows cross-sectional SEM images of organic films after etching, subsequent to Pt particle deposition by MOCFD as a function of the etching time for (a) 30 s to 180 s at 60°C. The time- dependent height of the organic rods and etched organic film are shown in (f) as the with Pt cover and without Pt cover.

The organic rods formation is confirmed. Pt nanoparticle covered organic rods also etched with the plasma exposure. However, the etching amount was almost half compared to the etching amount at uncovered area. Lateral etching of the organic rod was not observed. This tendency and value back up the result of Fig. 3.4.

Figure 3.10 shows the increase of the intensity of Pt 4f spectrum during etching process and the decrease during over etching. This result indicates that the increase of the Pt nanoparticle density during plasma etching process and decrease during over etching process. This result also back up the decomposition of the small sputtered Pt particle into nanoparticles on the sidewalls of the organic rods during plasma etching.

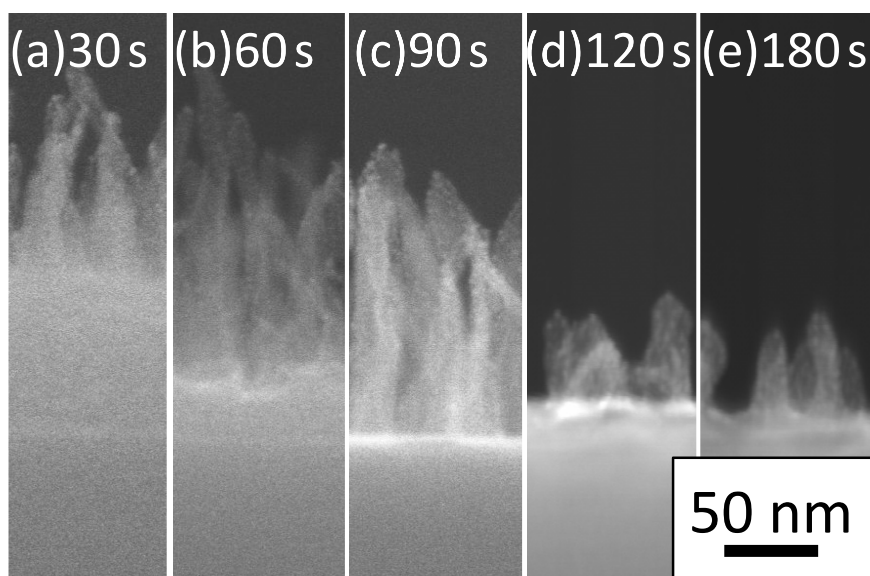

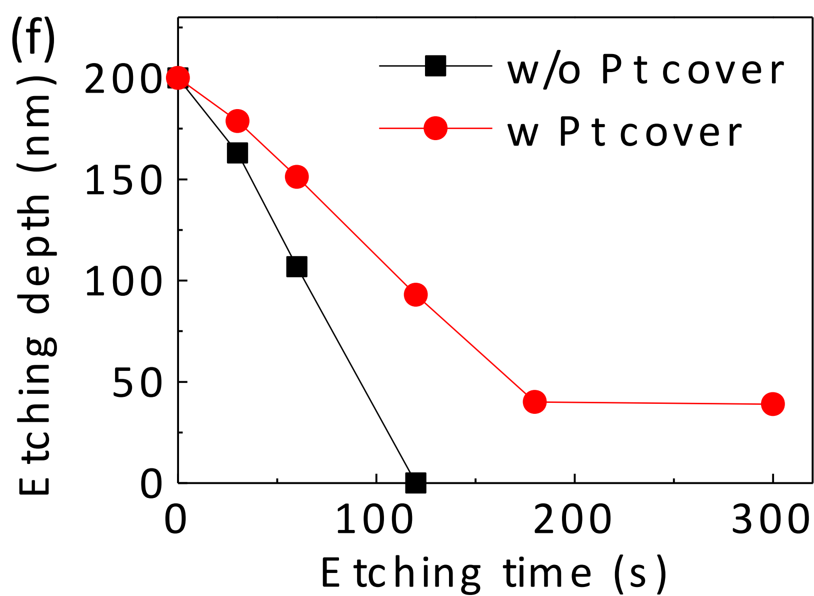

Figure 3.9 Cross-sectional SEM images of organic films after etching, subsequent to Pt particle deposition by MOCFD, as increasing etching time of (a) 30 s (b) 60 s and (c) 120 s (d) 180 s and (e) 300 s with the substrate temperature of 60°C.

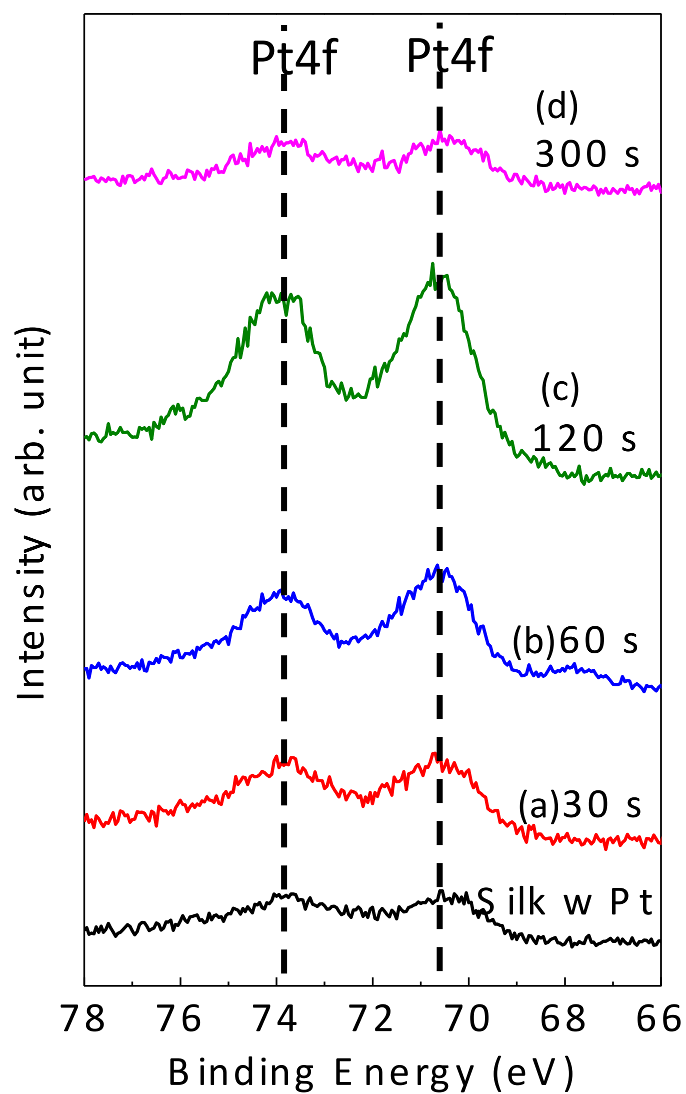

Figure 3.10 XPS Pt 4f spectrums for the surface of organic film as increasing etching time of (a) 30 s (b) 60 s and (c) 120 s (d) 180 s and (e) 300 s with the substrate temperature of 60°C.

3.3.5 Comparison of Methods for Pt Particle Mask deposition

I made comparison the methods of Pt particle mask deposition between the supercritical chemical fluid deposition (SCFD) and the arc-plasma sputter gun. The SCFD method has been described above the section 3.2.1. The arc-plasma sputter gun was operated with Ar gas flow rate of 100 sccm and power of 200 W.

Figure 3.11 shows the cross-sectional SEM images of organic films with Pt mask deposited by SCFD after being etched for (a) 30 s and completely etched for (b) 120 s, and organic films with Pt mask deposited arc plasma sputter gun after being etched for (c) 30 s and completely etched for (d) 120 s.

Both etching features with Pt mask deposition by SCFD and arc plasma gun were almost the same after being etched for 30 s. However, organic rods after 120 s etching could be only seen at the condition of Pt mask deposition and couldn’t be seen at the condition of Pt deposition. The difference between the Pt particle deposited by SCFD and arc plasma gun is assumed to be the size of the sputtered particle since Pt particle deposit by SCFD is constructed by Pt complex and bonding of the each complex is weak compared to the Pt particle deposited by the ark plasma gun. And the small sputtered Pt particle decomposed into nanoparticles and deposited on the sidewalls of the organic rods during plasma etching, and could play a role in the masking, with resistance to not only vertical ion bombardment but also chemically spontaneous etching. Thus the organic rod fabricated only under the Pt mask deposited by SCFD.

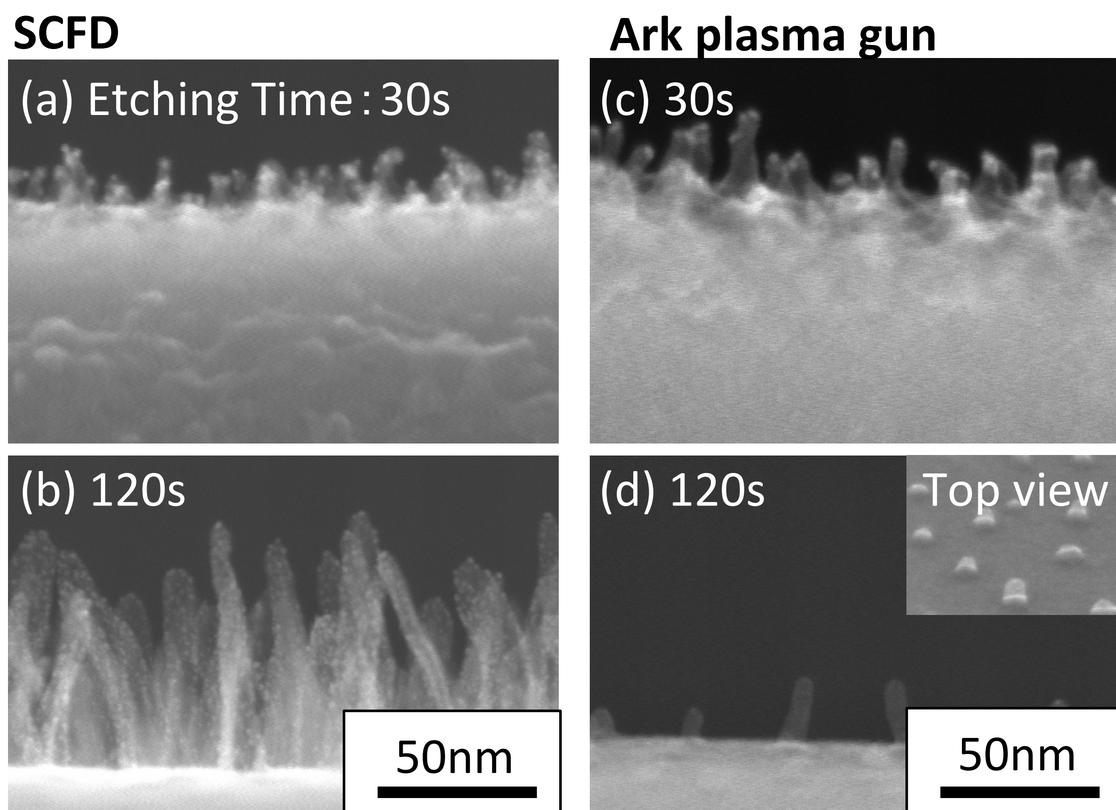

Figure 3.11 Cross-sectional SEM images of organic films with Pt mask deposited MOCFD after being etched for (a) 30 s and (b) completely etched for 120 s.

3.3.6 Sidewalls Protection Effect of Pt Nanoparticle against Etching of H Atoms

To confirm the effect of Pt nanoparticles on sidewall, 65-nm line and space (L&S) mask patterned organic film was etched with and without Pt particle deposition by MOCFD. Figure 3.12 shows Cross-sectional SEM images of the L&S patterned organic films after the etching of 90 s (a) and, L&S patterned Pt particle deposited organic film after the 120 s etching (b).

As seen in Figs, the lateral etching amount decreased from 9.2 nm to 4.1 nm. And the undercut decreased from 7.2 nm to almost 0 nm. It is well known that lateral etching is conducted during the etching because the sidewall is exposed to atom and angled ion bounced from the mask. On the other hand the film just under the mask is exposed to only atom. So this result indicate that with the Pt particle deposition, sidewall is protected from ion assist atom etching and etching amount decreased half. It also protect the sidewall just under the mask from the atom etching and etching amount decreased to almost zero. The result is reasonable to the result of Figure 3.4.

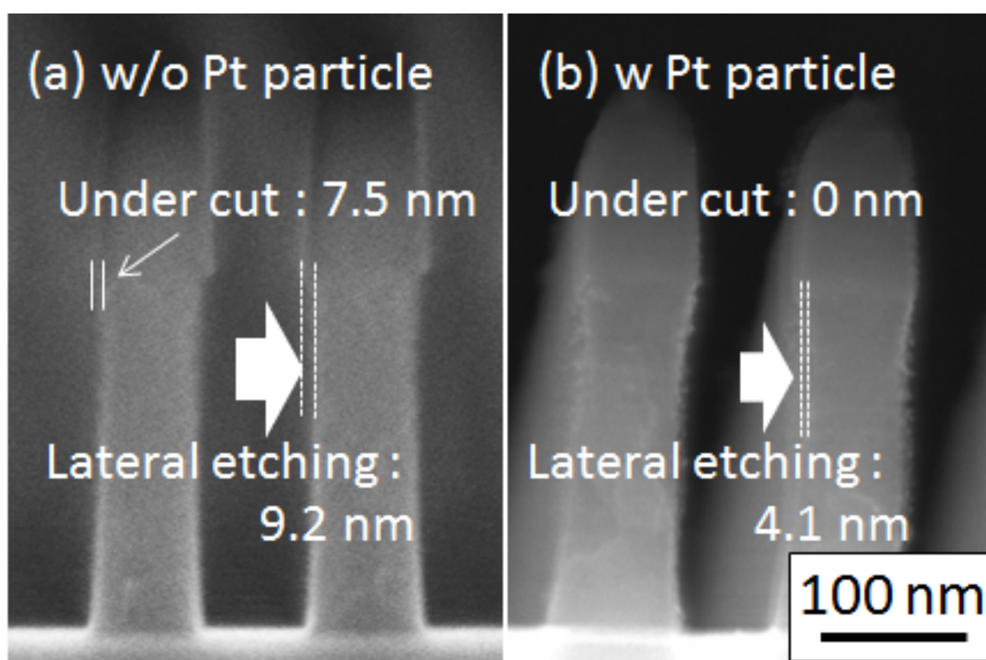

Figure 3.12 Cross-sectional SEM images L&S patterned organic films after being completely etched for 90 s (a) and, L&S patterned Pt particle deposited organic film (b).

3.3.7 Analysis of Protection Effect of Pt Nanoparticle

To examine why the sidewalls of the organic rods were prevented from erosion, I conducted the following experiment in order to clarify the protective ability of Pt nanoparticles existing at the sidewalls during etching. Our hypothesis, based on experimental results of the organic rod formation, is schematically illustrated in Figure 3.15. Atoms and ions in the H_2/N_2 plasma reacted with the organic materials and played two different roles: ion-assisted etching of organic material and ion sputtering of the Pt mask. The following are envisaged: (a) Pt particles were deposited on the organic films; (b) the Pt particles were deposited with clustering on the sidewalls during the etching process; (c) the sidewall of organic rods were covered and protected from etching by H atoms.

Figure 3.16 (a) shows a comparison of the etching characteristics of samples with and without Pt particle deposition on the organics films. At the sidewalls, the effect of ion bombardment is almost negligible since the ions impinge laterally. Neutral atom species and plasma emission light are irradiated directly from the plasma. In order to clarify the etching process at the sidewall, our group has developed a technique called Pallets for Plasma Evaluation (PAPE) [26-29]. As the Pt particles covered the organics, the etching amount for the rest of Pt deposited area in direct exposure to the plasma decreased to almost half compared with the case without Pt nanoparticle deposition. Figure 3.16 (b) shows a comparison of etching characteristics of the samples regarded as sidewalls with and without Pt particles on organics. Transport of atoms inside the gap between sample surface and MgF_2 window was estimated to 1-2% of the actual fluxes of open area. Thus I carried out a treatment for hundred larger duration time for comparison. The etching amounts drastically decreased to less than 10% with the Pt nanoparticles. Namely, the Pt nanoparticles prevented lateral etching within a thickness of less than 1 nm. The Pt nanoparticles thus had a protective effect from etching on the

sidewalls, especially for etching by atoms but not ions.

Here, I used plasma chemistry comprising H and N gases. In our previous studies, the organic films were chemically etched by exposure to H atoms [30]. N atom has a role for creation of a protective layer comprising from C-N bonds, which could inhibit to spontaneously etch of H atom [30,33,34]. Basically, the C-N layer acts in part as sidewall protection but not perfectly. The H atoms recombine on the Pt surface with a large recombination coefficient. As the results, the number of reactive H atoms decreases and it decrease chemical etching of the organic films by exposure to H atoms [31]. I proved that the etching amounts caused by H atoms were drastically decreased to less than one tenth in the cases of the surface with Pt nanoparticles. The Pt nanoparticles have a protective effect against chemical etching by H atoms and this minimizes sidewall etching. Organic nanorods were thus realized with Pt nanoparticles acting as sidewall protection film. As a result, outstanding high aspect ratio etching was successfully obtained. This is a novel and useful method employing supercritical chemical fluid deposition of nanoparticles and plasma etching. The method enables fabrication of 10-nm-scale organic rods with the protective effect of Pt nanoparticles under a specific organic-film-etching condition.

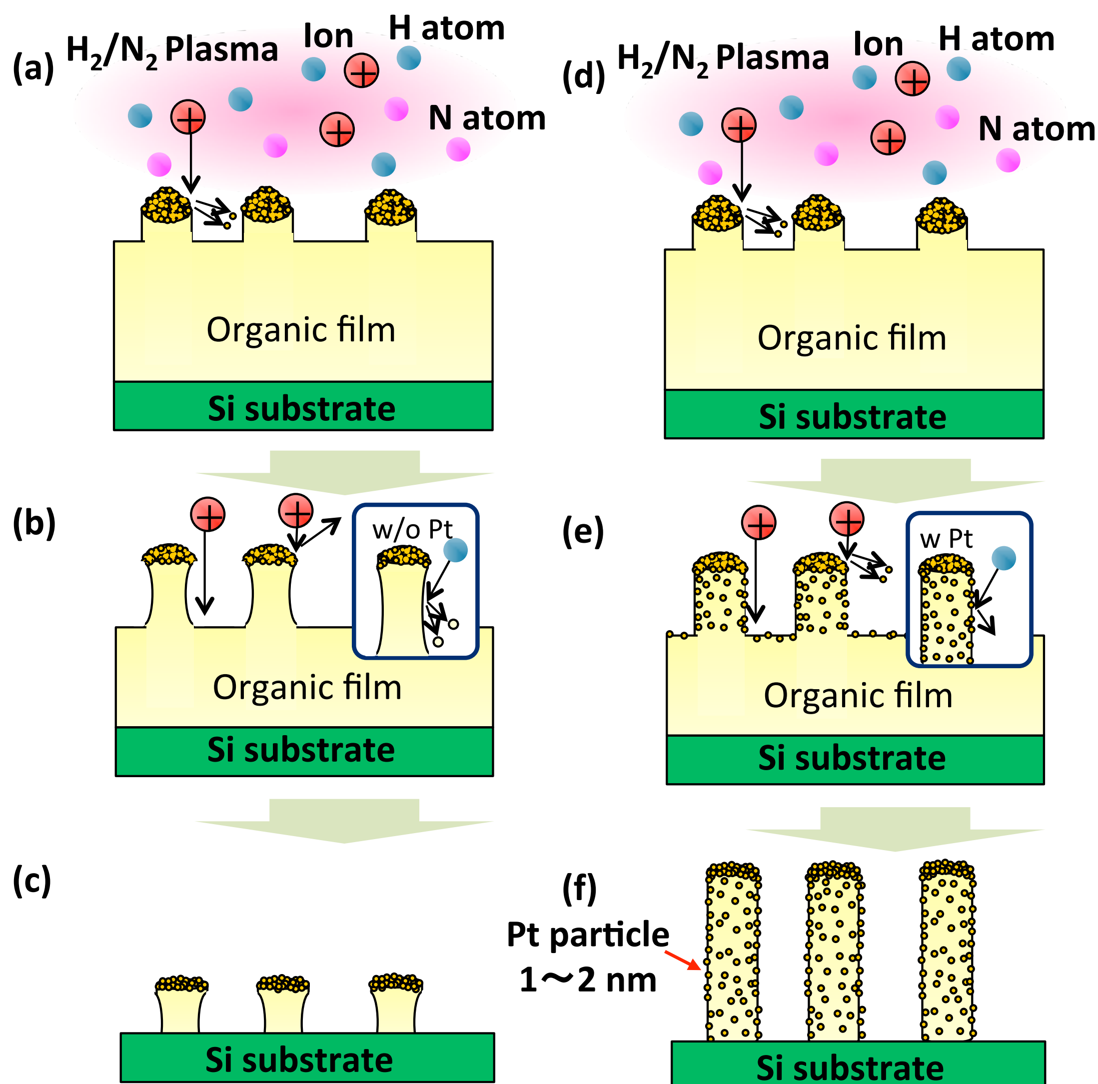

Figure 3.15 Schematic illustration of formation of organic rods armored by Pt nanoparticles. **(a)** The deposited Pt nanoparticles cluster were suputtered by ion sputtering effects. **(b)** During etching process, the the sidewall of rods were eroded by chemical reaction with atom. **(c)** The armored organic rods were etched to be short and thin. **(d)** The deposited Pt nanoparticles cluster decomposed into nanoparticles by ion sputtering effects. **(e)** During etching process, the decomposed particles covered on the sidewall of rods. **(f)** The armored organic rods protected at the sidewall from etch of H atom.

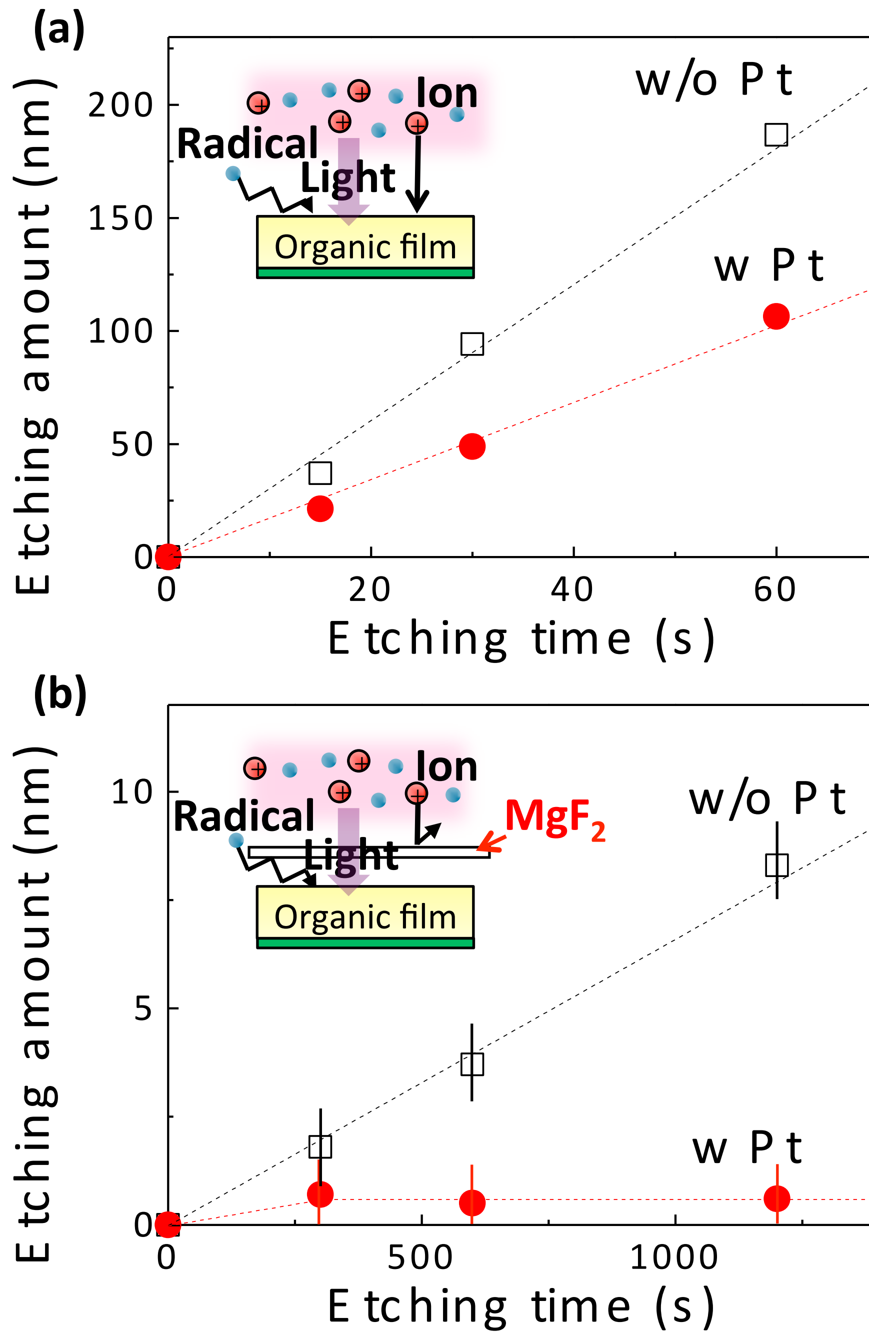

Figure 3.16 Etching amounts in plasma treatment of the blanket organic films with or without deposition of Pt particles. **(a)** by direct plasma exposure and **(b)** by irradiating limited only neutrals and lights, covering with a MgF_2 window with spacing roofed the sample. Etching conditions were identical with the aforementioned samples.

3.3.8 Application in Field Emission Device

The organic rod electrical characteristics were also changed from insulator to conductor. Figure 3.17 shows field emission properties of the armored organic rods. Electron field emission properties of the rods were clearly obtained. The electric field threshold was decreased from 13.1 to 8.2 V/μm as the N and H atom density ratio in the plasma etching was changed. According to the Fowler-Nordheim (FN) theory [32], the electrical current, I, at the applied voltage, V, is given by [32] ($\mathrm{I} = V^2 \exp\left(\frac{-b}{V}\right)$), where $\mathrm{b} = \frac{-6.38\times10^9\phi^{\frac{1}{2}}}{\beta}$, the slope of the linear part of the FN plot of $\ln\frac{\mathrm{I}}{V^2} = \frac{-b}{V}$, ß is the field enhancement factor, and φ is the work function.

It was estimated that the shapes of the top part of the rods were possibly unchanged among each etching condition. If the surface reacted with N atoms, then it was modified by the formation of a layer of sp_3 -bonded C-N to protect from spontaneous chemical etching [30,33,34]. During plasma etching, surface nitridation on carbon materials worked to protect more effectively the lateral etching of the sidewalls. Consequently, lower the work function was obtained on the samples of Pt/C composites.

Namely, the compositional ratio of H_2 and N_2 had a strong impact on the electro-conductive properties of the organic rods armored with Pt nanoparticles. It has been reported recently that self-assembled graphitic carbon materials such as carbon nanotubes (CNT), carbon nanowalls (CNW). have lower threshold of a few V/μm in electric field than the experimental result of 8.2 V/μm.[19] As consequence the emission properties of organic rods synthesized were inferior to that of other conductive materials.

However, there is a strong emphasis on electron emission of the organic rods, as originally insulator. In general no emission is found from insulator or under high

fields at least as high as 100 V/μm. I believe the modified sp_3-bonded C-N layer responsible for enhancing electro-conductivity and field emissions. The novel approach utilizing the organic/inorganic composites described here may fill a gap opening top-down and bottom-up synthesis at nanometer and atomic scales. I anticipate this to be a solution for fabricating flexible electronics on polymeric materials. In future, the composite materials may open novel applications for displays and provide on cloths with the ability for solar-cell-driven sterilization.

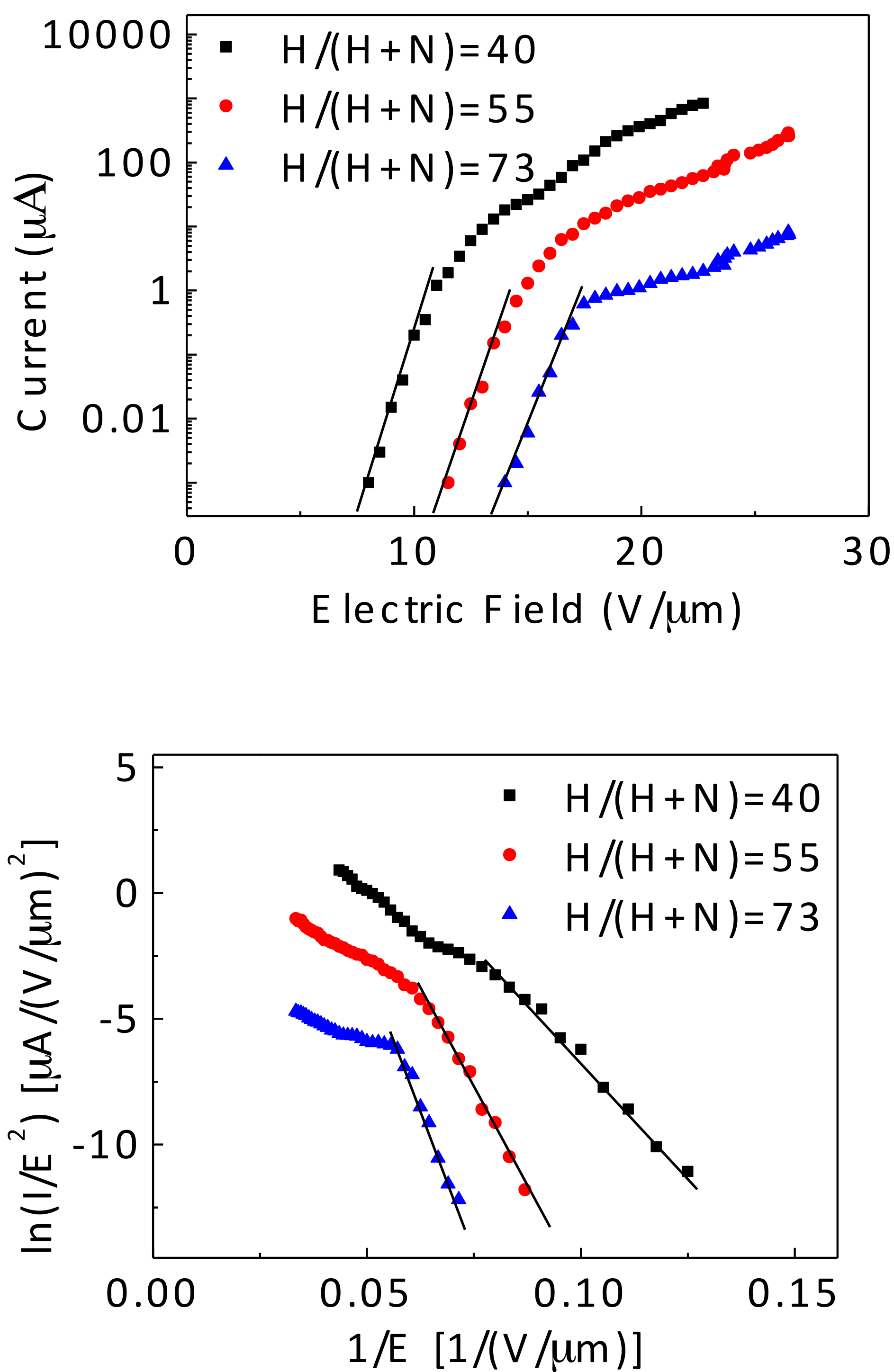

Figure 3.17 (a) The current-voltage plot of the electron field emission properties for the organic rods (b) Fowler-Nordheim plot of (a).

3.4 Conclusion

In conclusion, I have demonstrated the fabrication of 10-nm-scale organic rods covered on the sidewalls with Pt nanoparticles that acted as a resist mask. Supercritical chemical fluid-deposited Pt particles were deposited on the sidewall to inhibit the spontaneous chemical etching reactions of H atoms with organics. The Pt nanoparticles prevented lateral etching within a thickness of less than 1 nm. Accordingly, precise shape control was achieved by this approach of the sidewall protective effect with the Pt nanoparticle coverage. These armored organic rods changed from dielectric to conductive demonstrating field emission properties. It is noteworthy that the super-fine plasma etching of organic materials is a suitable fabrication process at low temperatures for flexible materials.

3.5 References

[1] M. J. Pitkethly: Nano Today 36 (2003) 36.

[2] K. Ostrikov: Rev. Mod. Phys. 77 (2005) 489.

[3] B. D. Gates, Q. Xu, M. Stewart, D. Ryan, C. G. Willson, and G. M. Whitesides: Chem. Rev. 105 (2005) 1171.

[4] M. Kaltenbrunner, M. S. White, E. D. Głowacki, T. Sekitani, T. Someya, N. S. Sariciftci, and S. Bauer: Nat. Commun. 3 (2012) 770.

[5] S. Iijima: Nature 354 (1991) 56.

[6] W. Lu and C. M. Lieber: Nat. Mater. 6 (2007) 841.

[7] A. G. Rinzler, J. H. Hafner, P. Nikolaev, P. Nordlander, D. Tomanek, R. E. Smalley, L. Lou, S. G. Kim, and D. T. Colbert: Science 269 (1995) 1550.

[8] W. A. de Heer, A. Chaˆtelain, and D. A. Ugarte: Science 270 (1995) 1179.

[9] Q. H. Wang, T. D. Corrigan, J. Y. Dai, R. P. H. Chang, and A. R. Krauss: Appl. Phys. Lett. 70 (1997) 3308.

[10] A. M. Rao, D. Jacques, R. C. Haddon, W. Zhu, C. Bower, and S. Jin: Appl. Phys. Lett. 76 (2000) 3813.

[11] H. Murakami, M. Hirakawa, C. Tanaka, and H. Yamakawa: Appl. Phys. Lett. 76 (2000) 1776.

[12] W. B. Choi, D. S. Chung, J. H. Kang, H. Y. Kim, Y. W. Jin, I. T. Han, Y. H. Lee, J. E. Jung, N. S. Lee, G. S. Park, and J. M. Kim: Appl. Phys. Lett. 75 (1999) 3129.

[13] A. Thess, R. Lee, P. Nikolaev, H. Dai, P. Petit, J. Robert, C. Xu, Y. H. Lee, S. G. Kim, A. G. Rinzler, D. T. Cocert, G. E. Scuseria, D. T. Tomanek, J. E. Fischer, and R. E. Smalley: Science 273 (1996) 483.

[14] Z.W.Pan,S.S.Xie,B.H.Chang,C.Y.Wang,L.Lu,W.Liu,W.Y. Zhou, W. Z. Li, and L. X. Qian: Nature 394 (1998) 631.

[15] Z. F. Ren, Z. P. Huang, J. W. Xu, J. H. Wang, P. Bush, M. P. Siegal, and P. N.

Provencio: Science 282 (1998) 1105.

[16] M. Tanemura, K. Iwata, K. Takahashi, Y. Fujimoto, F. Okuyama, H. Sugie, and V. Filip: J. Appl. Phys. 90 (2001) 1529.

[17] P. Rai, D. R. Mohapatra, K. S. Hazra, D. S. Misra, J. Ghatak, and P. V. Satyam: Chem. Phys. Lett. 455 (2008) 83.

[18] Y. Saito, K. Hamaguchi, S. Uemura, K. Uchida, Y. Tasaka, F. Ikazaki, M. Yumura, A. Kasuya, and Y. Nishina: Appl. Phys. A 67 (1998) 95.

[19] T. Machino, W. Takeuchi, H. Kano, M. Hiramatsu, and M. Hori: Appl. Phys. Express 2 (2009) 025001.

[20] K. Mase, H. Kondo, S. Kondo, M. Hori, M. Hiramatsu, and H. Kano: Appl. Phys. Lett. 98 (2011) 193108.

[21] T. Horibe, H. Kondo, K. Ishikawa, H. Kano, M. Sekine, M. Hiramatsu, and M. Hori: Appl. Phys. Express 6 (2013) 045103.

[22] S. J. Martin, J. P. Godschalx, M. E. Mills, E. O. Shaffer, II, and P. H. Townsend: Adv. Mater. 12 (2000) 1769.

[23] J. P. Godschalx, D. R. Romer, Y. H. So, Z. Lysenko, M. E. Mills, G. R. Buske, P. H. Townsend, III, D. W. Smith, Jr., S. J. Martin, and R. A. DeVries: US Patent 5965679 (1999).

[24] M. Kreyenschmidt, F. Uckert, and K. Muellen: Macromolecules 28 (1995) 4577.

[25] R. D. Goldblatt, B. Agarwala, M. B. Anand, E. P. Barth, G. A. Biery, Z. G. Chen, S. Cohen, J. B. Connolly, A. Cowley, T. Dalton, S. K. Das, C. R. Davis, A. Deutsch, C. DeWan, D. C. Edelstein, P. A. Emmi, C. G. Faltermeier, J. A. Fitzsimmons, J. Hedrick, J. E. Heidenreich, C.-K. Hu, J. P. Hummel, P. Jones, E. Kaltalioglu, B. E. Kastenmeier, M. Krishnan, W. F. Landers, E. Liniger, J. Liu, N. E. Lustig, S. Malhotra, D. K. Manger, V. McGahay, R. Mih, H. A. Nye, S. Purushothaman, H. A. Rathore, S.-C. Seo, T. M. Shaw, A. H. Simon, T. A. Spooner, M. Stetter, R. A. Wachnik, and J. G. Ryan: Proc. Int. Interconnect Technology Conf., 2000, p. 261.

[26] H. Yamamoto, K. Takeda, K. Ishikawa, M. Ito, M. Sekine, M. Hori, T. Kaminatsui, H. Hayashi, I. Sakai, and T. Ohiwa: J. Appl. Phys. 109 (2011) 084112.

[27] H. Yamamoto, K. Asano, K. Ishikawa, M. Sekine, H. Hayashi, I. Sakai, T. Ohiwa, K. Takeda, H. Kondo, and M. Hori: J. Appl. Phys. 110 (2011) 123301.

[28] H. Yamamoto, H. Kuroda, M. Ito, T. Ohta, K. Takeda, K. Ishikawa, H. Kondo, M. Sekine, and M. Hori: Jpn. J. Appl. Phys. 51 (2012) 016202.

[29] H. Nagai, S. Takashima, M. Hiramatsu, M. Hori, and T. Goto: J. Appl. Phys. 91 (2002) 2615.

[30] K. Ishikawa, Y. Yamaoka, M. Nakamura, Y. Yamazaki, S. Yamasaki, Y. Ishikawa, and S. Samukawa: J. Appl. Phys. 99 (2006) 083305.

[31] K. Kurihara, A. Egami, and M. Nakamura: J. Appl. Phys. 98 (2005) 084907.

[32] S. Uchida, S. Takashima, M. Hori, M. Fukasawa, K. Ohshima, K. Nagahata, and T. Tatsumi: J. Appl. Phys. 103 (2008) 073303.

[33] J. W. Fox, A. C. H. Smith, and E. J. Smith: Proc. Phys. Soc. London 73 (1959) 533.

[34] R. H. Fowler and L. Nordheim: Proc. R. Soc. London 119 (1928) 173.

Chapter 4 Temporal Changes of Absolute Densities of Atoms in H_2 and N_2 Mixture Gas Plasmas by Surface Modifications of Reactor Wall

4.1 Introduction

Plasma etching technologies are indispensable for the nanostructures fabrication by engraving patterns, trenches or holes along the etching masks in the underlying material [1,2]. Plasma deposition and surface modification processes are also important to synthesis thin films with high functionality and surface modifications of materials at a low temperature. It is widely known that behaviors of densities of chemical reactive species influenced much on plasma processes [3,4]. Recently, reactive plasmas employing the chemistry of H_2/N_2 mixture gas plasmas have been used in various kinds of material processes such etching of organic resists [5-12], chemical vapor deposition of nitrides [13], and so on. In the etching processes of low-dielectric constant (low-*k*) organic films using H_2/N_2 plasmas in the ultralarge scale integrated circuits (ULSIs), absolute densities of hydrogen (H) and nitrogen (N) atom and their relative ratio of H/ (H+N) affect considerably etched feature profiles [5-7]. In the processing, N atom is known to form a protective layer on the sidewall of the patterns against the etching species of H atom [14–19]. Nagai *et al*. reported that the etching profile of 65-nm line and space (L&S) mask-patterned low-*k* organics with H_2/N_2 mixture plasma was affected by just several percent of variation in the atom density ratio [14].

It has been a great concern for the precise control of plasma etching processing to discuss the condition of reactor wall surface influences the plasma chemistry in the reactor [20-22]. Particularly, it has become problems that the prior process and/or the exposure the ambient air for the maintenance of reactors could modify the surface

condition of the wall considerably and then influence the present etching process indirectly via the wall surface memory [23]. Recently, some papers have reported the reactor-wall's surface loss probabilities of species such as molecular atoms [24–26] and atoms [27–31] by using various diagnostic techniques such as absorption spectroscopy and appearance mass spectroscopy. However, many of the details of the interaction of plasma particles, such as ion, neutral, involving atom, metastable and so on, with the reactor wall and substrate are not clear because of complexity of the plasma processes.

In our previous study, Moon *et al.* indicated that the change of surface loss probability of H and N atoms was from 0.03 to 0.16 for the variety of wall materials and gas mixture ratio [18]. These changes of loss probability could affect the atom density near the wall.

In this chapter, we have focused on the study of influence of the modified surface by the various kinds of plasma exposures in the etching plasma processing on H and N atom densities in the H_2/N_2 mixture gas plasma. Based on the quantitatively measurement using vacuum ultraviolet absorption spectroscopy (VUVAS), the temporal changes of absolute densities of H and N atoms in the H_2/N_2 mixture plasma after each processes of the H_2 plasma, the N_2 plasma and the O_2 plasma as a cleaning were studied on the wall surface memory effects, i.e. influences of prior processes on the atom densities qualitatively and systematically in the H_2/N_2 plasma.

4.2 Experimental Details

The H_2/N_2 plasma was generated in a capacitively coupled plasma (CCP) reactor whose inner wall material was anodically-oxidized aluminum, which is similar to industrially commercialized etching tools. Gases of H_2 with a flow rate of 75 sccm and N_2 with a flow rate of 25 sccm were introduced to the chamber through the showerhead as a top electrode. The total gas pressure was kept at 2.0 Pa. A 100-MHz very high frequency (VHF) power of 400 W was supplied to the top electrode, and 2-MHz medium frequency (MF) of 200 W was supplied to the bottom electrode as a substrate bias. A self-bias voltage was -480 V for this condition. Substrate was fixed by an electrical-static chunk on a stage whose temperature was controlled with coolant circulation. Wafer temperature was -20°C before the plasma exposure, and 19.6°C at maximum at steady-state from plasma discharge after 30 s of ignition. Temperature of the chamber walls was room temperature without control. This condition is typically used for the etching of low-*k* organic materials [32,33].

Figure 4.1 shows a schematic diagram of the etch reactor and the setup for measuring the absolute density of H and N atoms near the reactor wall. A compact atom monitoring system consists of a micro-discharge hollow cathode lamp (MHCL), a VUV monochromator and optical component parts such as reflection mirror and MgF_2 windows [34-38]. The VUV light from MHCL was reflected by the aluminum (Al) mirror with the direction of 45 degrees and passed through the MgF_2 window and was absorbed in the plasma region. The VUV light passed through another MgF_2 window and reflected at Al mirror to a VUV monochromator with a photomultiplier tube. The absorption length was 40 mm. Its configurations in details are shown in elesewhere.[39) The transition lines for the absolute atom density measurement were the Lyman α at 121.6 nm for H atom, and $^4P_{5/2}$-$^4S^o_{3/2}$, $^4P_{3/2}$-$^4S^o_{3/2}$ and $^4P_{1/2}$-$^4S^o_{3/2}$ at 119.96, 120.02 and 120.07 nm for N atom [34-38]. All errors estimated by averaging over repeatable

measurements in three times are indicated in text.

Figure 4.2 shows the approach of this experiment. Before each experiment, chamber was exposed to several different plasmas (Step 1) for 3 min, (i) seasoning condition of H_2/N_2 plasma (seasoning), (ii) H_2 plasma, (iii) N_2 plasma, and (iv) O_2 plasma to intentionally change the chamber wall condition. Before each plasma exposures, the reactor wall was exposed to the O_2 plasma as cleaning for 3 min. In addition, a small piece of Al_2O_3 (anodized Al) was placed on the reactor wall and exposed to the plasmas with sequences as similar as the circumstance (e.g. the samples were prepared by exposing the different plasma conditions after the O_2 plasma cleaning for 3 min and the H_2/N_2 seasoning plasma for 3 min) and analyzed by X-ray photoelectron spectroscopy (XPS) to investigate the surface chemical composition after the wall modification by each process that could cause the variation of atom density in the following H_2/N_2 plasma. The results of XPS analysis will be discussed in section 4.3.4.

Subsequently after several plasma exposures, temporal change of H and N atom densities in H_2/N_2 plasma were analyzed for 2 min (Step 2). The results of radical density changes will be discussed in section 4.3.2.

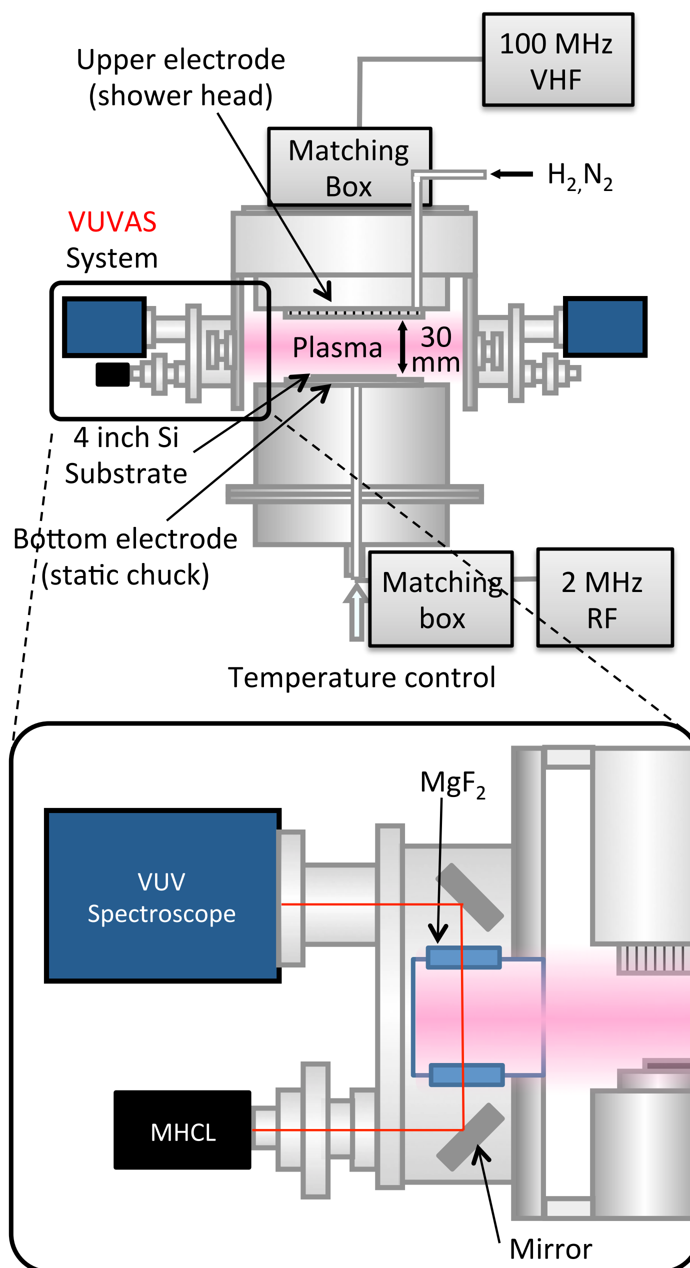

Figure 4.1 Schematics diagram of the experimental apparatus used for measuring the density of hydrogen and nitrogen atoms near the reactor wall employing a VUVAS system.

<u>Step 1: Change of wall condition</u>
Plasma : (i)H_2/N_2, (ii)H_2, (iii)N_2, (iv)O_2
Analysis: XPS
→Discussed in section 4.3.4

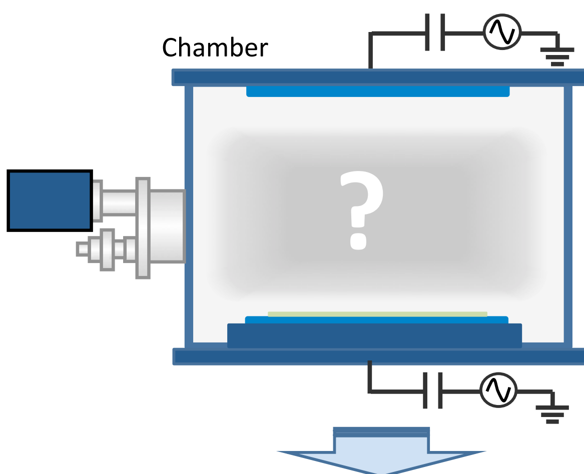

<u>Step 2: Temporal change of atoms density in H_2/N_2 plasma</u>
Plasma : H_2/N_2 plasma
Analysis : VUVAS
→Discussed in section 4.3.2

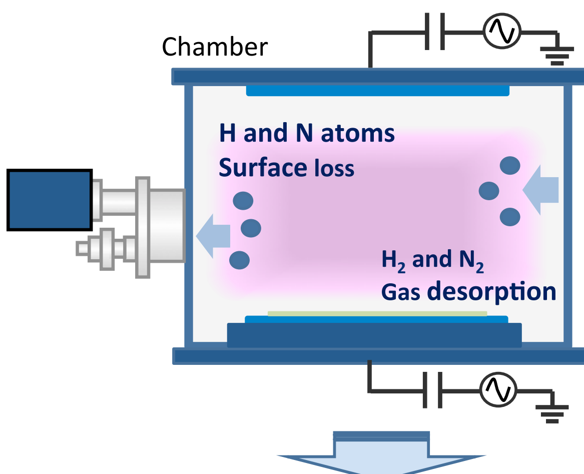

<u>Step 3: H_2 and N_2 gas desorption in O_2 plasma</u>
Plasma : O_2 plasma
Analysis : VUVAS
→Discussed in section 4.3.3

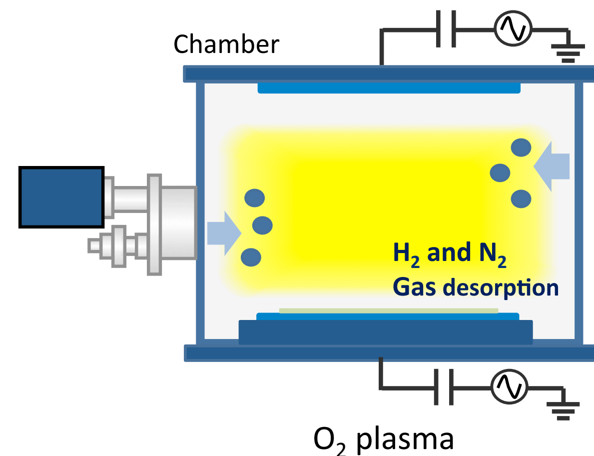

Figure 4.2 Schematics diagram of the experimental approach.

4.3 Results and Discussion

4.3.1 Generation and Loss of H and N atoms

The behavior of the H or N atom density can be described by the following rate equation: [30]

$$\frac{dN(HorN)}{dt} = \langle\sigma v\rangle n_e N(H_2 or N_2) - \frac{N(HorN)}{\tau_d} - k_r N^2(HorN)N(X) \qquad (4.1)$$

where N(H or N) and N(X) represent the atom density of H or N, the density of other species, *X*, reacting with the H or N atoms, respectively. σ is the generation cross-section of H or N atoms by one electron impact on H_2 or N_2, v is the velocity of electron, n_e is electron density, τ_d is the decay time constant of H or N atoms and k_r is the rate constant for the gas-phase recombination reaction among two H or N atoms and other species. The contribution of the gas phase reaction to the loss of H and N atom is small, since these reactions constant are too small to account for the observed decay time. Therefore, the term $k_r N^2(H\ or\ N)N(X)$ in the right hand side of Eq. (4.1) can be negligible.

The atoms reach the surface and some are reflected while others migrate along the surface, resulting in loss of atoms through chemisorption and recombination. Thus, the atom loss reaction caused by recombination on the wall can be represented by the product of the incident flux (Γ) and the surface loss probability (α). The surface loss of atoms is given by following equation: [30]

$$HorN_{loss} = \alpha\Gamma_{HorN} v_{HorN} = \frac{\alpha N(HorN)}{4}\sqrt{\frac{\pi m}{8k_B T}} \qquad (4.2)$$

where v is the thermal velocity, *N* is the density of atom, k_B is the Boltzmann constant, *T* is the temperature and m is the mass of the atom. The flux is a function of the atom temperature and density. This loss is equal to the term $\frac{N(HorN)}{\tau_d}$ in Eq. (1). Therefore,

the decay time constant is represented by

$$\tau_d = \frac{4}{\alpha}\sqrt{\frac{\pi m}{8k_BT}} \ . \tag{4.3}$$

From Eq. (1) and (3), the balance between generation and loss of H and N atom in the plasma at the steady state is represented by following equation

$$\langle\sigma v\rangle n_e N(H_2 or N_2) = \frac{N(HorN)}{\tau_d} \ . \tag{4.4}$$

Applying ideal gas law, the equation can be converted to

$$N(H) = \frac{4\langle\sigma v\rangle n_e p v}{\alpha RT}\sqrt{\frac{\pi m}{8k_BT}} \ . \tag{4.5}$$

As shown by this equation, the difference in surface loss provability, α, is directly related to the density of atom. Moon *et al*. indicated that the change of surface loss probability for H and N atom was between 0.03 - 0.16, depended on the wall material and gas mixture ratio. [30] This variation of loss probability might cause this five times increase of the atom density value at maximum.

4.3.2 Influence of Preceding Process on Atom Densities

Figure 4.2 shows temporal changes for N and H atom densities in the H_2/N_2 plasma in the reactor after (i) seasoning plasma, (ii) H_2 plasma, (iii) N_2 plasma and (iv) O_2 plasma. Temporal changes of the cases of (i) seasoning and (ii) H_2 plasma, the N atom density was stabilized just after the plasma ignition to be $1.0\pm0.1\times10^{11}$ cm^{-3} and the H atom density were stabilized just after the plasma ignition to be $1.2\pm0.2\times10^{11}$ cm^{-3}.

Only at the process of (i) seasoning, densities were stabilized almost the same value after the plasma treatment time of 30 s. In other case of the process of (ii) H_2 plasma, the stabilization needed 120 s.

In contrast, at the beginning of H_2/N_2 plasma after (iii) N_2 plasma and (iv) O_2 plasma, the N atom density was varied to be increase to $1.8\pm0.1\times10^{11}$ cm^{-3} for (iii) and $4.0\pm0.2\times10^{11}$ cm^{-3} for (iv). The H atom density was also increased $1.7\pm0.2\times10^{11}$ cm^{-3} after (iii) N_2 plasma and $2.0\pm0.3\times10^{11}$ cm^{-3} after (iv) O_2 plasma. After the plasma ignition, the N and H atom density decreased gradually in both cases of after (iii) N_2 and (iv) O_2 plasmas. The increase of atom density in the case of (iii) N_2 and (iv) O_2 plasmas are assumed to be induced by the surface modification of the reactor wall during the prior plasma exposure.

Figure 4.3 shows temporal changes for the atom density ratio, N/(H+N), calculated by the data represented in Fig. 4.2. It was reported that the atom density ratio of H/(H+N) has an important meaning to decide the etching rate and pattern profile of low-*k* organics in the H_2/N_2 plasma etching processing [14,15,32]. Therefore, the behavior of atom density ratio was evaluated after the various kinds of prior processes. The atom density ratio indicated 46% just after the ignition at (i) seasoning, 48% at (ii) H_2 plasma, as well as 50% at (iii) N_2 plasma. Although the temporal changes in atom densities as shown in Fig. 4.2 were significant in particular of (iii) N_2 plasma, the ratio

of atom densities was always stabilized.

On the other hand, the atom density ratio at the ignition was shown a low value of 30% in the case of (iv) O_2 plasma, subsequently gradual increase reached to a stable value of 48% after the discharge for 120 s. Those values in the ratios of atom densities were stabilized and reached a constant value with variations of approximately 10%, subsequently as the N_2/H_2 plasma discharge elapsed. It is noteworthy that the seasoning process needs at least for 120 s, prior to perform the etching process of low-*k* organics with the stabilization of the atom densities after the O_2 exposure as a cleaning of reactor walls.

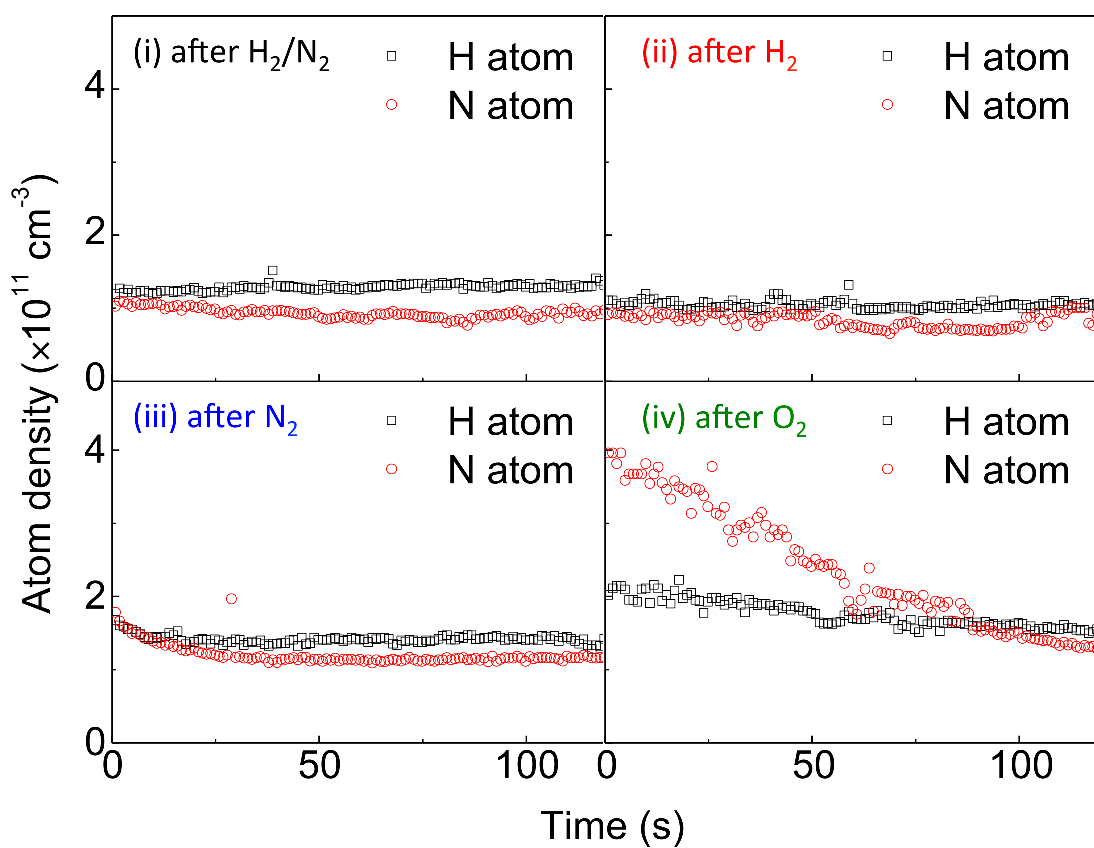

Figure 4.2 Temporal changes for nitrogen atom (N) atom density in the H_2/N_2 plasma subsequently, after the various plasma exposures after (i) H_2/N_2 plasma, (ii) H_2 plasma, (iii) N_2 plasma and (iv) O_2 plasma.

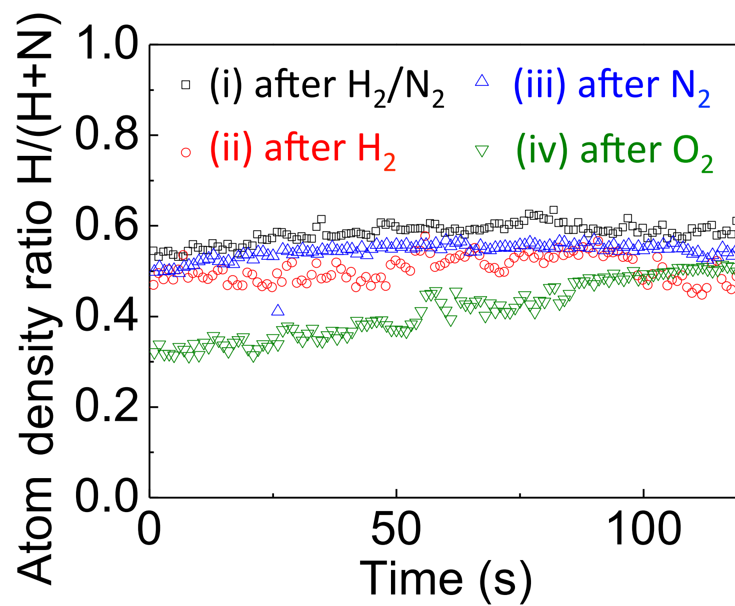

Figure 4.3 Temporal change for atom density ratio, H/(H+N), calculated by data represented in Fig. 2 (a)-(d).

4.3.3 Decay of Atom Density in O_2 plasma after H_2/N_2 Plasmas

The temporal changes for the densities of H and N atoms in O_2 plasma after the H_2/N_2 plasma are shown in Fig. 4.4. Absolute densities just after the ignition of the H_2/N_2 plasma were values of $8.2\pm0.3\times10^{11}$ cm^{-3} for H atom and $6.1\pm0.2\times10^{11}$ cm^{-3} for N atom. Upon elapsing periods of 50 s for H atom and 10 s for N atom, those atom densities were disappeared to reach values less than the detection limit. This result suggests that H and N atoms were generated by emissions of certain absorbates from the reactor wall into the plasma, while the absorbates emission under the O_2 plasma exposure.

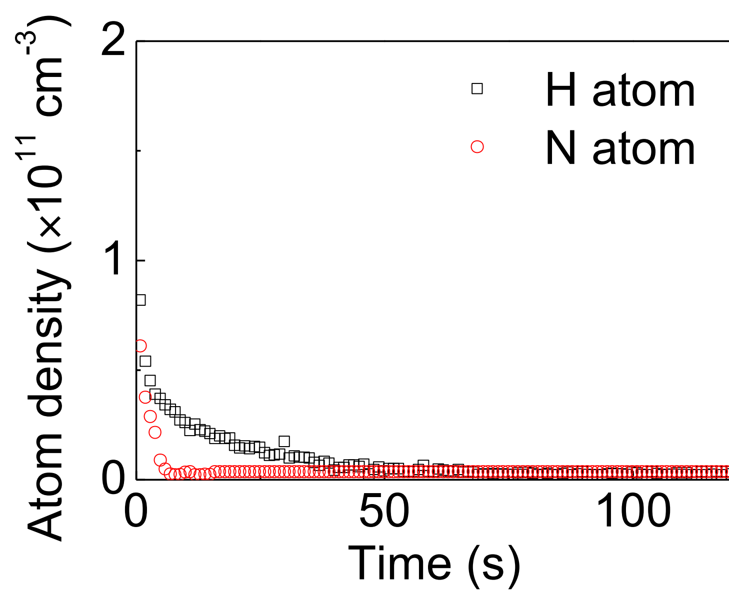

Figure 4.4 Temporal changes for hydrogen (H) and nitrogen (N) atom density in the O_2 plasma after H_2/N_2 plasma.

4.3.4 XPS Analyses on Al_2O_3 Film as a Reactor Wall Material

To investigate surface conditions after each plasma exposure, XPS analyses were performed on Al_2O_3 film set on the reactor wall as a reactor wall material exposed to the plasma. Figure 4.5 (a) shows XPS spectra for Al 2*p* on the Al_2O_3 piece. Spectral changes exhibited clearly upon different kinds of pre-treatment of plasmas. The peak was decomposed into two Gaussian peak components by fitting the spectra. A component (#1) at 73.5 eV can be assigned to be aluminum bound to nitrogen[40)] and called hereafter "AlN". Another component (#2) at 76.7 eV can be assigned to be aluminum bound to oxygen in wurtzite Al_2O_3 [40] and called hereafter "AlO". Apparently the AlN component (#1) was exhibited in the spectra of Al 2*p* on the surface exposed to the (i) H_2 and N_2 mixture plasma and (iii) N_2 plasma. Intensities of the AlN component (#1) on the surface exposed to the (ii) H_2 and (iv) O_2 plasmas were exhibited negligibly low. Intensities of the AlO component (#2) for all samples exposed to plasma processes remained almost a constant. This result indicates that the plasma exposure without N_2 gas such as the (ii) H_2 mixture plasma and (iv) O_2 plasma resulted in reducing Al-N bonds on the surface.

Figure 4.5 (b) shows N 1*s* spectra of the Al_2O_3 exposed to each plasma process. The spectra of N 1*s* of the samples exposed to the (i) H_2/N_2 plasma and (iii) N_2 plasma shows an asymmetric shape. As referred from previous publications with respect to the peak assignment [40-42], the peak was decomposed into three Gaussian peak components; the 1st component (#1) at 395.0 eV, the 2nd component (#2) in at 397.0 eV, and the 3rd component (#3) at 399.6 eV. On the basis of electron-transferring environment of nitrogen bound to other atoms. The lowest component (#1) can be assigned to the nitrogen adsorbed physically on the sample surface. The component (#2) in N 1*s* is assigned to the nitrogen bound to aluminum in AlN. The component (#3) in N 1*s* is assigned to the nitrogen, in which electron transfers to aluminum bound to oxygen,

e.g. in alumina (Al_2O_3), "N-Al-O" [40].

Intensities of three peak components in N 1*s* decreased on the surface exposed to the (ii) H_2 and (iv) O_2 plasmas. The AlN peaks in both Al 2*p* and N 1*s* were corresponded with each other. Namely, the plasma exposure including N_2 gas resulted in reducing Al-O bonds and forming Al-N bonds covered on the surface. The amount of N atoms on the surface in the N_2 plasma was higher than those in other plasmas. The surface N rich layer may induce unintentional desorption of the N atom from the surface during the H_2/N_2 mixture plasma exposure and the primitive increase of N radical as discussed before.

In the analysis of XPS, chemical structures of hydride surfaces exposed to H_2 and H_2/N_2 plasmas and their effects to the interaction with radicals have not been yet made clear that and the furthermore study is necessary.

Figure 4.5 (c) shows O 1*s* spectra of the Al_2O_3 exposed to each plasma process. The spectra of O 1*s* on the surface exhibited peak at 531.6 eV, and it is assigned to oxygen bound to aluminum in α-Al_2O_3 [40]. Spectral intensity increased only case of the (iv) O_2 plasma. This indicates that an amount of the Al-O bonds exposed was increased after the (iv) O_2 plasma by oxidation of the covered Al-N bonds on the surface.

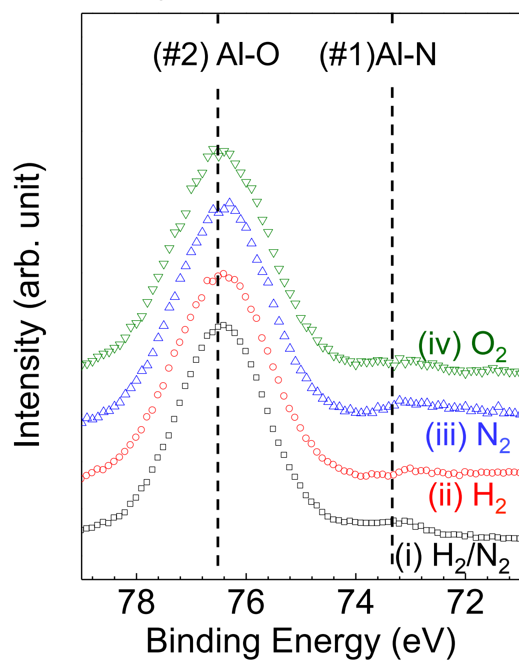
(a) Al 2p
(#2) Al-O
(#1)Al-N
Intensity (arb. unit)
(iv) O2
(iii) N2
(ii) H2
(i) H2/N2
78
76
74
72
Binding Energy (eV)

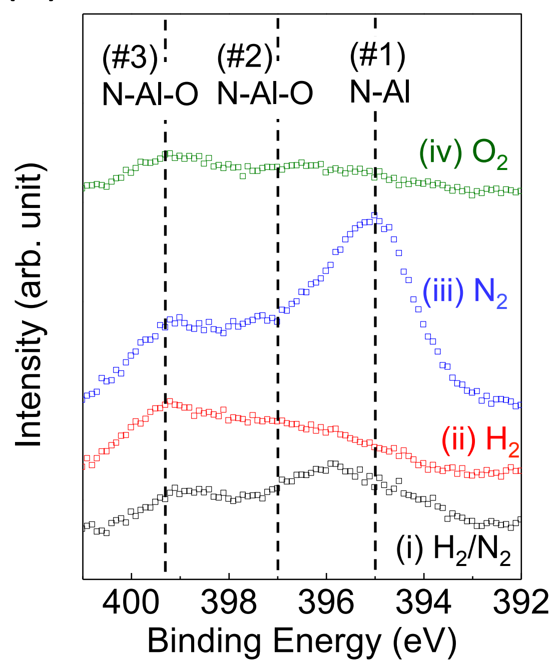
(b) N 1s
(#3)
N-Al-O
(#2)
N-Al-O
(#1)
N-Al
Intensity (arb. unit)
(iv) O2
(iii) N2
(ii) H2
(i) H2/N2
400
398
396
394
392
Binding Energy (eV)

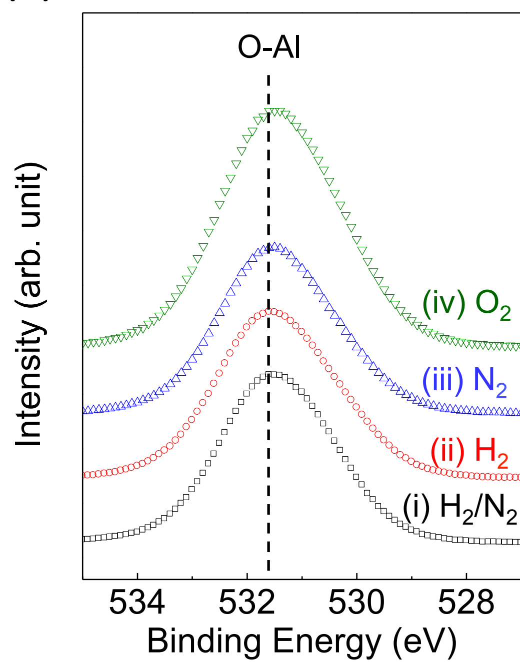

Figure 4.5 XPS spectra of (a) Al 2*p*, (b) N 1*s* and (c) O 1*s* on Al_2O_3 plate exposed to (i) H_2/N_2, (ii) H_2, (iii) N_2 and (iv) O_2 plasma after (i) H_2/N_2 seasoning plasma after (iv) O_2 cleaning plasma.

4.3.5 Importance of Loss Process on Reactor Wall

In the discussion on the mechanism of these behaviors of H or N atom densities, the atom density can be usually described by a balance between the generation by the electron impact dissociation and the loss of recombination and surface sticking at both the gas phase and the reactor wall surface. The contribution of the gas phase reactions with respect to the loss of H and N atom might be regarded to be negligible small, since these reactions hardly occur at low pressures in this experimental condition. This was also supported by observation of decay time of atom density in afterglow plasma [43]. Therefore, the atom loss reaction will be caused dominantly by the loss on the reactor wall surface.

The surface loss can be represented by a product of the incident flux (Γ) and the surface loss probability (α) [43], and then the atom density *N* is given by $\propto \frac{\Gamma}{\alpha}$. Thus, in this condition, the surface loss probability α is directly related to the density of atom. In fact Moon *et al.* indicated that the surface loss probabilities for H and N atom ranged between 0.03 and 0.16, depending on the wall materials and gas mixture ratio [18,19]. This variation of loss probability will cause the influence on the atom densities in the range of 5 factors at maximum.

In addition, except for the condition of (iv) O_2, densities of H and N atom in H_2/N_2 mixture plasmas after (iii) N_2 plasma were higher than those after (i) H_2/N_2 and (ii) H_2 plasmas. The surfaces exposed to the hydrogen-containing plasma indicated no difference in loss properties of atoms on the surface, unlikely it was observed that both N and H atom densities were increased with maintaining the ratio of densities on the surface after (iii) N_2 plasma. Accordingly, it should be taken into a consideration of hydrogenation of the wall-surface.

The effect of hydrogen into a N_2 plasma on the iron plate was reported to be increased in the sticking coefficient on the reactor wall surface. This was interpreted

that the work function of iron decreased in the presence of coadsorbed hydrogen.[44] The experiment results observed in (i) H_2/N_2 and (ii) H_2 plasmas can be interpreted by the similar hydrogenation mechanism that lowering the work function, which led to an increase of chemisorption on the surface and to enhance the surface loss probability. Further considerations with respect to the hydrogenation are needed in the future.

Lastly, the values of H and N atom densities in H_2/N_2 mixture plasmas after (iv) O_2 plasma was significantly higher than those after (i) H_2/N_2, (ii) H_2 and (iii) N_2 plasmas. The atom density of N atom differed significantly in the H_2/N_2 mixture plasmas after (iv) O_2 plasma than the other processes. This is probably due to the changes in the surface loss of the reactor wall. The surface loss of H and N atoms in the H_2/N_2 mixture plasma on the surface of Al_2O_3 covered with nitrogen or oxygen in the H_2/N_2 plasma was lower than that covered with hydrogen atom. Consequently the experiments results of the (iii) N_2 and (iv) O_2 plasmas indicate clearly that both the nitridation and the oxidation on the chamber wall surface decrease the sticking coefficients, as resulted from the change of the surface coverage of elements on the reactor wall of the anodized aluminum as the surface material.

4.4 Conclusion

Temporal changes of absolute densities of H and N atoms in the H_2/N_2 plasma after several plasma exposures in the reactor were clarified. The densities of both H and N atoms in the H_2/N_2 plasma just after O_2 plasma were significantly influenced by the reactor wall surface comparing with plasmas of H_2/N_2, H_2 and N_2. The N atom density increased 290% and the H atom density increased 70% compared to the stable value after the seasoning process of O_2 plasma due to the interaction between the plasma and the reactor wall surface.

Dramatic changes in atom densities indicate that the chemical modifications such as oxidation and nitridation of reactor wall surface affected the surface loss of atom species. As the results, it was revealed that the reactor-wall conditions have the memory effect which affected on the temporal behavior of atom densities. The quantitative measurements of absolute atom density proved the correlations of the plasma condition with the reactor wall condition. Thus the control of the wall surface condition was crucially important in achievement of stabilizing in the atom densities. In establishing highly reliable plasma processes, the interactions between the surface and the plasma need to understand throughout determining mechanisms. In addition, the real time stabilization process of atom densities on the basis of the real time monitoring of atom densities hopes to enable steady controls in the absolute atom densities and their relative ratio for realizing the high performance of plasma processing.

4.5 References

[1] H. Abe, M. Yoneda, and N. Fujiwara: Jpn. J. Appl. Phys. **47** (2008) 1435.

[2] V. M. Donnelly and A. Kornblit: J. Vac. Sci. Technol. A **31** (2013) 050825.

[3] M. Sekine, Appl. Surf. Sci. **192** (2002) 270.

[4] G. S. Oehrlein, R. J. Phaneuf, and D. B. Graves: J. Vac. Sci. Technol. B **29** (2011) 010801.

[5] M. Fukasawa, T. Tatsumi, T. Hasegawa, S. Hirano, K. Miyata, and S. Kadomura: Proc. on Dry Process Symposium (Tokyo, 1999) p. 221.

[6] Y. Morikawa, S. Yasunami, W. Chen, T. Hayashi, and T. Uchida: J. Vac. Sci. Technol. **A** 19 (2001) 1747.

[7] Y. Morikawa, T. Hayashi, and T. Uchida: Jpn. J. Appl. Phys. **42** (2003) 1441.

[8] Y. Yamaoka, K. Kurihara, K. Karahashi, M. Sekine, and M. Nakamura: Ext. Abstr. Electrochemical Society 201st Meet. (ECS2002 Spring), 2002, p. 410.

[9] K. Kurihara, A. Egami, and M. Nakamura: J. Appl. Phys. **98** (2005) 084907.

[10] K. Ishikawa, Y. Yamaoka, M. Nakamura, U. Yamazaki, Y. Ishikawa, and S. Samukawa: J. Appl. Phys. **99** (2006) 083305.

[11] K. Van Laer, S. Tinck, V. Samara, J. F. de Marneffe, and A Bogaerts: Plasma Sources Sci. Technol. **22** (2013) 025011.

[12] X. Liu, S. Gill, F. Tang, S. W. King, and R. J. Nemanich: J. Vac. Sci. Technol. B **30** (2012) 031212.

[13] Lu Yi, H. Kondo, K. Ishikawa, O. Oda, K. Takeda, M. Sekine, H. Amano, and M. Hori, to be submitted.

[14] H. Nagai, S. Takashima, M. Hiramatsu, M. Hori, and T. Goto: J. Appl. Phys. **91** (2002) 2615.

[15] H. Nagai, M. Hiramatsu, M. Hori, and T. Goto: J. Appl. Phys. **94** (2003) 1362.

[16] H. Nagai: Dr. Thesis, Department of Quantum Engineering, Nagoya University,

Nagoya, 2003.

[17] S. Uchida, S. Takashima, M. Hori, and M. Fukasawa: Jpn. J. Appl. Phys. **47** (2008) 3621.

[18] C. S. Moon, K. Takeda, M. Sekine, Y. Setsuhara, M. Shiratani, and M. Hori: J. Appl. Phys. **107** (2010) 113310.

[19] C. S. Moon, K. Takeda, M. Sekine, Y. Setsuhara, M. Shiratani, and M. Hori: Appl. Phys. Express **2** (2009) 096001.

[20] G. Cunge, M. Kogelschatz, and N. Sadeghi: Plasma Sources Sci. Technol. **13** (2004) 522.

[21] M. Schaepkens, R. C. M. Bosch, T. E. F. M. Standaert, G. S. Oehrlein, and J. M. Cook: J. Vac. Sci. Technol. A **16** (1998) 2099.

[22] T. W. Kim and E. S. Aydil: J. Electrochem. Soc. **150** (2003) G418.

[23] A. Agarwal and M. J. Kushner, J. Vac. Sci. Technol. A **26** (2008) 498.

[24] N. Itabashi, K. Kato, M. Magane, S. Naito, T. Goto, A. Matsuda, C. Yamada, and E. Hirota: Jpn. J. Appl. Phys. **29** (1990) L505.

[25] Y. Hikosaka, H. Toyoda, and H. Sugai: Jpn. J. Appl. Phys. **32** (1993) L690.

[26] K. Sasaki, K. Usui, H. Furukawa, C. Suzuki, and K. Kadota: Jpn. J. Appl. Phys. **37** (1998) 5047.

[27] J. P. Booth and N. Sadegi: J. Appl. Phys. **70** (1991) 611.

[28] Y. Hatanaka and S. Mickramanayaka: Vacuum **35** (1992) 894. [in Japanese]

[29] S. Takashima, M. Hori, T. Goto, A. Kono, and K. Yoneda: J. Appl. Phys. **90** (2001) 5497.

[30] M. Hori and T. Goto: Appl. Surf. Sci. **253** (2007) 6657.

[31] G. A. Curley, L. Gatilova, S. Guilet, S. Bouchoule, G. S. Gogna, N. Sirse, S. Karkari, and J. P. Booth: J. Vac. Sci. Technol. A **28** (2010) 360.

[32] H. Yamamoto, H. Kuroda, M. Ito, T. Ohta, K. Takeda, K. Ishikawa, H. Kondo, M. Sekine, and M. Hori: Jpn. J. Appl. Phys. **51** (2012) 016202.

[33] T. Suzuki, K. Ishikawa, K. Takeda, H. Kondo, M. Sekine, and M. Hori: Jpn. J. Appl. Phys. **52** (2013) 120203.

[34] S. Takashima, M. Hori, T. Goto, A. Kono, M. Ito, and K. Yoneda: Appl. Phys. Lett. **20** (1999) 3929.

[35] K. Murata, Y. Mizutani, E. Iwasaka, S. Takashima, M. Hori, T. Goto, S. Samukawa, and T. Tsukada: Jpn. J. Appl. Phys. **40** (2001) L4.

[36] S. Takashima, M. Hori, T. Goto, and K. Yoneda: J. Appl. Phys. **89** (2001) 4727.

[37] S. Takashima, S. Arai, M. Hori, T. Goto, A. Kono, M. Ito, and K. Yoneda: J. Vac. Sci. Technol. A **19** (2001) 599.

[38] H. Nagai, M. Hiramatsu, M. Hori, and T. Goto: Rev. Sci. Instrum. **74**, (2003) 3453.

[39] S. Takahashi, R. Kawauchi, S. Takashima, S. Den, T. Katagiri, H. Kano, T. Ohta, M. Ito, T. Suzuki, K. Takeda, and M. Hori: Jpn. J. Appl. Phys. **51** (2012) 076502.

[40] L. Rosenberger, R. Baird, E. McCullen, G. Aunerc, and G. Shrevea: Surf. Interface Anal. **40** (2008) 1254.

[41] P. M. Raole, P. D. Prabhawalkar, D. C. Kothari, P. S. Pawar, and S. V. Gogawale: Nucl. Instrum. Method. B **23** (1987) 329.

[42] M. A. Rooke, J. A. Rotole, and P. M. A. Sherwood: J. Vac. Sci. Technol. A **13** (1995) 1299.

[43] Y. Abe, A. Fukushima, K. Takeda, H. Kondo, K. Ishikawa, M. Sekine, and M. Hori: J. Appl. Phys. **113** (2013) 013303.

[44] S. Bockel, J. Amorim, G. Baravian, A. Ricard, and P. Stratil: Plasma Source. Sci. Technol. **5** (1996) 567.

Chapter 5 Reactor Wall Loss Properties Influenced by the Preceding Process

5.1 Introduction

Plasma-surface interaction is one of the most important research areas in the development of plasma processes. Plasma parameter changes temporally affected by the condition of chamber wall (inner wall), which is in contact with the plasma. However many of the details of the interaction of plasma particles, such as ion, atom and neutral with solid surfaces such as a substrate and walls are not clear because of complexity of the plasma process. Recently, a number of papers have reported chamber-wall's surface loss probabilities of species such as molecular atoms [1–3] and atoms [4–6] by using various diagnostic techniques such as absorption spectroscopy and appearance mass spectroscopy. Moon et al. indicated the change of surface loss probability of H and N atom from 0.03 to 0.16 as a function of different wall materials and gas mixture ratio [7].

In this chapter, I focused on the influence of preciding processes on the loss probabirity on the reactor wall in H_2/N_2 plasmas. Temporal changes of hydrogen (H) and nitrogen (N) atoms' loss probabilities were about investigated quantitatively in the H_2/N_2 mixture plasma subsequently after a different kind of plasmas by employing vacuum ultraviolet absorption spectroscopy (VUVAS) The influence of the process history was evaluated in various sequences of different kinds of plasma.

5.2 Experimental Details

Figure 5.1 shows a schematic diagram of the experimental arrangement for measuring surface loss probabilities of H, N atoms in H_2/N_2 afterglow plasma employing vacuum ultra-violet absorption spectroscopy (VUVAS) system with an atmospheric pressure microdischarge hollow cathode lamp (MHCL) as a light source. The dimensions of the process apparatus are 146 mm in diameter and 200 mm in height. The process input power with radio frequency (rf) of 13.56 MHz was supplied to the inner antenna coated by Al_2O_3 to prevent contaminations. To survey the decay curve of atom density in the afterglow plasma, a dc pulsed voltage with a repetition of frequency of 10 Hz (on:25 ms, off:75 ms) was applied to generate the plasma and continuous wave (cw) power was supplied to sustain the discharge of MHCL. The process chamber and VUVAS system were differentially pumped by two capillary plates since VUV transparent widows were located at each end of port of VUV monochromator and MHCL [11]. The transition lines for the measurements of absolute atom densities were Lyman α at 121.6 nm for H atom and $^4P_{5/2}$-$^4S^0_{3/2}$, $^4P_{3/2}$ -$^4S^0_{3/2}$ and $^4P_{1/2}$-$^4S^0_{3/2}$ at 120.0 nm for N atom. Surface loss probabilities of H, N atoms were investigated as a function of gas mixture ratio and kinds of wall materials. Especially, in order to examine the dependence of surface loss probabilities on the wall materials, all walls in the chamber were covered with each material. The detailed process conditions were shown in Table 5.1.

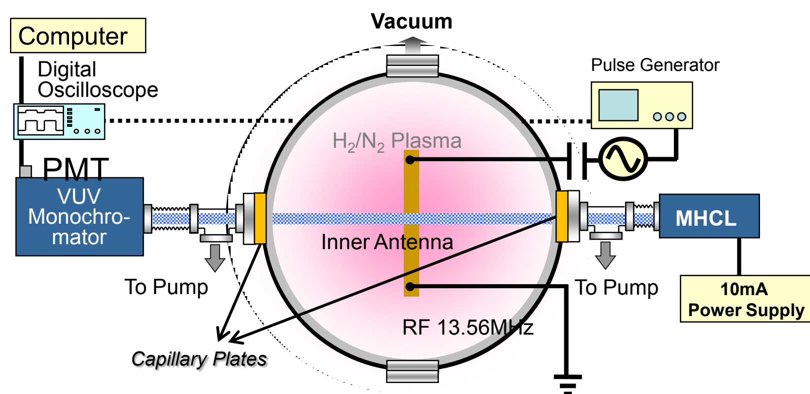

(a)

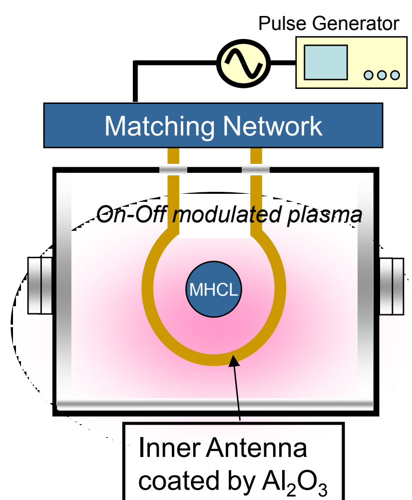

(b)

Figure 5.1 Schematic diagrams of (a) top view and (b) side view of reactor for measuring surface loss probabilities of H, N atoms in the afterglow plasma employing VUVAS system.

5.3 Results and Discussion

5.3.1 Importance of Sticking and Loss Probabilities of Atoms [16]

In plasma processing, the primary reaction in the plasma is caused by collisions between fast electrons and feed gases which are selected depending on the processes. The decomposition products consist of positive and negative ionic species and neutral species such as molecular species and neutral atoms. For example, for H_2 molecules, most H atoms are produced by electron impact dissociation of H_2:

$$H_2 + e \rightarrow H + H + e \tag{5.1}$$

In the case of removal pumping, the residence time under the conditions employed was estimated to be 470 ms, which was sufficiently longer than the observed decay times (0.4 ~ 2.0 ms). Therefore, the pumping action is considered to be negligible as a possible loss mechanism. On the other hand, the removal processes of H atoms are due to three-body recombinations with other species including H atoms and diffusion to the surface. Accordingly, the behavior of the H atom density can be described by the following rate equation:

$$\frac{dN(H)}{dt} = \langle \sigma v \rangle n_e N(H_2) - \frac{N(H)}{\tau} - k_r N^2(\mathrm{H}) N(\mathrm{X}) \tag{5.2}$$

where N(H), N(H_2) and N(X) represent the H atom density, the H_2 density and the density of other species (X) reacting with the H atoms, respectively, σ the generation cross-section of H atoms by one electron impact on H_2, ν the thermal velocity of the electron, n_e the electron density, τ the decay time constant of H atoms and k_r is the rate

constant for the three-body reaction among two H atoms and other species. Collision frequency (ν) with an electron is determined by the following equation:

$$\nu = \frac{1}{n_e \langle \sigma v \rangle} \tag{5.3}$$

The incident flux (Γ) of neutral atoms on the surface is given by following equation:

$$\Gamma = \frac{n}{4}\sqrt{\frac{8k_B T}{\pi m}} \tag{5.4}$$

where n is the atom density, k_B the Boltzmann constant, T the temperature of the atom and m is the mass of the atom. The flux is a function of the atom temperature and density. Next, the atoms reach the surface and some of atoms are reflected while others diffuse on the surface resulting in sticking and re-desorption through recombination.

Figure 5.2 illustrates the surface reaction scheme. The ($1-\beta$) is the reflection factor, γ is the recombination desorption and the desorption factor and s is the surface reaction factor (sticking probability). Generally, the surface loss probability means $\beta = \gamma + s$. Therefore, the flux (Γ), the sticking coefficient (s) and surface loss probability (β) are the most important parameters to characterize plasma processes. In this chapter, β for H, N atoms were estimated for various kinds of wall material and plasma conditions such as gas mixture ratio.

5.3.2 Loss Kinetics of H and N Atoms in Afterglow of H_2/N_2 Mixture Plasma

Before the measuring, the loss mechanisms of H, N atoms in the afterglow plasma have to be discussed. The possible loss mechanisms for H, N atoms could be considered by three kinds of loss ways such as the removal by pump action, the gas-phase recombination, and the diffusion followed by wall recombination.

In first case of the removal by pumping, the residence time under our conditions was 470 ms, and it was sufficiently longer than the observed decay times (H atom: 0.5 ~ 1.8 ms, N atom: 0.9 ~ 3 ms). Therefore, the pump action can be dismissed as a possible loss mechanism.

Second, the relevant gas-phase reactions were taken into consideration [13].

(I) $N + N + M \rightarrow N_2 + M$, $k = 8.3\times10^{-34}exp(500/T)\ cm^6s^{-1}$

(II) $H + H + M \rightarrow H_2 + M$, $k = 8.8\times10^{-33}(300/T)\ cm^6s^{-1}$

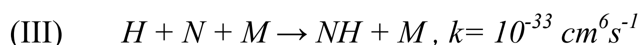

(III) $H + N + M \rightarrow NH + M$, $k = 10^{-33}\ cm^6s^{-1}$

(IV) $N + NH_2 + M \rightarrow NH_3 + M$, $k = 5.5\times10^{-30}\ cm^6s^{-1}$

Since these reaction constants are too small to account for the observed decay times, the loss of atom by the gas-phase recombination could be negligible. After all, diffusion followed by wall recombination would be main loss mechanisms of atoms. These could include a lot of reactions such as physical adsorption and desorption, chemical adsorption and desorption, reaction of chemisorbed atoms, the surface diffusion of physisorbed atoms and so on.

In order to clarify the loss kinetics of the H, N atoms in H_2/N_2 plasma, the decay curves of N and H atom densities in the afterglow plasma were measured as a function of working pressure. Surface loss probabilities of H, N atoms on stainless-steel and Ni walls were estimated. Figure 5.3 shows typical decay curves of H and N atom

densities in the afterglow plasma generated from on-off modulated H_2/N_2 mixture discharge at a pulsed rf power of 200W (on period: 25 ms, off-period: 75 ms), pressures of 3.3 to 13.3 Pa, and gas mixture ratio, $H_2/(H_2+N_2)$, of 0.2. As shown in Fig. 5.3, the decay curves of N atom densities measured at various pressures were well fitted with exponential functions, and the slope of decay curve was steeper for the lower gas pressure.

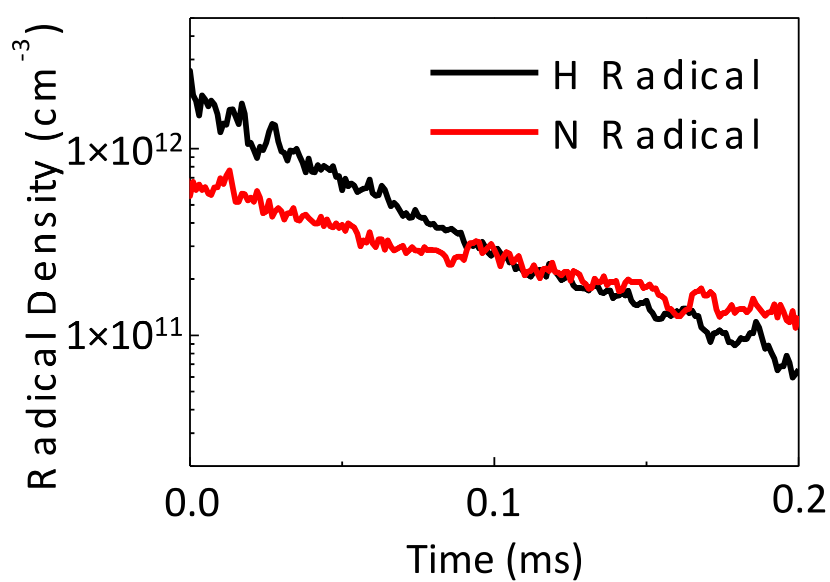

Figure 5.2 Typical decay curves of H and N atom density under the wall covered with stainless-steel.

The extinctions of H, N atoms in the afterglow are given by

$$\frac{dN(H_{or}N)}{dt} = -\frac{N(H_{or}N)}{\tau_d} - k_r N_n(H_{or}N)N(x). \tag{5.5}$$

where *N(H $_{or}$ N)* is H or N atom density, *N(x)* is the density of the main reaction species with H or N atom, τ_d is the decay time constant of atom, and k_r is the reaction rate constant between atom and reaction species. As shown in Fig. 5.4, the decay time constant of N atom increases with increase of working pressure. The contribution of gas phase reaction to the loss reaction of N atom is small as described above. Therefore, the term $k_r N_n$(H or N)N(x) in Eq. (5.5) could be negligible. Solving this rate equation, I have obtained a single exponential function for the decay of atom concentration in the afterglow plasma

$$N(H_{or}N) = N_0(H_{or}N)\exp(-t/\tau_d), \tag{5.6}$$

where N_0*(H or N)* is the initial atom density. Therefore, the measured decay time constant corresponds to the decay time constant τ_d. This single exponential equation is very well fitted with experimental results as shown in Fig. 5.3.

Figure 5.4 shows the decay time constant of N atom as a function of working pressure and gas mixture ratio in the afterglow plasma. The decay time constants were increased as the working pressure and hydrogen gas ratio were increased in the process chamber covered with stainless steel. Since the atom in the afterglow plasma could be mainly extinct by the reaction with wall, more collisions in a higher working pressure resulted in a longer decay time constant. To the contrary, the atom by less collisions at a lower working pressure could arrive to the wall relatively fast and as a result, the decay time was decreased due to the reaction with the wall.

In the first case of removal by pumping, the residence time under the conditions employed was estimated to be 200 ms, which was sufficiently longer than the observed decay times (0.4-2.0 ms). Therefore, the pumping action is considered to be negligible as a possible loss mechanism. The measured decay time constant, corresponds to losses by diffusion followed by reactions on the wall surface and reaction with H_2:

$$\tau = \frac{1}{1/\tau_d + kN(H_2)}. \tag{5.7}$$

From the equation the effective diffusion lifetime taking into account the surface loss probability according to the model of Chantry [30] is represented by:

$$\tau_d = \frac{1}{1/\tau + kN(H_2)}. \tag{5.8}$$

Therefore, τ_d is calculated using τ, the reaction rate constant $k_1 = 8.8\times10^{-33}(300/T)^{0.6}$ cm^6s^{-1} and the density of H_2. The density of H_2 is estimated form the pressure of H_2. The dissociation ratio of H_2 in the plasma afterglow is not significantly influence on results shown here, because the term of 1/ is one or two order higher in magnitude compared with the term of $kN(H_2)$. The diffusion lifetime τ_d is represented by

$$\tau_d = \frac{p\Lambda^2}{D}, \tag{5.9}$$

where p is pressure, Λ is an effective diffusion length, Λ_0 and D is the diffusion coefficient for H radicals. A simple approximation of Λ^2 was proposed by Chantry $\Lambda^2 = \Lambda_0^2 + l_0\lambda$, where and l_0 are the geometric diffusion length and the volume to area ratio of the chamber, and is determined by a surface boundary condition and expressed by

$$\lambda = \frac{4D}{v}\left(\frac{1-\alpha/2}{\alpha}\right), \tag{5.10}$$

where v is the velocity of H radicals given by $(8kT/\pi M)^{1/2}$, T and M are the temperature

and mass, respectively, and k is the Boltzmann constant, and α is the surface loss probability on the chamber wall. For a cylinder of radius R and height H, Λ_0^2 and l_0 are

$$\frac{1}{l_0} = \left(\frac{\pi}{H}\right) + \left(\frac{2.405}{R}\right)^2. \tag{5.11}$$

$$l_0 = \frac{RH}{2(R+H)}. \tag{5.12}$$

These expressions of Λ^2 are actually rigorous in two limiting cases: (i) high pressure and/or α → 1 where $\Lambda^2 = \Lambda_0^2$, and (ii) low pressure and/or α → 1 where $\Lambda^2 \approx l_0 4D/v\alpha$, and accounts for intermediate cases within a 10% error. From these equations, τ_d is represented by the following equation

$$\tau_d = \frac{p\Lambda_0^2}{D} + \frac{2l_0(2-\alpha)}{v\alpha}. \tag{5.13}$$

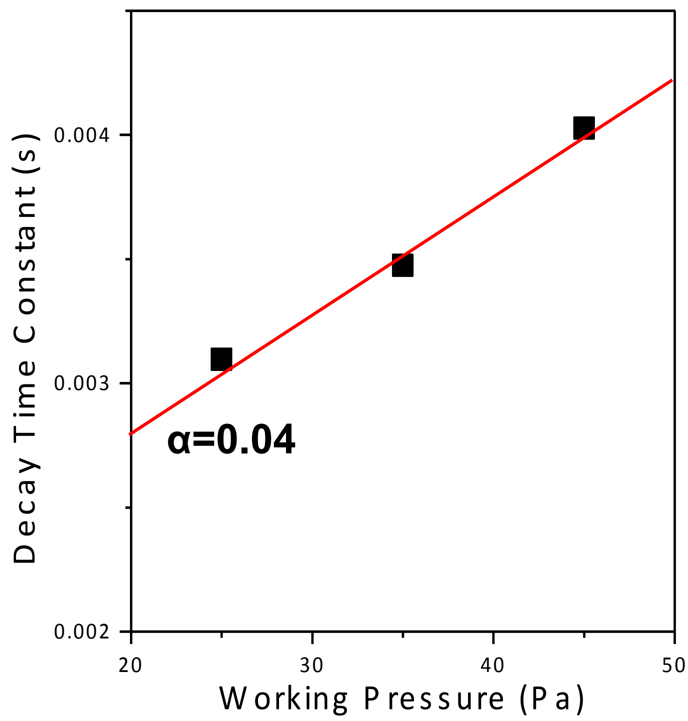

Figure 5.3 Decay time constants of N atom densities as a function of working pressure on stainless steel wall.

This lifetime (decay time constant, τ_d) from those results above is well represented by the following equation [14]:

$$\tau_d = \frac{p\Lambda_0^2}{D} + \frac{2l_0(2-\alpha)}{v\alpha} , \qquad (5.14)$$

where p is pressure, D is the diffusion coefficient for H or N atoms. Λ_0 is the geometrical diffusion length determined by the chamber structure [$\Lambda_0^{-2} = (\pi/L)^2+(2.405/R)^2$: in the present study, height L is 20 cm and radius R is 5.3 cm], $l_0 = V/S$ with the volume (V) band surface area (S) of the chamber and v is the velocity of H or N atoms given by $(8kT/\pi M)^{1/2}$ [T and M are temperature (400K) and mass of H, N atoms, respectively, and k is Boltzmann constant]. α is the surface loss probability on the chamber wall. The diffusion coefficient D was determined from the slope shown in Figure 5.4. D of N atom (at 400 K) in H_2/N_2 mixture plasma was estimated to be 1.1×10^5 cm$^2\cdot$Pa/s. This value was well similar to 1.0×10^5 cm$^2\cdot$Pa/s reported in Reference [15], which was acceptable compared to theoretical calculation for binary gas systems at low pressure (D = 1.2×10^5 cm$^2\cdot$Pa/s at 400K) by the Chapman-Enskog theory with the Lennard-Jones intermolecular potential [16, 17]. From this result, the surface loss probability on the chamber wall was estimated.

5.3.3 Dependence of Surface Loss Probabilities of H and N Atoms for Different Preceding Processes

As calculated in 5.3.2, surface loss probabilities of H, N atoms on different wall materials were investigated with changing the preceding process. Figure 5.5 shows the dependence of surface loss probabilities of H, N atoms as a function of different preciding processes. Surface loss probabilities of H, N atoms in H_2 and N_2 mixture plasma after H_2/N_2 plasma (seasoning), (a) H_2 plasma, (b) N_2 plasma and (c) air exposure were significantly higher than those in H_2/N_2 mixture plasma. This is probably due to the modification of the wall surface by the preceding plasma process, and it resulted in the difference of surface loss probability in each process condition.

It was reported that the effect of hydrogen into nitrogen plasma on iron contributed to the increase of sticking coefficient on the surface. The decrease of the work function of iron has been observed in the presence of co-adsorbed hydrogen [21]. This decrease of work function may lead to an increase in sticking and hence the chemisorptions at the surface. Moreover, for transition metals with high densities of 3d electrons, adsorption of even small amounts of hydrogen in the presence of a large concentration of vacancies at the surface caused the formation of hydrogen-vacancy surface states. These are acceptor-like levels with large correlation lengths which can assist in the capture of nitrogen species from the gas phase into an adsorbed state [13]. From these reports, as compared with our results on stainless steel, it is significantly agreeable. The surface loss probability of H atom after preceding process after the plasma including H_2 gas was lower than any other processes.

Figure 5.6 indicate the temporal change of surface loss probability of H and N atom in H_2/ N_2 plasma dependence on preceding plasma process H_2/N_2, (a) H_2, (b) N_2 and (c) air. From this result, each loss probability increase after (b) N_2 and (c) air exposure is saturated to the same value after seasoning in 300 s.

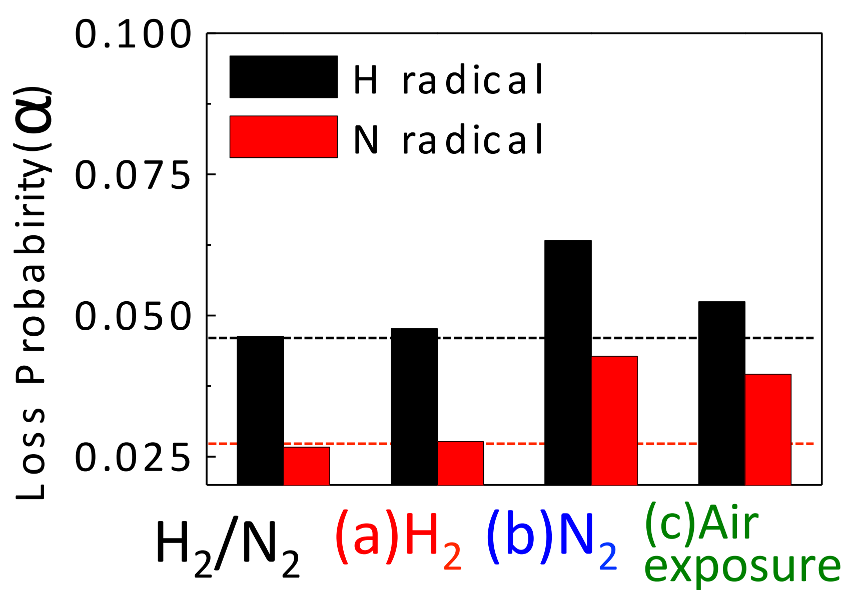

Figure 5.4 Dependence of preceding plasma process H_2/N_2, (a) H_2, (b) N_2 and (c) air exposure on H and N atom surface loss probability in H_2/N_2 mixture plasma.

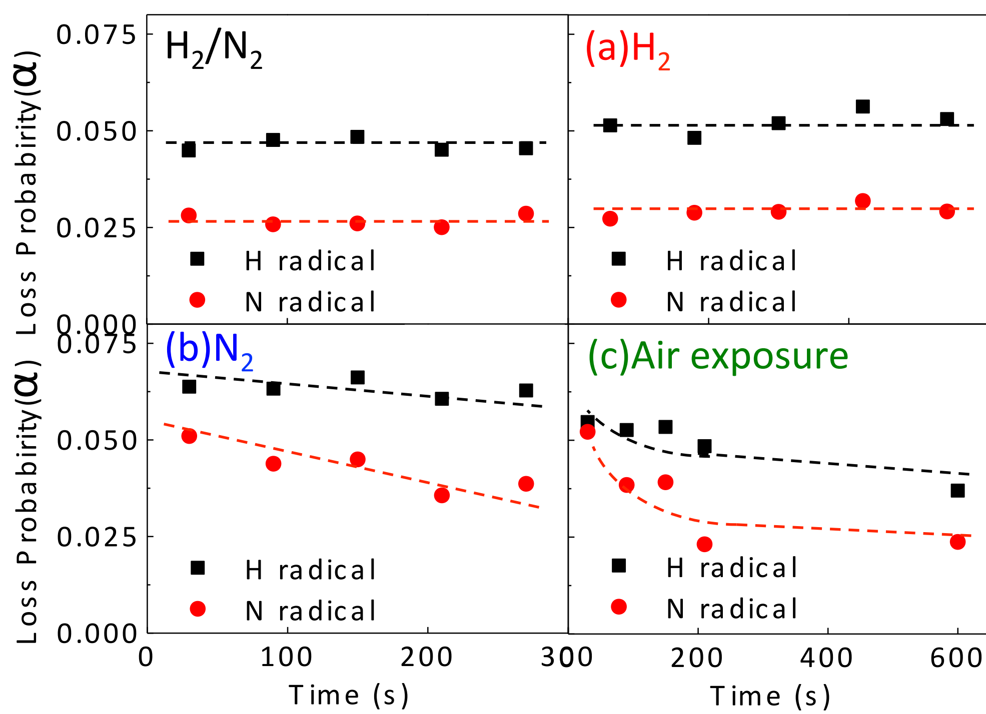

Figure 5.5 Temporal change of surface loss probability of H and N atom in H_2/ N_2 plasma dependence on preceding plasma process H_2/N_2, (a) H_2, (b) N_2 and (c) air.

5.4 Conclusion

I have investigated surface loss probabilities of H, N atoms in the afterglow plasma on different preceding processes such as H_2/N_2 plasma, H_2, N_2 and air exposure employing VUVAS system.

It was confirmed that surface loss probabilities of H, N atoms in H_2/N_2 plasma after (b) N_2 plamsa and (c) air exposure were higher in H_2/N_2 mixture plasma than those in pure H_2 or N_2 plasma with an exception on stainless steel in H_2 plasma.

By understanding of the surface loss probability which is necessary for the precise process control, it is possible to realize more precise interpretation of the process characteristics by internal parameters. Moreover, based on a well-established Plasma Nano-Science including sufficient information about internal parameters, the development for next generation etching process would be accelerated.

5.5 References

[1] H. Nagai, S. Takashima, M. Hiramatsu, M. Hori, and T. Goto, J. Appl. Phys. 91, 2615 (2002).

[2] X. Hua, X. Wang, D. Fuentevilla, G. S. Oehrlein, F. G. Celii, and K. H. R. Kirmse, J. Vac. Sci. Technol. A 21, 1708 (2003).

[3] M. Posseme, T. Chevolleau, T. David, M. Darnon, O. Louveau, and O. Joubert, J. Vac. Sci. Technol. B 25, 1928 (2007).

[4] M. J. Baldwin, G. A. Colliness, M. P. Fewell, S. C. Haydon, S. Kumar, K. T. Short, and J. Tendys, Jpn. J. Appl. Phys. 36, 4941 (1997).

[5] N. Itabashi, K. Kato, M. Magane, S. Naito, T. Goto, A. Matsuda, C. Yamada, and E. Hirota, Jpn. J. Appl. Phys. 29, L505 (1990).

[6] K. Sasaki, K. Usui, H. Furukawa, C. Suzuki, and K. Kadota, Jpn. J. Appl. Phys. 37, 5047 (1998).

[7] Y. Hikosaka, H. Toyoda, and H. Sugai, Jpn. J. Appl. Phys. 32, L690 (1993).

[8] S. Takashima, M. Hori, T. Goto, A. Kono, and K. Yoneda, J. Appl. Phys. 90, 5497 (2001).

[9] Y. Hatanaka and S. Mickramanayaka, Vacuum 35, 894 (1992).

[10] J. P. Booth and N. Sadegi, J. Appl. Phys. 70, 611 (1991).

[11] S. Takashima, M. Hori, T. Goto, A. Kono, M. Ito, and K. Yoneda, Appl. Phys. Lett. 75, 3929 (1999).

[12] M. Hori and T. Goto, Appl. Surf. Sci. 253, 6657 (2007).

[13] B. Gordiets, C. M. Ferreira, M. J. Pinheiro, and A. Ricard, Plasma Sources Sci. Technol. 7, 363 (1998).

[14] P. J. Chantry, J. Appl. Phys. 62, 1141 (1987).

[15] E. A. Mason, and L. Monchick, J. Chem. Phys. 36, 2746 (1962).

[16] R. C. Reid, J. M. Prausnitz, and T. K. Sherwood: The Properties of Gases and

Liquids (McGraw-Hill, New York, 1977).

[17] R. A. Svehla, NASA Tech. report No. R-132, Iewis Research Center, 1962.

[18] H. M. Katsch, A. Tewes, E. Quandt, A. Goehlich, T. Kawetzki, and H. F. Döbele, J. Appl. Phys., 88, 6232 (2000).

[19] J. W. Coburn, and H. F. Winters, J. Appl. Phys. 50, 3189 (1979).

[20] E. Gogolides, P. Vauvert, G. Kokkoris, G. Turban, and A. G. Boudouvis, J. Appl. Phys. 88, 5570 (2000).

[21] S. Bockel, J. Amorim, G. Baravian, A. Ricard, and P. Stratil, Plasma Sources Sci. Technol. 5, 567 (1996).

[22] D. T. Clark, and A. Diks, J. Polym. Sci. Poym. Chem. Ed. 15, 2321 (1977).

[23] S. Takashima, S. Arai, A. Kono, M. Ito, K. Yoneda, M. Hori, and T. Goto, J. Vac. Sci. Technol. A 19 (2001) 599.

[24] O. Jintsugawa, M. Sakuraba, T. Matsuura, and J. Murota, Surf. Interface Anal. 34, 456 (2002).

[25] A. Herrera-Gomez, F. S. Aguirre-Tostado, M. A. Quevedo-Lopez, P. D. Kirsch, M. J. Kim, and R. M. Wallace1, J. Appl. Phys. 104, 103520 (2008).

[26] D. Marton, K .J. Boyd, A. H. Al-Bayati, S. S. Todorov, and J. W. Rabalais, Phys. Rev. Lett. 73, 118 (1994).

[27] K. J. Boyd, D. Marton, S. S. Todorov, A. H. Al-Bayati, J. Kulik, R. A. Zuhr, and J. W. Rabalais, J. Vac. Sci. Technol. A 13, 2110 (1995).

[28] D. E. Weibel , C. Vilani, A. C. Habert, and C.A. Achete, Surf. Coat. Technol. 201, 4190 (2006).).

Chapter 6 Real Time Process Control of Plasma Etching Based on Atom Densities Measurements

6.1 Introduction

Plasma etching technologies are indispensable for manufacturing ultralarge scale integrated (ULSI) circuits by engraving patterns, trenches or holes along the etching masks in the underlying material [1,2]. Recently, ULSI circuits have been rapidly decreasing in size in accordance with Moore's law. As the design rules of ULSI circuits are reduced, etching processes become more complex. Thus, it is important to realize ultraprecise control with few fluctuations on a subnanometer scale. For the precise plasma etching, it is widely known that behaviors of atom densities influenced much on etching feature [3-7]. However, condition of reactor wall surface influences the plasma chemistry in the reactor and it has been a great concern for the precise control of plasma etching processing [8-10]. Particularly, it has become problems that the prior process and/or the exposure the ambient air for the maintenance of reactors could modify the surface condition of the wall considerably and then influence the present etching process indirectly via the wall surface memory [11] Recently, some papers have reported the reactor-wall's surface loss probabilities of species such as molecular atoms [12–14] and atoms [15–19] by using various diagnostic techniques such as absorption spectroscopy and appearance mass spectroscopy. However, many of the details of the interaction of plasma particles, such as ion, atom and neutral with the reactor wall and substrate are not clear because of complexity of the plasma processes.

Based on these backgrounds, one strategy for realizing precise etching process is to control the atom densities directly with monitoring and feedback the results to the processing. In our previous study, Takahashi *et al.* investigate the plasma etching of

low-k organic films by focusing on real-time monitoring of absolute atom densities for many internal parameters, which affect the plasma etching characteristics of low-k organic films [20]. Several researchers have investigated real-time control of plasma processes [21]. Shadmehr *et al.* used optical emission spectroscopy in conjunction with residual gas analysis for fault detection and control of a CHF_3/O_2 plasma [22]. Greve *et al.* demonstrated real-time feedback control of a SiH_4/NH_3 plasma by using quadrupole mass spectrometry [23].

In this chapter, I report an autonomously controlled plasma etching process for the realization of the nm-scale super fine etching process. For the realization of the process fluctuation of the radical density ratio during process has to be control to the ideal value under the fluctuation of a few %. For the first step of the experiment, the changes of absolute densities of H and N atoms in the H_2/N_2 mixture plasma on the modified surface by air exposure was controlled to the intended value, based on the quantitatively measurement by absolute measurements using vacuum ultra-violet absorption spectroscopy (VUVAS). The organic films used in this study were SiLK^{TM}(Dow Chemical), having a good thermal stability (420°C), and good adhesion. Gases of H_2 with a flow rate of 75 sccm and N_2 with a flow rate of 25 sccm were introduced to the chamber through the showerhead as a top electrode. The total gas pressure was kept at 2.0 Pa. A 100-MHz very high frequency (VHF) power of 400 W was supplied to the top electrode, and 2-MHz medium frequency (MF) of 200 W was supplied to the bottom electrode as a substrate bias. This condition is typically used for etching of the low-*k* organic materials. [24,25].

This radical feedback control system is expected to realize not noly nm-scale super fine etching process but also greatly improve wafer-to-wafer or lot-to-lot processing quality, because the feedback control system reduce process variability, and more specifically capability, which is a function of process variability and process accuracy. The feedback control system improves process accuracy utilizing pre- and

post-process measurement, modeling of process and equipment trends, and suggesting subsequent process parameter adjustments (i.e. feedback control). Process variability is generally reduced through preprocess measurements and subsequent process parameter adjustment (i.e. feedforward control). Run-to-run process control (R2R) could address to improve within-wafer and within-die variability. In general, process engineers are unwilling to allow dynamic changes in the process recipe in order to achievements [1]. Furthermore, it is necessary that processes are controlled at real time in order to minimize any fluctuations in etching characteristics to suppress any perturbation such as modification of chamber–wall conditions [2].

6.2 Experimental Details

Samples were prepared by the photolithographic patterning of the line/space (65/65 nm) of a SiO_2 hard mask on an organic film, $SiLK^{TM}$(Dow Chemical), covered by a spin-on coating and cured thermally at 400°C. After etching the hard mask, the photoresist films were covered because no ash removal process was carried out. The patterned sample consisted of stacked structure of a SiO_2(125 nm)/$SiLK^{TM}$(240 nm)/Si. Plasma etching was performed by the capacitively coupled plasma etcher with the real time controller. Schematic diagram of the etch reactor and the setup for measuring the absolute density of H and N atoms near the reactor wall were described elsewhere.[2,27]

The real-time controller changed autonomously the gas flow rates to satisfy the ratio of atom densities to the intended values for well-shaped feature profile. At the beginning, gases of H_2 with a flow rate of 75 sccm and N_2 with a flow rate of 25 sccm as initial values were introduced to the chamber through a showerhead as a top electrode. The total gas pressure was kept at 2.0 Pa. A 100-MHz very high frequency (VHF) power of 400 W was supplied to the top electrode, and 2-MHz medium frequency (MF) of 200 W was supplied to the bottom electrode as a substrate bias. This condition is typically used for etching of the low-*k* organic materials.[26,28] Etching time was set at 10% over of the etched time. The etching profiles of the cross section of the line-and-space pattern were observed using scanning electron microscopy (SEM; Hitachi S-5200).

A compact atom monitoring system consists of a micro-discharge hollow cathode lamp (MHCL), a VUV monochromator and optical component parts such as reflection mirror and MgF_2 windows was equipped the plasma etcher used in this study. Details were described elsewhere. [29-34] For the real-time control, densities of both N and H atoms were simultaneously measured by the two monitors. The atom density

ratio H/(H+N) was calculated at real time from the measured densities of both N and H atoms. Only the gas flow rates were changed by controlling the atom density ratio to maintain a target value, and the rest of process parameters remained a constant. The system controls the atom density ratio H/(H+N) with two-degrees-of-freedom controller; target parameter was the atom density ratio and operation parameter was the gas mixture ratio [35,36]. The details of the control system was described elsewhere [27]. In this experiment, target H/(H+N) atom density ratio was 50%.

Schematic diagram of the etch reactor and the setup for measuring the absolute density of H and N atoms near the reactor wall is indicated in the previous paper [20,26]. A compact atom monitoring system consists of a micro-discharge hollow cathode lamp (MHCL), a VUV monochromator and optical component parts such as reflection mirror and MgF_2 windows [27-31]. The VUV light from MHCL was reflected by the aluminum (Al) mirror with the direction of 45 degrees and passed through the MgF_2 window and was absorbed in the plasma region. The VUV light passed through another MgF_2 window and reflected at Al mirror to a VUV monochromator with a photomultiplier tube. The absorption length was 40 mm. Its configurations in details are shown in elsewhere [32]. The transition lines for the absolute atom density measurement were the Lyman α at 121.6 nm for H atom, and $^4P_{5/2}$-$^4S^o_{3/2}$, $^4P_{3/2}$-$^4S^o_{3/2}$ and $^4P_{1/2}$-$^4S^o_{3/2}$ at 119.96, 120.02 and 120.07 nm for N atoms.[27-31)] To reduce the measurement time, two atom density monitors were used to simultaneously measure the N and H atom densities. The atom density ratio H=(H/N) was calculated from the atom densities measured by these two atom density monitors. By keeping all the process parameters besides the gas mixture ratio constant, the atom density ratio could be controlled by controlling the gas mixture ratio. The target parameter was the atom density ratio and the operation parameter was the gas mixture ratio. The measured value (i.e., the output of the controlled system) was the atom density ratio measured by the

atom monitor. Samples were prepared by the photolithographic patterning of the line/space (65/65 nm) of a SiO_2 hard mask on an organic film. After etching the hard mask, the photoresist films were covered because no ash removal process was carried out. The patterned sample used in this experiment consisted of a SiO_2/SiLK^{TM}/Si stacked structure. The thickness of the hard mask using SiO_2 was 125 nm. A dielectric film of SiLK^{TM} (Dow Chemicals) resin with a thickness of 240 nm was covered using a spin coating technique on a bare silicon substrate and thermally cured at 400°C to provide a high glass transition temperature, good mechanical properties at processing temperatures, and resistance to the processing chemicals used. The SiLK resin includes crosslinked polyphenylenes obtained by the reaction of polyfunctional cyclopentadienone- and acetylene- containing materials. [33,34] Polyphenylenes and a solution of a partially polymerized oligomer with an average molecular weight of less than 10,000 and a polymer concentration ranging from 5 to 20 wt % in a high-purity organic solvent of either c-butyrolactone with cyclohexanone or c-butyrolactone with mesitylene was used [35,36]. Etching time was set at 10% of the overetched time estimated from etch rate. The etching profiles of the cross section of the line-and-space pattern were observed using scanning electron microscopy (SEM; Hitachi S-5200).

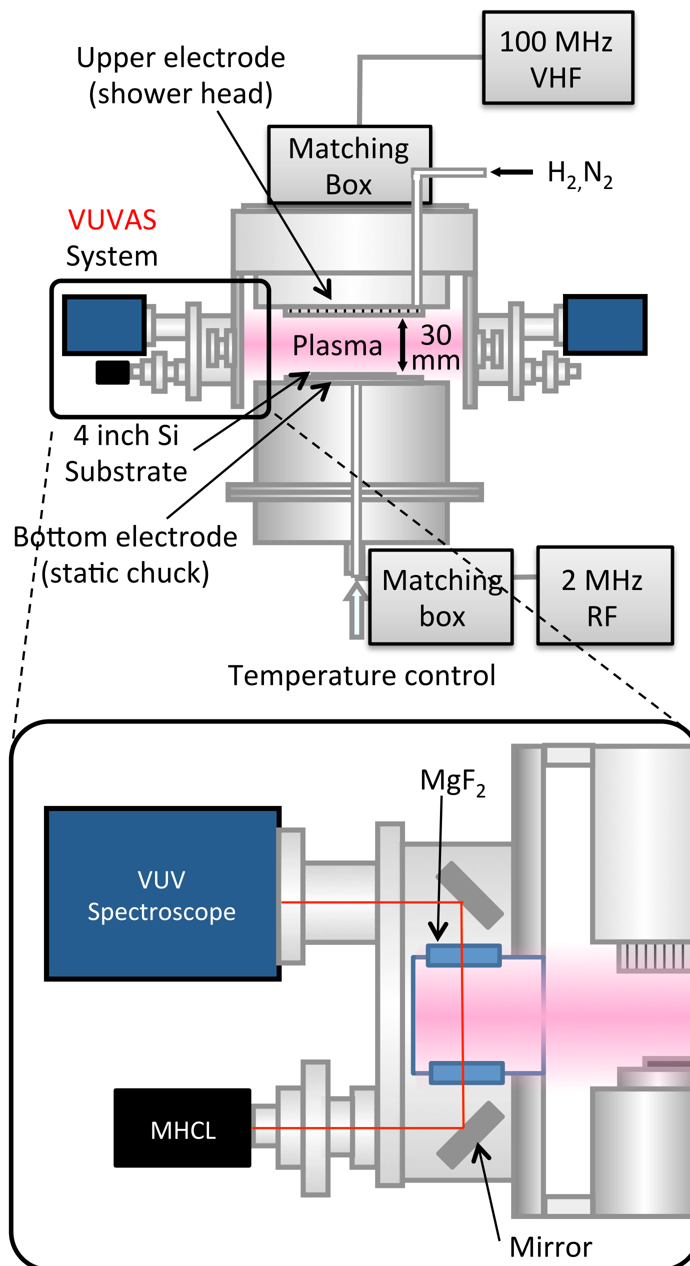

Figure 6.1 Schematics diagram of the experimental apparatus used for measuring the density of hydrogen and nitrogen atoms near the reactor wall employing a VUVAS system.

6.3 Results and Discussion

6.3.1 Autonomous Control System Setup

Figure 6.2 shows the operating system that enables autonomous control of the plasma etching process. Two-degrees-of-freedom control [37,38] was used in the system to control the atom density ratio H/(H+N). This system has feedforward and feedback compensators. The feedforward compensator enhances the target value response of the atom density ratio H/(H+N). The proportional–integral–derivative (PID) feedback compensator of this system corrects deviations between the target and measured values (including disturbance and white noise). The etching time is generally about three-five minutes, which is relatively short. Consequently, it is necessary to control the system in as short a time as possible.

In Fig. 6.2, r is the target value of the atom density ratio H/(H+N) and u is the operational value of the gas flow rate ratio $H_2/(N_2+H_2)$. Moreover, $f_m(u)$ is the function of the controlled object and $f_m(u)$ is the model for the controlled object and indicates the correlation obtained between the atom density ratio H/(H+N) and the gas flow ratio $H_2/(N_2+H_2)$. $f_m(u)$ is constructed by measuring the atom density ratio using the atom monitors installed on the plasma equipment while varying the gas flow rate ratio $H_2/(H_2+N_2)$. When the model of the controlled object changes owing to disturbances and other factors such as electrode degradation due to secular distortion, $f_m(u)$ is updated based on the data accumulated by the system.

Moreover, y indicates the measured atom density ratio H/(H+N). It includes the values of d and w; y and y_b are respectively given by $y=y_b+w$ and $y=y_a+d$. d represents disturbances such as aging variation and contamination of the

chamber and w is the white noise such as measurement errors. Here, y_a expresses the atom density ratio H/(H+N) after subtracting d and w. It is difficult to completely eliminate d and w during measurements and so a state is defined using their initial values.

By determining the target value of r and inputting it to the controller, the gas flow rate ratio $H_2/(H_2+N_2)$ corresponding to r can be determined from the inverse $f_m^{-1}(u)$ of the output function $f_m(u)$. This value is defined as u_1, and the difference in y and r gives the output gas flow rate ratio $H_2/(H_2+N_2)$ from the PID controller. This value is defined as u_2. The final gas flow rate ratio of $H_2/(H_2+N_2)$ is determined by summing the two operational values ($u=u_1+u_2$). This value is output from the main server to the programmable logic controller (PLC) as the setting value of the flow rate ratio of the two gases.

A previous study [20] found that the atom density ratio is not simply proportional to the gas flow rate ratio. It is not easy to optimize only one gain in every range because the controlled system is nonlinear. Tuning the control gain is simplified by selecting the optimum correction gain for the target value r. The parameters K_1; K_2; . . . ; K_n are the correction gains of PID controller. The gain K_n corresponding to r is set and it is switched depending on the range of r by the switch SW. By switching the gain of K_n in the range of r, it is not necessary to adjust the system for the full range of the gas flow rate ratio (i.e., 0–100%). This system has the advantage that the model can be changed by readjusting the gain over a limited range.

The elements of the etching gas in the plasma are deposited on the chamber wall and the electrode during the etching process. If this deposit peels off from the chamber wall and the electrode, particles form in the chamber. To prevent this, the chamber is cleaned. The environment in the chamber generally changes after cleaning. This affects the control system as turbulence. In this

study, the control model is always compared with the controlled system. When the error between the control model and the controlled system increases, the control model and the correction gain are retuned.

In the previous experiment, Yamamoto et al. Indicated that boing amount could be minimized under the condition of H/(H+N) = 0.5 to 0.6 [24]. Thus, target H/(H+N) atom density ratio was set to 50% in this experiment.

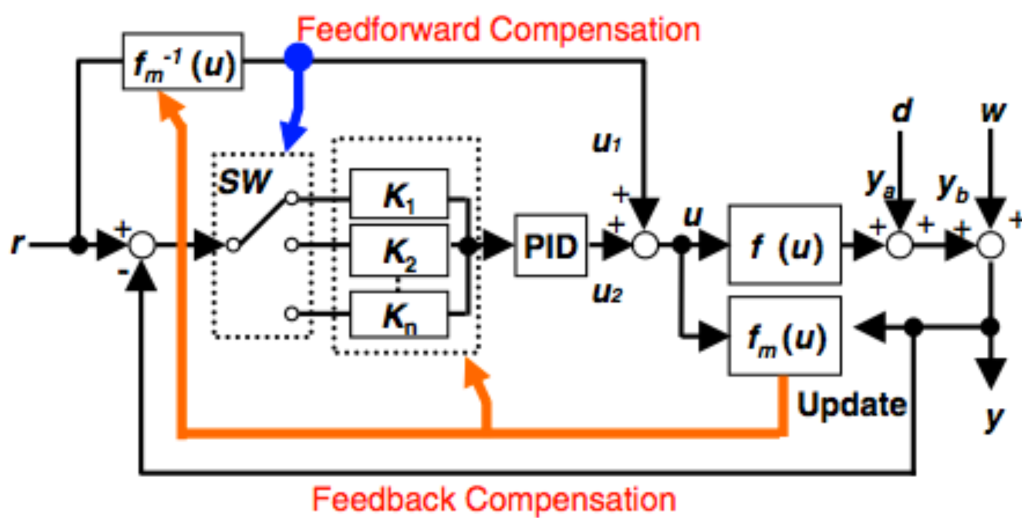

Figure 6.2 Block diagram of control system for atom density ratio H/(H+N).

6.3.2 Properties of Organic Low Dielectric Constant Film [3]

In the etching parts of this study, blanket films of organic low-*k* material, SiLK, on Si substrate, which has been developed by The Dow Chemical Company, were etched. SiLK resin is a solution of partially polymerized oligomer in high-purity organic solvents. The number-average molecular weight of the oligomer is less than 10,000. Depending on the specific formulation, the polymer concentration ranges from 5 to 20 wt.-% in a solvent mixture of either c-butyrolactone with cyclohexanone or c-butyrolactone with mesitylene.

Thin films are prepared by conventional spin-coating and thermal curing. The solutions have viscosity of 5 to 80 cSt at room temperature, yielding films in the range of 0.2 to 2.0 μm. These solutions have handling characteristics very similar to modern photoresist products. The polymer molecular weight and solution concentration were tuned to enable precise and convenient deposition by spin-coating, a technique universally used by the industry for the deposition of photoresist materials.

After deposition on the wafer, the polymer is thermally cured to an insoluble film that has a high T_g, has good mechanical properties at process temperatures, and is resistant to process chemicals. The properties of SiLK are summarized in Table 6.2.

The approach that was commercially implemented as SiLK dielectric involves the synthesis of crosslinked polyphenylenes by the reaction of polyfunctional cyclopentadienone- and acetylene-containing materials (see Fig. 6.3) [6]. Polyphenylenes are known to have excellent thermal stability [7]. Typically, however, polyphenylenes need to be substantially substituted in order to achieve solubility and thus processability. By preparing the polyphenylenes from cyclopentadienone- and acetylene-containing monomers, the initial oligomers formed are soluble without undue substitution and can thus be processed.

Further reaction on wafer converts the oligomers to crosslinked polymers that

have properties suitable for use as interlayer dielectrics. The cyclopentadienones react with the acetylenes in a 4+2 cycloaddition reaction followed by the expulsion of CO to form a new aromatic ring. The multifunctional nature of the monomers leads to crosslinked polyphenylene systems after full cure. In April 2000, IBM reported the complete integration of SiLK dielectric and copper wiring, and announced its intent to commercially fabricated integrated circuits using SiLK resin [8)].

Table 6.1. Summary of SiLK dielectric properties

Property	***Value***
Dielectric constant	2.65
Voltage breakdown	4V/cm
Leakage current at 1MV/cm	0.33 nA/cm^2
Refractive index at 632.8 nm	1.63
Moisture uptake at 20℃, 80%RH	0.24 %
Thermal stability	> 425℃
Weight loss at 450℃	0.7 wt.-%/h
Thermal conductivity at 25℃	0.19 W/mK
Glass transition	> 490℃
Young’s modulus	2.45 GPa
Strength	90 MPa
Ultimate strain	11.5 %
Hardness	0.38 GPa
Toughness	0.62 MPa m$^{1/2}$
Residual stress at RT	56 MPa
Coefficient of Thermal Expansion (CTE)	66 ppm/℃

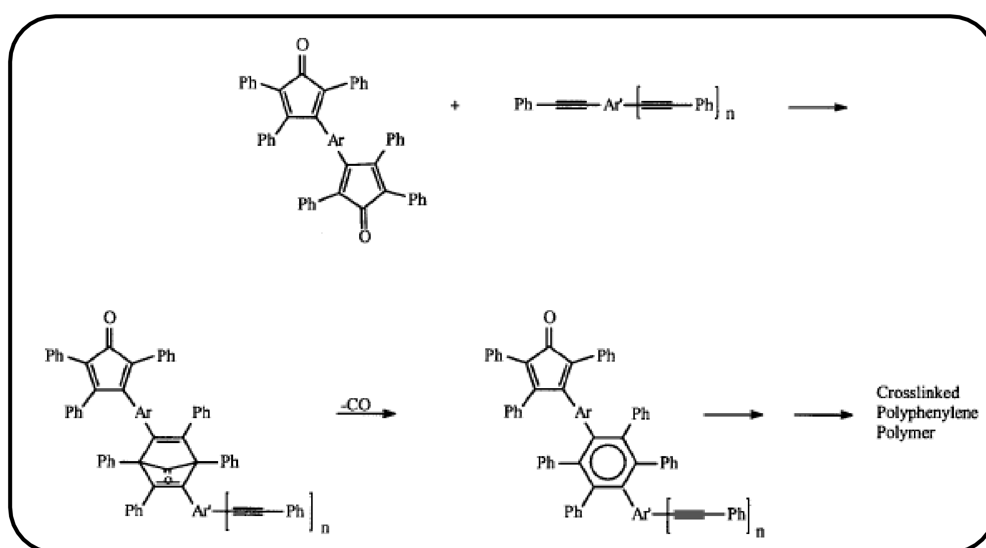

Figure 6.3 Formation of crosslinked polyphenylene by the reaction of polyfunctional cyclopentadienone- and acetylene-substituted monomers.

6.3.3 Influence of Air Exposure on Atom Density

As mentioned previously, process parameters run frequently into unintentional fluctuation. To suppress the fluctuation, a real-time process control is supposed to be realized the precise control in plasma etching. Exampled as a fluctuated situation, we carried out experiments when the inner wall condition was changed after conditions air exposure. This introduces intentionally temporal variations of H and N atom densities of H_2/N_2 plasma, because the reactor wall was modified in their atom loss probabilities by exposing air exposure after the O_2 plasma as cleaning for 3 min after H_2/N_2 plasma as seasoning for 3 min.

Figure 6.4 (a) and (b) shows temporal changes for H and N atom densities respectively in the H_2/N_2 plasma. After air exposure, the H atom density was increased to be 1.4 $\times 10^{11}$ cm^{-3} just after the plasma ignition, decreased during early 60 s, and stabilized to reach a constant of 1.1×10^{11} cm^{-3}. The N atom density was also increased to be 3.5×10^{11} cm^{-3} just after plasma ignition, and remained higher value even after 120 s.

Figure 6.5 shows temporal changes for the atom density ratio, N/(H+N) calculated from the atom densities. Atom density ratio 0.31 just after the plasma ignition, and stabilized to be 0.24 after fluctuation during early process for 60 s. Based on previous study, both the etching rate and pattern profile of low-*k* organics would be modified in the H_2/N_2 plasma etching processing [28,37,38]. In this case, the atom density ratio of H/(H+N) is controlled in the area of 0.5±3.8 after 70 seconds with the autonomous control. This stabilizing duration have to be minimizing by optimization of the autonomous feed back control system.

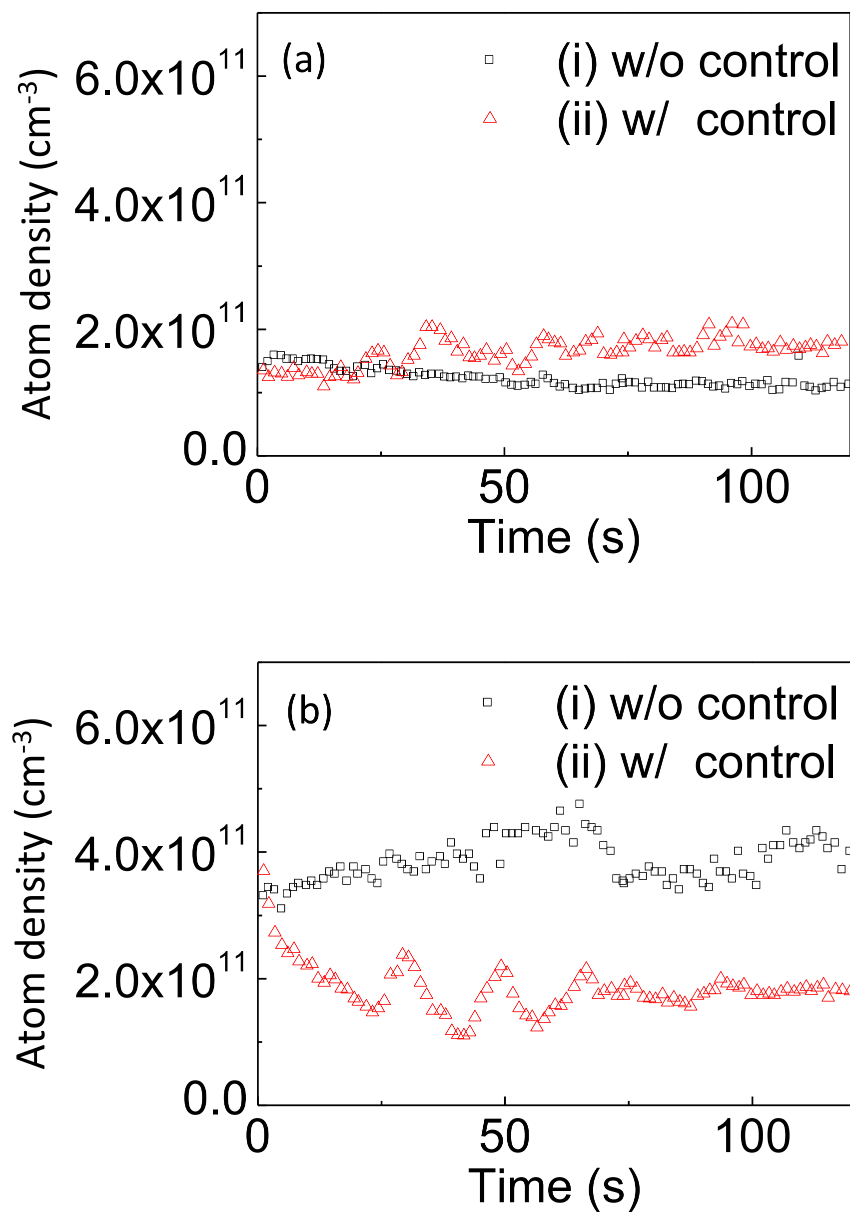

Figure 6.4 Temporal changes for atom density of (a) Hydrogen and (b) Nitrogen, in the H_2/N_2 plasma subsequently after air exposure (i) without and (ii) with the autonomous control.

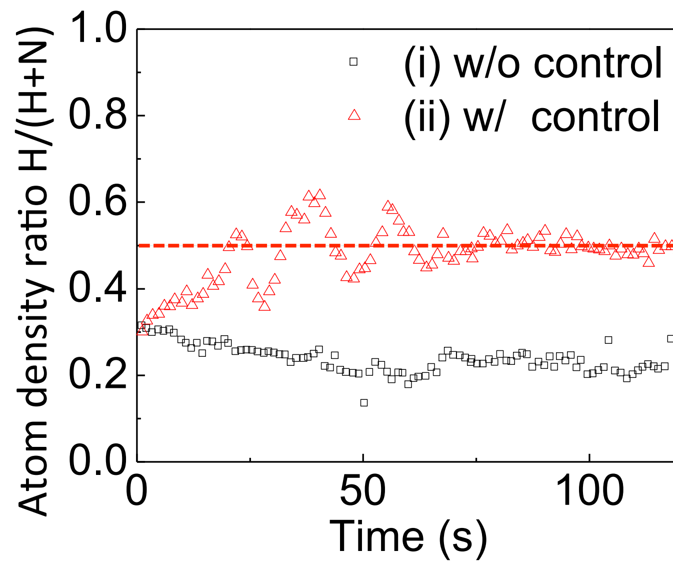

Figure 6.5 Temporal change for atom density ratio under autonomous control.

6.3.4 Evaluation with Optical Emission Spectroscopy (OES)

On the other hand, conventionally optical emission spectroscopy (OES) was failed to monitor the change of atom densities for the feature profile control. During the H_2/N_2 plasma processes, emission intensities were measured for lines at 501.7 and 857.7 nm of H_2, and at 674.91, 670.02, 372.42, 593.64, 761.87 and 790.76 nm of N_2. Figure 6.6 shows temporal changes of the emission intensities of representative lines at 501.7 nm for (a) H_2 lines, and at 674.9 nm for (b) N_2 lines, during the processes without (i) and with the autonomous control (ii).

In the visible ranges, no lines could be distinguished enough in atoms and molecules. Notably no parameter related the ratio of atom densities was obtained by the OES, and the temporal changes of emission intensities were not corresponded with those of the atom densities measured by the VUVAS, because the intensities in the OES do not represent the atom densities. Thus the ratio of atom densities could not permit to suppress the fluctuation in the H_2/N_2 plasma subsequently after air exposure.

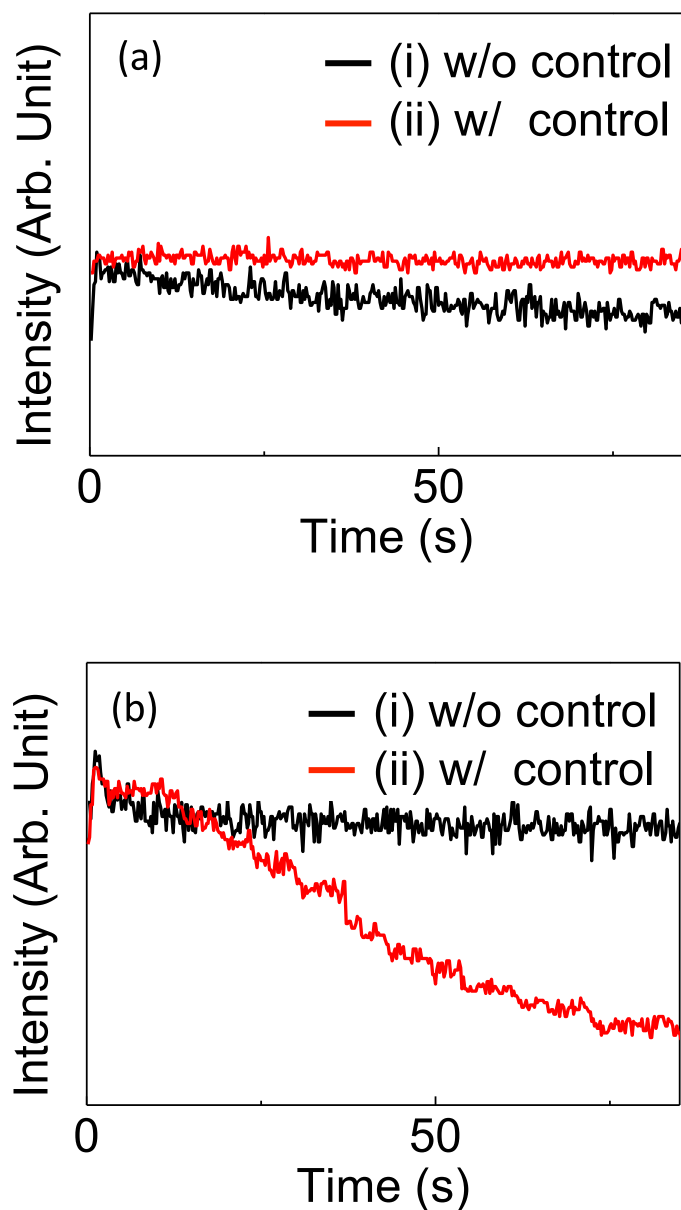

Figure 6.6 OES intensity of (a) H_2 emission (at 501.7 nm) (b) N_2 emission (at 674.9 nm) in the H_2/N_2 plasma subsequently after air exposure (i) without and (ii) with the autonomous control.

6.3.5 Impact of Atom Density Control on Etching Feature

The amount of bowing is defined as the difference between the width at the highest bowing position or the most tapered position ‘‘B’’ and the width at the line at the top ‘‘A’’, as shown in Figure 6.7. (Note: To meet the requirements of the etch process, it is better to reduce the size of the trench bottom, B. Hence, if B is less than A, I always regard the data as the taper profile.) The amount of bowing slightly increased with increasing the substrate temperature. This change is important from the viewpoint of controlling the shape of sidewall. Etched profiles have been investigated on the basis of the average ratio of H and N atom densities during process.

Black dot in the Figure 6.7 shows the amount of bowing at the sidewall of a in H_2/N_2 plasma after each seasoning, red dot indicate bowing amount in H_2/N_2 plasma after (ii) air exposure, and blue dot indicate bowing amount in H_2/N_2 plasma under atom control after (ii) air exposure.

Figure 6.8 shows cross-sectional SEM images of the etch profile of the 65nm line-and-space pattern of the organic film. The bowing amount was -13.5 nm at the reactor condition after (ii) air exposure, and the value decreased to -5 nm under atom control. These results show that the etching feature can be controlled with the atom density ratio, without thinking about the reactor wall condition.

Unfortunately the other internal parameter such as electron density, ion bombardment could not be measured for these experiment. However, pressure and self-bias voltage (V_{dc}) at under electrode were constant at 2.0 Pa and 480 V. These results indicates that etching shape is deeply depending on the radical density and the feedback control based on radical density ratio has the potential to realize a super fine etching with nm-size fluctuation without considering pre-plasma processes.

I intend to improve the accuracy and speed in controlling the atom density ratio in a future study. In actual etching, atom density changes temporary affected not only by

the reactor wall initial condition but also etching product and change the reactor wall condition by the deposition of etching product. However, in this study, I have demonstrated the control of the atom density in real time by employing an autonomous control system and minimized the etching feature fluctuation. These results demonstrate a new concept for realizing high precision control of plasma processing, which will be required for precise etching in the near future.

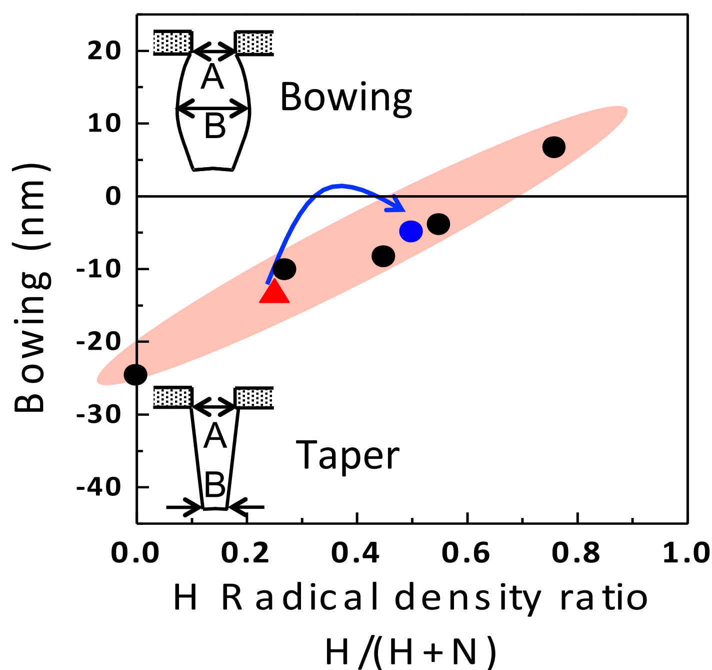

Figure 6.7 SEM image of etched L&S patterned sample (red dot) without atom control and (blue dot) with atom autonomous control.

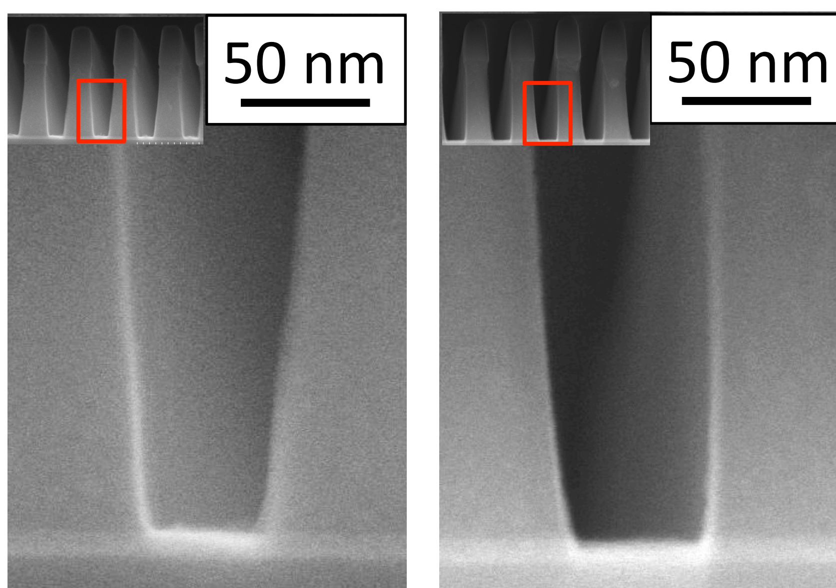

Figure 6.8 SEM images of the L&S patterned sample etched (i) without and (ii) with the autonomous control in the chamber after air exposure.

6.4 Conclusion

The atom densities subsequently after a different kind of plasmas in the H_2/N_2 mixture plasmas after air exposure were higher than those in the H_2/N_2 plasma after seasoning. It is assumed that the temporal behavior can be interpreted as etched products or process gases were adsorbed on inner wall surface during the previous process, and then those species were desorbed from the wall into bulk plasmas. Especially, the ratio continued to be kept low for a long time after the air exposure. It may suggest water vapor could affect much and/or modify some products deposited on the inner wall. In this study, I have demonstrated control of atom density in real time by employing an autonomous control system. The control minimized influence of the reactor wall condition to the etching feature. These results demonstrate a new concept for realizing high precision control of plasma processing, which will be required in the near future.

6.5 References

[1] H. Abe, M. Yoneda, and N. Fujiwara: Jpn. J. Appl. Phys. **47** (2008) 1435.

[2] V. M. Donnelly and A. Kornblit: J. Vac. Sci. Technol. A **31** (2013) 050825.

[3] M. Sekine, Appl. Surf. Sci. **192** (2002) 270.

[4] G. S. Oehrlein, R. J. Phaneuf, and D. B. Graves: J. Vac. Sci. Technol. B **29** (2011) 010801.

[5] M. Fukasawa, T. Tatsumi, T. Hasegawa, S. Hirano, K. Miyata, and S. Kadomura: Proc. on Dry Process Symposium (Tokyo, 1999) p. 221.

[6] Y. Morikawa, S. Yasunami, W. Chen, T. Hayashi, and T. Uchida: J. Vac. Sci. Technol. **A** 19 (2001) 1747.

[7] Y. Morikawa, T. Hayashi, and T. Uchida: Jpn. J. Appl. Phys. **42** (2003) 1441.

[8] G. Cunge, M. Kogelschatz, and N. Sadeghi: Plasma Sources Sci. Technol. **13** (2004) 522.

[9] M. Schaepkens, R. C. M. Bosch, T. E. F. M. Standaert, G. S. Oehrlein, and J. M. Cook: J. Vac. Sci. Technol. A **16** (1998) 2099.

[10] T. W. Kim and E. S. Aydil: J. Electrochem. Soc. **150** (2003) G418.

[11] A. Agarwal and M. J. Kushner, J. Vac. Sci. Technol. A **26** (2008) 498.

[12] N. Itabashi, K. Kato, M. Magane, S. Naito, T. Goto, A. Matsuda, C. Yamada, and E. Hirota: Jpn. J. Appl. Phys. **29** (1990) L505.

[13] Y. Hikosaka, H. Toyoda, and H. Sugai: Jpn. J. Appl. Phys. **32** (1993) L690.

[14] K. Sasaki, K. Usui, H. Furukawa, C. Suzuki, and K. Kadota: Jpn. J. Appl. Phys. **37** (1998) 5047.

[15] J. P. Booth and N. Sadegi: J. Appl. Phys. **70** (1991) 611.

[16] Y. Hatanaka and S. Mickramanayaka: Vacuum **35** (1992) 894. [in Japanese]

[17] S. Takashima, M. Hori, T. Goto, A. Kono, and K. Yoneda: J. Appl. Phys. **90** (2001) 5497.

[18] M. Hori and T. Goto: Appl. Surf. Sci. **253** (2007) 6657.

[19] G. A. Curley, L. Gatilova, S. Guilet, S. Bouchoule, G. S. Gogna, N. Sirse, S. Karkari, and J. P. Booth: J. Vac. Sci. Technol. A **28** (2010) 360.

[20] S. Takahashi, R. Kawauchi, S. Takashima, S. Den, T. Katagiri, H. Kano, T. Ohta, M. Ito, T. Suzuki, K. Takeda, and M. Hori: Jpn. J. Appl. Phys. **51** (2012) 076502.

[21] T. F. Edgar, S. W. Butler, W. J. Campbell, C. Pfeiffer, C. Bode, S. B. Hwang, K. S. Balakrishnan, and J. Hahn: Automatica **36** (2000) 1567.

[22] R. Shadmehr, A. Angell, P. B. Chou, G. S. Oehrlein, and R. S. Jaffe: J. Electrochem. Soc. **139** (1992) 907.

[23] D. W. Greve, T. J. Knight, X. Cheng, B. H. Krogh, and M. A. Gibson: J. Vac. Sci. Technol. B **14** (1996) 489.

[24] H. Yamamoto, H. Kuroda, M. Ito, T. Ohta, K. Takeda, K. Ishikawa, H. Kondo, M. Sekine, and M. Hori: Jpn. J. Appl. Phys. **51** (2012) 016202.

[25] T. Suzuki, K. Ishikawa, K. Takeda, H. Kondo, M. Sekine, and M. Hori: Jpn. J. Appl. Phys. **52** (2013) 120203.

[26] T. Suzuki, K. Takeda, H. Kondo, K. Ishikawa, M. Sekine, and M. Hori: Jpn. J. Appl. Phys. **Submitted** (2013).

[27] S. Takashima, M. Hori, T. Goto, A. Kono, M. Ito, and K. Yoneda: Appl. Phys. Lett. **20** (1999) 3929.

[28] K. Murata, Y. Mizutani, E. Iwasaka, S. Takashima, M. Hori, T. Goto, S. Samukawa, and T. Tsukada: Jpn. J. Appl. Phys. **40** (2001) L4.

[29] S. Takashima, M. Hori, T. Goto, and K. Yoneda: J. Appl. Phys. **89** (2001) 4727.

[30] S. Takashima, S. Arai, M. Hori, T. Goto, A. Kono, M. Ito, and K. Yoneda: J. Vac. Sci. Technol. A **19** (2001) 599.

[31] H. Nagai, M. Hiramatsu, M. Hori, and T. Goto: Rev. Sci. Instrum. **74** (2003) 3453.

[32] S. Takahashi, R. Kawauchi, S. Takashima, S. Den, T. Katagiri, H. Kano, T. Ohta, M. Ito, T. Suzuki, K. Takeda, and M. Hori: Jpn. J. Appl. Phys. **51** (2012) 076502.

[33] S. J. Martin, J. P. Godschalx, M. E. Mills, E. O. Shaffer, II, and P. H. Townsend: Adv. Mater. **12** (2000) 1769.

[34] J. P. Godschalx, D. R. Romer, Y. H. So, Z. Lysenko, M. E. Mills, G. R. Buske, P. H. Townsend, III, D. W. Smith, Jr., S. J. Martin, and R. A. DeVries: US Patent 5965679 (1999).

[35] M. Kreyenschmidt, F. Uckert, and K. Muellen: Macromolecules **28** (1995) 4577.

[36] R. D. Goldblatt, B. Agarwala, M. B. Anand, E. P. Barth, G. A. Biery, Z. G. Chen, S. Cohen, J. B. Connolly, A. Cowley, T. Dalton, S. K. Das, C. R. Davis, A. Deutsch, C. DeWan, D. C. Edelstein, P. A. Emmi, C. G. Faltermeier, J. A. Fitzsimmons, J. Hedrick, J. E. Heidenreich, C.-K. Hu, J. P. Hummel, P. Jones, E. Kaltalioglu, B. E. Kastenmeier, M. Krishnan, W. F. Landers, E. Liniger, J. Liu, N. E. Lustig, S. Malhotra, D. K. Manger, V. McGahay, R. Mih, H. A. Nye, S. Purushothaman, H. A. Rathore, S.-C. Seo, T. M. Shaw, A. H. Simon, T. A. Spooner, M. Stetter, R. A. Wachnik, and J. G. Ryan: Proc. Int. Interconnect Technology Conf., 2000, p. 261.

[37] I. M. Horowitz: Synthesis of Feedback Systems (Academic Press, New York, 1963).

[38] N. Suda: PID Seigyo (PID Control) (Asakura, Tokyo, 1992) p. 69 [in Japanese].

[39] H. Nagai, S. Takashima, M. Hiramatsu, M. Hori, and T. Goto: J. Appl. Phys. **91** (2002) 2615.

[40] H. Nagai, M. Hiramatsu, M. Hori, and T. Goto: J. Appl. Phys. **94** (2003) 1362.

Chapter 7 Conclusions and Future Works

7.1 Conclusions of Present Research

Highly precise process control technologies based on the advanced plasma science are indispensible for the fabrication of microelectronics devices which are improved with depending on the shrinkage of dimension and the high integration. The driving force for the rapid development of plasma processing over the past 30 years has been seen in the microelectronics industry such as display and the fabrication of silicon integrated circuits (ICs). Especially, the deposition and etching processes are important necessary keys for advancing the technological developments. Sophisticated and innovative developments have been also required for the application to flexible electronics and the scaling down of its devices.

In Chapter 1, the necessity of plasma processing in the fabrication of microelectronics and attractive interest on the flexible electronics and need of sophisticated deposition and etching technologies for LSIs manufacturing were introduced. Moreover, for the first initiative innovation of etching process development, new approach for next generation nano-etching process was proposed to overcome the problem induced by conventional process.

In Chapter 2, the diagnostic techniques for sophisticatedly evaluating the plasma were introduced and the principle of XPS for analysis of surface reaction was described. VUVAS, OES were used as the measurement tools. XPS, SEM, TEM were used as the measurement methods for the properties of films deposited and etched.

In Chapter 3, the fabrication of 10-nm-scale organic rods covered with Pt nanoparticles on the sidewalls was demonstrated. Supercritical chemical fluid-deposited Pt particles were deposited and they were deposited on the sidewall during etching, which inhibit the spontaneous chemical etching reactions of H atoms with organics. The

Pt nanoparticles prevented lateral etching within a thickness of less than 1 nm. Accordingly, precise shape control was achieved by this approach of the sidewall protective effect with the Pt nanoparticle coverage. This etching process changed the dielectric organic rods to conductive. It was confirmed that the nano-rods sonwed field emission properties. It is noteworthy that the super-fine plasma etching of organic materials is a suitable fabrication process at low temperatures for flexible materials.

In Chapter 4, temporal changes of absolute densities of H and N atoms in the H_2/N_2 plasma after several plasma exposures in the reactor were clarified. The densities of both H and N atoms in the H_2/N_2 plasma just after O_2 plasma were significantly influenced by the reactor wall surface. The N atom density increased 290% and the H atom density increased 70% compared to the stable value after the seasoning process of O_2 plasma due to the interaction between the plasma and the reactor wall surface. Dramatic changes in atom densities indicate that the chemical modifications such as oxidation and nitridation of reactor wall surface affected the surface loss of atom species. As the results, it was revealed that the reactor-wall conditions have the memory effect which affected the temporal behavior of atom densities. The quantitative measurements of absolute atom density revealed the correlations the plasma condition with the surface condition of reactor wall. Thus the control of the wall surface condition was crucially important in achievement of stabilizing in the atom densities. In establishing highly reliable plasma processes, the interactions between the surface and the plasma in the material processing need to understand throughout determining mechanisms. In addition, the real time stabilization process of atoms on the basis of the real time monitoring of atom densities hopes to enable steady controls in the absolute atom densities and their relative ratio for realizing the high performance of plasma processing.

In Chapter 5, I have investigated surface loss probabilities of H, N atoms in the afterglow plasma on different preceding processes such as H_2/N_2 plasma, H_2, N_2 and air

exposure employing VUVAS system. It was confirmed that surface loss probabilities of H, N atoms in H_2/N_2 plasma after N_2 plamsa and air exposure were higher in H_2/N_2 mixture plasma than those in pure H_2 or N_2 plasma with an exception on stainless steel in H_2 plasma. By understanding of the surface loss probability necessary for the precise process control, it is possible to realize more precise interpretation of the process characteristics by internal parameters. Moreover, based on a well-established Plasma Nano-Science including sufficient information about internal parameters, the development for next generation etching process would be accelerated.

In Chapter 6, the atom densities subsequently after a different kind of plasmas in the H_2/N_2 mixture plasmas after air exposure were higher than those in the H_2/N_2 plasma after seasoning. It is assumed that the temporal behavior can be interpreted as etched products or process gases were adsorbed on inner wall surface during the previous process, and then those species were desorbed from the wall into bulk plasmas. Especially, the atoms density ratio continued to be kept low for a long time after the (i) air exposure. It may suggest water vapor could affect much and/or modify some products deposited on the inner wall. I have demonstrated control of atom density in real time by employing an autonomous control system. The control minimized influence of the reactor wall condition to the etching feature. These results demonstrate a new concept for realizing high precision control of plasma processing, which will be required in the near future.

This research was pursued the development of advance plasma processing for etching in a scientific and technological view. Etching characteristics of organic materials were investigated employing H_2/N_2 gas chemistries in CCP discharges. Moreover, as an initiative innovation for the development of plasma processing technologies, precision and versatile plasma process was first proposed on the basis of Plasma Nano-Science for next generation technological progress. The autonomous feedback control etching based on H and N atoms was successfully demonstrated.

Besides those, plasma-surface interaction could be considered and discussed more deeply by investigating surface loss probabilities of H and N atom on various wall materials.

Consequently, advanced plasma processing for precise and versatile etching and deposition developments could be performed by controlling effective hydrogen atoms, which influencing film formation in deposition process at low temperature and etching characteristics of organic materials for flexible material-based applications.

7.2 Future Research Directions

In this research, the etch performance for organic films could be well interpreted by internal parameters such as ion flux and H/(H+N) atom flux ratio in H_2/N_2 plasma. High performance of autonomous feedback control plasma process was also demonstrated. As a future work, it is necessary to collect sufficient information as a function of a variety of autonomous feedback plasma process conditions constantly. Moreover, although the author have mainly considered H, N atoms to interpret the etching characteristics, actually other internal parameters such as the energies of species, the temperature and surface reaction coefficient have to be considered for the sophisticated interpretation with reproducibility. In addition, many of these internal parameters may be difficult to be associated and implemented but their results would allow for a greater validation to the development of nano-scaled etching process, as well as for overcoming the limitation of the technological advancement. Beside only application to etching process, the development by Plasma Nano-Science could be expanded to other plasma based process technologies such as the deposition, ashing and surface modification. In order to apply and improve the autonomous feedback control, it is necessary to develop a well-established autonomous feedback control program, also.

In near future, the establishment of Plasma Nano-Science with spatio-temporal control of the plasma would expect the acceleration of development for deposition as well as etching processes.

Acknowledgements

The present research has been performed in Prof. Hori and Prof. Sekine Laboratory, Department of Electrical Engineering and Computer Science, Nagoya University. The research results presented in this dissertation couldn't have been obtained without the support of the following people whom I wish to appreciate.

First and foremost, I would like to express my sincere appreciation to the research supervisor, Prof. Masaru Hori, Department of Electrical Engineering and Computer Science, Nagoya University, for having given me the opportunity to pursue a Ph.D in Japan. His guidance, valuable advices, and encouragements allowed me to progress rapidly in my understanding of this research. I also would like to thank my co-superviser, Prof. Makoto Sekine, Plasma Nanotechnology Research Center, Nagoya University for providing his wealth of experience and wonderful discussions. At same time, I wish to express my sincere gratitude to the vice-adviser, Prof. Hirotaka Toyoda, Department of Electrical Engineering and Computer Science, Nagoya University, for his valuable suggestions and discussions in progressing this research. I also thank to the vice-adviser, Prof. Kazuo Shiokawa, Solar-Terrestrial Environment Laboratory, Nagoya University, for giving the big motivation for the passionate research. I also thank to the vice-adviser, Prof. Keiji Nakamura, Department of Electrical Engineering and Computer Science, Chubu University, for his valuable suggestions and discussions in progressing this research.

I have warm thanks to Prof. Yuichi Setsuhara, Joining and Welding Research Institute, Osaka University, and Prof. Masaharu Shiratani, Department of Electronics, Graduate School of Information Science and Electrical Engineering, Kyushu University, for collaborating and giving regular and valuable advices for the project of Core Research for Evolutional Science Technology, Japan Science and Technology Agency. To whom it concerns with Japan Society for the Promotion of Science International

Training Program, I am heartily grateful for having given me unforgettable opportunity to broaden my view for world-wide research area and. To Prof. Han, the director of Center for Advanced Plasma Surface Technology in Sungkyunkwan University, Korea. I am deeply indebted to you for teaching me during the ITP program. I am also grateful to the entire staff in Hori and Sekine's Lab., especially Prof. Kenji Ishikawa, Associate Prof. Hiroki Kondo, Assistant Prof. Keigo Takeda, and Dr. Arkadiusz Malinowski for their fruitful discussion and valuable comments. I'd like to acknowledge Dr. Shoji Den, Dr. Koji Yamakawa and Dr, Eiji Takahashi, in Katagiri Engineering Co., Ltd. for constructing and modifying the experimental equipments. A big thanks to my colleagues in Hori and Sekine's Lab, Dr. Shang Chen, Dr. Takuya Takeuchi, Dr. Yudai Miyawaki, Dr. Yuske Abe, Mr. Hironao Shimoeda, Mr. Sho Kawahima, Mr. Tokushige Kino, and Mr. Yuske Kondo, for giving the big pleasure in life and creating a most enjoyable work atmosphere. I also appreciate the enough secretarial supports to Ms. Tomoko Yokoi, Ms. Azusa Ohta, Ms. Megumi Oshigane, and Ms. Rie Nozaki for helping to concentrate on the research without any problem of administrative task.

Finally, I'd like to dedicate this thesis to my family and my future wife, Ayami Mizutani, who have become a stabilizing force in my life as well as an inspiration. To Mom and Dad, your constant encouragement and sincere support throughout the years have given me the strength and courage to do things I would have never dreamed possible. I look forward to spending much more time with each of you in the near future. I'd like to also thank my future wife, Ayami Mizutani, who has put up with so much over the last 7 years. I cannot wait to start out a new life with you in the near future. I'd like to thank my parents for their continued support over the years, and for lending an ear when I needed to vent my frustrations and anxieties.

Toshiya Suzuki

January 2014

List of Papers

1. Original Papers

	Title	Journal	Authors
1	Field Emissions from Organic Nanorods Armored with Metal Nanoparticles	Japanese Journal of Applied Physics **52** 120203 (2013).	T. Suzuki, K. Ishikawa, H. Kondo, M. Sekine, M. Hori
2	Influence of Preceding Process on Temporal Changes of Atom Densities in H_2 and N_2 Mixture Gas Plasma	Japanese Journal of Applied Physics (Accepted)	T. Suzuki, K. Ishikawa, H. Kondo, M. Sekine, M. Hori

2. International Conferences

	Title	Conference	Author
1	Study for Damage in Porous SiOCH Film with Air Exposure After H_2 or N_2 Plasma Treatment	2nd International Symposium on Advance Plasma Science and its Application, PA026A, Meijo University, Nagoya Japan, Mar. 7-10, 2010	T. Suzuki, M. Sekine, H. Toyoda, K. Takeda M. Hori
2	Sub-nm scale control of etched – profile-fluctuations in organic Low-*k* film etch	3nd International Symposium on Advance Plasma Science and its Application, Nagoya Institute of technology, Nagoya Japan, Mar. 6-9, 2011	T. Suzuki, M. Sekine, H. Toyoda, K. Takeda, M. Hori
3	Subnanometer-scale control of feature size and shape in organic low-*k* film etch	The 4th International Conference on Plasma-Nanotechnology & Science, Takayama public cultural hall, Gifu Japan, Mar. 7-12, 2011	T. Suzuki, S. Mitsuguti, K.Ishikawa, M. Sekine, M. Hori And 2 more authors
4	Field Emission Properties of 10-nm Pillars of Organics Fabricated by Pt Particles and Plasma Etching	2011 International Conference on Solid State Devices and Materials, Takayama public cultural hall, Gifu Japan, Mar. 7-12, 2011	T. Suzuki, H. kondo, K.Ishikawa, M. Sekine, M. Hori And 2 more authors

	Titile	Conference	Author
5	Influence of Last Condition in Plasma Reactor on Gaseous Radical Density	The 11th Asia Pacific Conference on Plasma Science and Technology and and 25th Symposium on Plasma Science for Materials, No. 2-P26, Kyoto University ROHM Plasma, Kyoto Japan Oct. 2-5 (2012)	T. Suzuki, H. kondo, K.Ishikawa, M. Sekine, M. Hori And 4 more authors
6	Etched Profile Control in H_2/N_2 Plasma with Radical Density Control	Advanced Materialization Conference 2012 22nd Asian Session, No. P-9, Ichizyo Hall, Tokyo Japan, Oct. 22-25 (2012)	T. Suzuki, H. kondo, K.Ishikawa, M. Sekine, M. Hori And 1 more authors
7	Subsequent Temporal Change and Control of Gaussians H and N radical Density in Plasma after Different Process	AVS 59th International Symposium & Exhibition, No. PS1-TuM5, Tampa convention center, Florida, America, Oct. 22-25 (2012)	T. Suzuki, H. kondo, K.Ishikawa, M. Sekine, M. Hori And 2 more authors
8	Radical Density Control in H_2/N_2 Plasma Based on In-situ Monitoring with Vacuum Ultra Violet Absorption Spectroscopy	The 16th International Workshop on Advanced Plasma Processing and Diagnostics Okazaki Conference Center, Okazaki, Japan, Jan. 26 (2013)	T. Suzuki, H. kondo, K.Ishikawa, M. Sekine, M. Hori And 2 more authors
9	Subsequent Temporal Change of Gaseous Atom Density in H_2/N_2 Plasmas after Different Processes	The 5th International Conference on Plasma-Nanotechnology & Science, Inuyama public cultural hall, Gifu Japan, Mar. 9-10, 2012	T. Suzuki, H. kondo, K.Ishikawa, M. Sekine, M. Hori And 1 more authors

3. Research Project

・International Training Program (Program for incubating young researchers on plasma nanotechnology materials and device processing, conducted by Japan Society for the Promotion of Science) in Sungkyunkwan University, Korea, from December 2009 to January 2010

・International Training Program (Program for incubating young researchers on plasma nanotechnology materials and device processing, conducted by Japan Society for the Promotion of Science) in Texas University at Dallas, The United State, from January to March 2011

・International Training Program (Program for incubating young researchers on plasma nanotechnology materials and device processing, conducted by Japan Society for the Promotion of Science) in Sungkyunkwan University, Korea, from September to August 2012

4. Awards

・**Encouragement Reward**

32nd (2012 spring) Japan society and applied physics “lecture encouragement reward”, Ehime University, Ehime, Japan, September 14-17, 2012